

MAGNETOM Flash

Issue Number 78 · 1/2021
ISMRM Edition

siemens-healthineers.com/magnetom-world

Page 4

Editorial Comment

Raju Sharma, et al.

Page 15

Improved Patient Throughput

Val Runge, Johannes Heverhagen

Page 22

Initial Clinical Experience with Iterative Denoising

Johan Dehem, et al.

Page 29

Deep Resolve

Nicolas Behl

Page 46

Compressed Sensing TOF MR Angiography

Luigi Cirillo, et al.

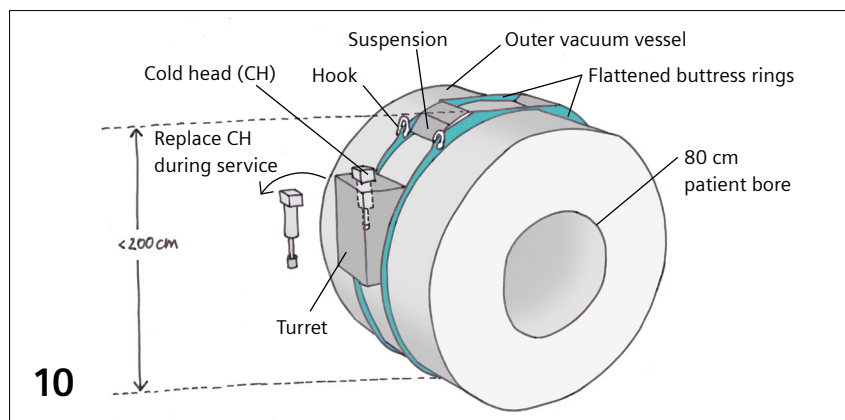
Page 67

Pushing the Limits of Accuracy in MRI

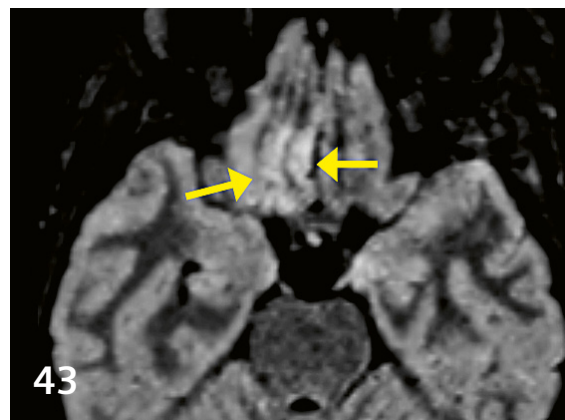
John E. Kirsch



Deep Resolve



MAGNETOM Free.Max – Big Inside and Small Outside



Cortical Involvement in COVID-19 Patients

Editorial Comment

4 Current Status of MRI in India

Raju Sharma, Devasenathipathy Kandasamy, Ankur Goyal
All India Institute of Medical Sciences, New Delhi, India

MAGNETOM Free.Max¹

6 Image Gallery 0.55T MAGNETOM Free.Max

10 MAGNETOM Free.Max: Access to MRI – How to Make it Big Inside and Small Outside

Stephan Biber
Siemens Healthineers, Erlangen, Germany



Cover image: Deep Resolve
MAGNETOM Vida
PD TSE, p3, TA 1:50 min
Matrix size: 717 x 896

Advances in Core Clinical MRI

15 Important Updates for Advanced Imaging Topics, with a Perspective on Improved Patient Throughput

Val Runge, Johannes Heverhagen
University Hospital of Bern, Switzerland

22 Initial Clinical Experience with an Iterative Denoising Algorithm Applied to Reduced-data 2D Turbo Spin Echo Acquisitions

Johan Dehem, et al.
Jan Yperman Ziekenhuis, Ieper, Belgium

29 Deep Resolve – Mobilizing the Power of Networks

Nicolas Behl
Siemens Healthineers, Erlangen, Germany

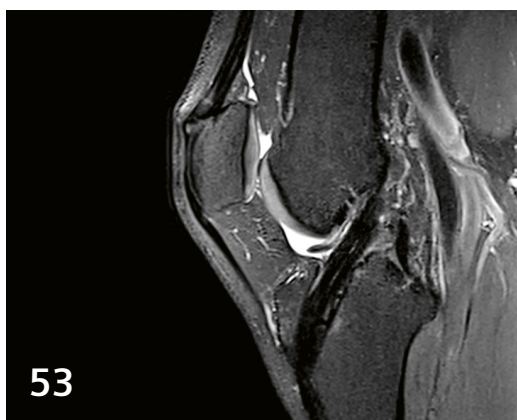
Pediatric Imaging²

36 4D Flow Characteristics After Aortic Valve Neocuspidization in Pediatric Patients: a Comparison with the Ross Procedure

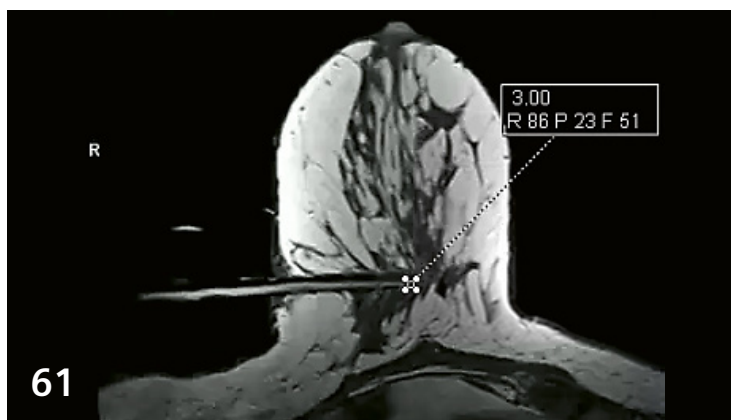
Aurelio Secinaro, et al.
Bambino Gesù Children's Hospital, IRCCS, Rome, Italy

¹ MAGNETOM Free.Max is pending 510(k) clearance, and is not yet commercially available in the U.S.

² MR scanning has not been established as safe for imaging fetuses and infants younger than two years of age. The responsible physician must evaluate the benefits of the MR examination compared to those of other imaging procedures.



Iterative Denoising Applied
to 3D SPACE CAIPIRINHA³



Breast Biopsy Workflow

Neurologic Imaging

- 43 MRI Depicts Olfactory Bulbs and Cortical Involvement in COVID-19 Patients with Anosmia**
Letterio S. Politi, et al.
IRCCS Humanitas Research Hospital, Rozzano, Milan, Italy

- 46 Case Series: Clinical Application of Compressed Sensing Time-of-Flight MR Angiography**
Luigi Cirillo, et al.
University of Bologna, Italy

Musculoskeletal Imaging

- 53 Iterative Denoising Applied to 3D SPACE CAIPIRINHA³: An Application to Musculoskeletal Imaging**
Chadi Hlailhel, et al.
Groupe Du Mail, Grenoble, France

Oncological Imaging

- 61 Breast Biopsy Workflow with syngo MR XA20 – How I Do It**
Sarah-Jane Lewis
Siemens Healthineers UK and Ireland

A History of Innovations

- 67 Pushing the Limits of Accuracy in MRI – A Perspective**
John E Kirsch
Athinoula A Martinos Center for Biomedical Imaging,
Massachusetts General Hospital, Charlestown, MA, USA

Remote Operations

- 74 Extending the Reach of MRI with Remote Operations**
Bac Nguyen, et al.
ARISTRA, Rasta, Norway
- 77 How Blended Learning can Provide Answers for Training in the COVID-19 Pandemic: Experience from France**
Magali Lopes, Maxime Roger
Saint-Denis, France

Meet Siemens Healthineers

- 81 Introducing Haitham Mohamed**
Business Development Manager,
Erlangen, Germany

³ Work in progress. The application is currently under development and is not for sale in the U.S. and in other countries. Its future availability cannot be ensured.



Dr. Ankur Goyal Dr. Devasenathipathy Kandasamy Dr. Raju Sharma

Raju Sharma, M.D., is a Professor of Radiology at the All India Institute of Medical Sciences (AIIMS) in New Delhi, the apex teaching institution of India. He trained at AIIMS and completed a fellowship at Massachusetts General Hospital in Boston, USA. His major area of interest is abdominal imaging and research focus is on diffusion-weighted imaging. He has done innovative work in the field of MR evaluation of bowel.

Devasenathipathy Kandasamy, M.D., trained at AIIMS in New Delhi and joined its faculty in 2012. His main areas of interest are pediatric radiology, MR physics, and artificial intelligence. He has done innovative work in the field of endocrine imaging, including 4D MRI of the parathyroid gland.

Ankur Goyal, M.D., also trained at AIIMS and joined its faculty in 2015. His main areas of interest are musculoskeletal and abdominal imaging. He has worked extensively on quantitative MR in renal masses and on MR characterization of soft-tissue tumors.

Current Status of MRI in India

Dear readers and friends,

We have been asked to introduce this edition of MAGNETOM Flash by talking about the status of magnetic resonance imaging in India. We are doing so at a very difficult time, as India is facing its worst-ever wave of the COVID-19 pandemic. Many other parts of the world are also fighting this pandemic. We convey our sincere wishes for the good health and safety of the international MR community and the world at large.

India is an emerging economy on the global horizon and is rich in human resources. Like elsewhere in the world, MRI indications are expanding in India – especially with the growing geriatric population, the burden of chronic non-communicable diseases, and the increased reliance on non-invasive diagnostic procedures. However, a major constraint in India is poverty and the very large population, which is spread unevenly across the country. A large part of the population still resides in rural areas. It is against this unique backdrop that we have to understand the status of MR in India.

The medical device industry in India is expected to grow to US\$50 billion by the year 2025. Currently, India is among the top 20 medical-device markets in the world and the fourth largest in Asia after Japan, China, and South Korea.

According to figures from 2019, there is an estimated annual market of approximately 270 to 280 MRI scanners shared by all the major vendors. The estimated number of MRI scanners installed across India is around 2,800 (including permanent magnet, 1.5T, and 3T scanners), of which the majority are 1.5T systems. 3T scanners are more common in metro and Tier-1 cities, and account for

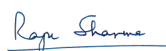
approximately 50–65% of the MRI market in those regions. Although 1.5T scanners still have the largest market share, the 3T systems are the ones contributing to the market growth. On an average, the annual market across government hospitals and medical colleges amounts to 40–60 MRI scanners and is cyclical. Private hospitals and diagnostic imaging centres account for about 220 new MRI scanners in a year. The volume of low-field-strength systems is stagnant at present.

The prohibitive cost of MR scanners limits their accessibility for the general population in our resource-poor environment. Most of the MR scanners are concentrated in the metro and Tier-1 cities. Penetration in rural areas is negligible. Also, the stringent requirements regarding power supply, a trained workforce, service, and maintenance are difficult to address at the peripheral level. On the positive side, in the last decade there have been many government initiatives to equip teaching hospitals across India with high-end MR scanners. Also, many new tertiary-care teaching hospitals are being set up across the length and breadth of the country, and are being equipped with state-of-the-art imaging equipment. The corporate sector has also set up hospitals in Tier-2 and Tier-3 cities, which will help to improve accessibility for the rural population. In the year lost to the COVID-19 pandemic, there has been a slump in the addition of new MRI scanners, although government-aided hospitals have perhaps been ahead of the private sector in the acquisition of new scanners. The government has also been promoting a Make in India campaign to bring down costs, adapt MRI to local requirements, and boost the domestic economy. As a result, a number of promising lightweight MRI scanners are in an advanced stage of development here.

Major limiting factors in MRI are the prohibitive cost, the need for trained personnel, and the complex infrastructure requirement for MR scanners. A cheaper lower-field-strength scanner that requires simpler infrastructure and can leverage recent advances – such as automated study planning, compressed sensing, innovative k-space filling strategies, remote support for troubleshooting, and deep-learning-aided image generation – would go a long way to making MR available to the Indian population. It would reduce both the capital and operational expenditure required for things such as helium top-ups, and could be used in areas where trained personnel is scarce. By utilizing the currently available technologies, it is possible to achieve good-quality diagnostic images with lower-field-strength scanners without a significant time penalty. There is a distinct need for low-cost MR scanners which can use optimum technology and provide good-quality images. In countries like India where trained personnel may not be available in small cities, it would further help if such scanners allowed the remote execution of MR protocols. This would be a major step toward making MR imaging more accessible in resource-poor regions of the world.

As far as the usage pattern is concerned, the bulk of the work at most sites is craniospinal imaging, followed by musculoskeletal imaging. Use of MR imaging for the evaluation of abdominal and chest diseases is generally confined to large tertiary-care and academic centres. In metro cities, there are many centres of excellence engaged in high-end research, including advanced applications like whole-body imaging, MR elastography, diffusion-weighted imaging (including intravoxel incoherent motion and diffusion kurtosis imaging), perfusion imaging, and texture analysis. These techniques have been used in India not only for the traditional oncology applications but also for diseases endemic in India, such as tuberculosis. Many groups in India, including ours, have published extensively on advanced MR applications.

This issue of MAGNETOM Flash contains some very interesting articles on the use of techniques for improving throughput, on the application of deep learning and AI to the field of MRI, and on iterative denoising. There is also an impressive gallery of images that were generated on the upcoming 0.55T system¹ using advanced technology. Happy reading!



Dr. Raju Sharma


Dr. Devasenathipathy
Kandasamy


Dr. Ankur Goyal

¹MAGNETOM Free.Max is pending 510(k) clearance, and is not yet commercially available in the U.S.

We appreciate your comments.

Please contact us at magnetomworld.team@siemens-healthineers.com

Editorial Board

Antje Hellwich
Editor-in-chiefRebecca Ramb, Ph.D.
Vice President of MR
Research & Clinical TranslationNadine Leclair, M.D.
MR Medical OfficerWellesley Were
MR Business Development
Manager Australia and
New ZealandJane Kilkenny
Vice President of MR
Malvern, PA, USASunil Kumar Suguru Laxman, M.D.
Clinical & Product Specialist MRI
Dubai, United Arab Emirates

Review Board

André Fischer, Ph.D.
Global Segment Manager
Neurology

Daniel Fischer
Head of Clinical and
Scientific Marketing

Christian Geppert, Ph.D.
Head of Cardiovascular Applications

Heiko Meyer, Ph.D.
Head of Neuro Applications

Gregor Thörmer, Ph.D.
Head of Oncological Applications

0.55T MAGNETOM Free.Max – Breaking Barriers

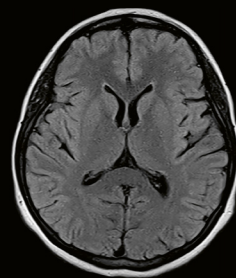
High-V MRI

Digitalization is rapidly transforming MR imaging by applying highly efficient acquisition techniques and Deep Learning-based reconstruction. High-V MRI takes the power of digitalization and deliberately applies it to a new field strength of 0.55T with inherent clinical benefits.

MAGNETOM Free.Max¹ breaks barriers to expand the reach of MRI

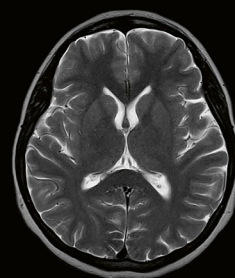
Where patients have felt discomfort, the world's first 80 cm bore sets a new paradigm in patient comfort.

Where infrastructure was an obstacle to MRI, MAGNETOM Free.Max slots into an existing helium-free infrastructure. Where access to MRI was not viable, MAGNETOM Free.Max makes access affordable. And where conventions have limited our thinking, MAGNETOM Free.Max breaks out of conventions to explore new clinical opportunities in MRI.



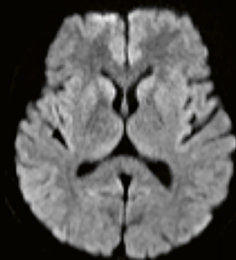
4aaaa0448

T2 FLAIR, Deep Resolve
Gain & Sharp,
ST 5 mm, TA 04:15 min



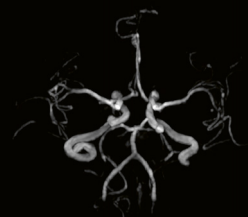
4aaaa0448

T2 TSE, Deep Resolve
Gain & Sharp,
ST 5 mm, TA 02:52 min



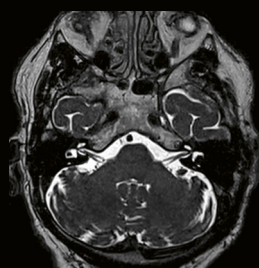
4aaaa0448

DWI b-value 1000 s/mm², PAT 2,
ST 5 mm, TA 01:49 min



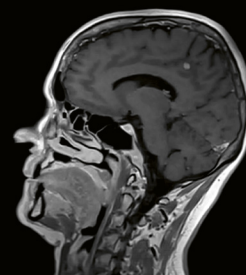
4aaaa0398

TOF, PAT 2,
ST 0.5 mm, TA 05:56 min



4aaaa0513

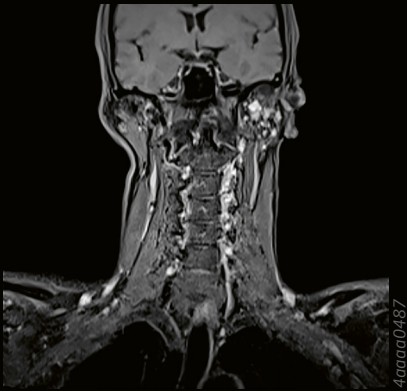
T2 CS SPACE Inner Auditory
Canal, CS 2,
ST 0.7 mm, TA 05:11 min



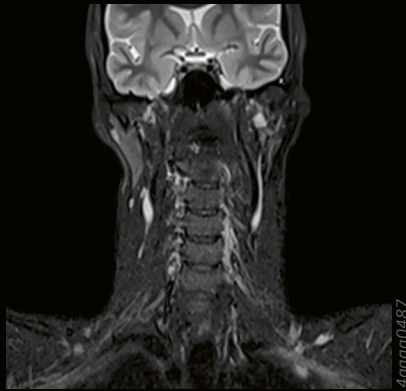
7aaaa0084

T1 CS SPACE CE sag, CS 2.5,
ST 1 mm, TA 04:50 min.
Courtesy of University Hospital
Erlangen, Germany

¹MAGNETOM Free.Max is pending 510(k) clearance, and is not yet commercially available in the U.S.



T1 TSE Dixon cor, SMS 2,
ST 4 mm, TA 04:36 min. *Courtesy of
University Hospital Erlangen, Germany*



T2 TIRM cor, ST 4 mm, TA 05:00 min.
*Courtesy of University Hospital
Erlangen, Germany*



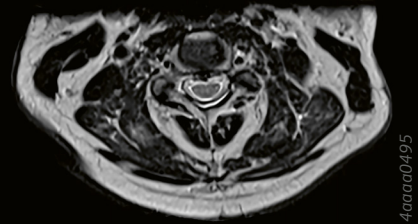
3D FLASH CE-MRA MIP, PAT 2, ST 1.2 mm,
TA 00:17 min. *Courtesy of University Hospital
Erlangen, Germany*



T1 TSE sag, PAT 2, ST 3 mm, TA 04:02 min.
*Courtesy of University Hospital Erlangen,
Germany*



T2 TSE sag, PAT 2, ST 3 mm, TA 04:40 min.
*Courtesy of University Hospital Erlangen,
Germany*



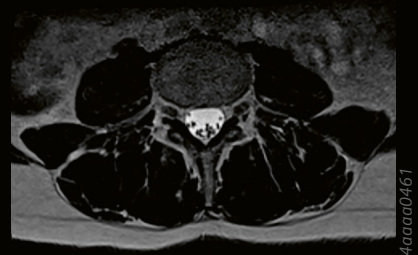
T2 TSE tra, Deep Resolve Gain & Sharp,
ST 3 mm, TA 03:42 min. *Courtesy of
University Hospital Erlangen, Germany*



T1 TSE sag, Deep Resolve Gain & Sharp,
ST 4 mm, TA 03:40 min. *Courtesy of
University Hospital Erlangen, Germany*



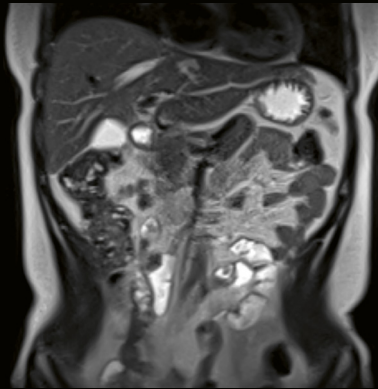
T2 TIRM sag, Deep Resolve Gain & Sharp,
ST 4 mm, TA 04:24 min. *Courtesy of
University Hospital Erlangen, Germany*



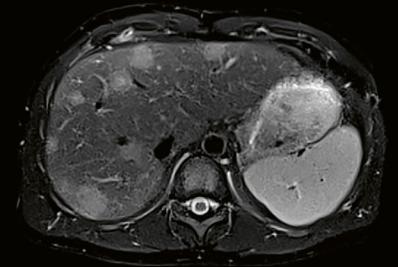
T2 CS SPACE tra, CS 3, ST 2.5 mm,
TA 04:32 min. *Courtesy of University Hospital
Erlangen, Germany*



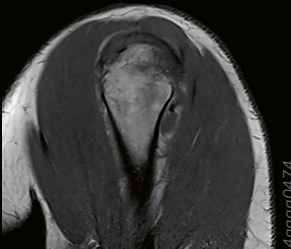
T2 fatsat cor, ST 3 mm,
TA 05:07 min.
Courtesy of University Hospital
Erlangen, Germany



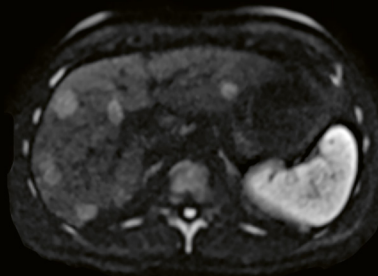
T2 HASTE cor, PAT 3,
ST 6 mm, TA 02:03 min



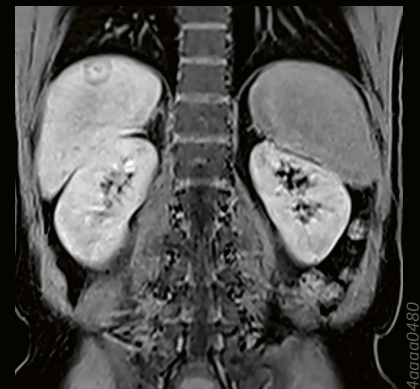
T2 fast-BLADE fatsat trig, PAT 2, ST 6 mm,
TA 05:28 min. Courtesy of University Hospital
Erlangen, Germany



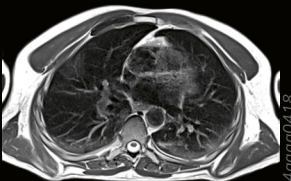
T1 TSE sag, ST 3 mm,
TA 05:33 min.
Courtesy of University Hospital
Erlangen, Germany



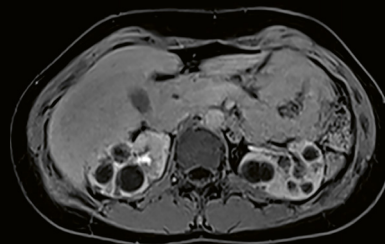
DWI b-value 800 s/mm², Deep Resolve Gain,
PAT2, ST 6 mm, TA 04:11 min. Courtesy of
University Hospital Erlangen, Germany



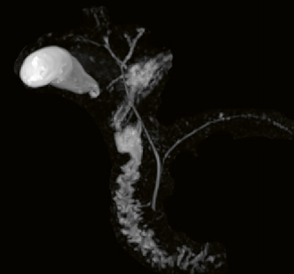
T1 VIBE Dixon water cor,
Deep Resolve Gain, CAIPIRINHA 4, ST 3 mm,
TA 00:16 min. Courtesy of University Hospital
Erlangen, Germany



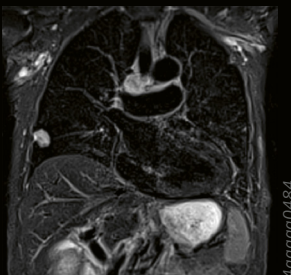
PD TSE fast-BLADE trig, PAT 2,
ST 6 mm, TA 04:26 min.
Courtesy of University Hospital
Erlangen, Germany



T1 VIBE Dixon water tra,
Deep Resolve Gain, CAIPIRINHA 3, ST 3 mm,
TA 00:18 min. Courtesy of University Hospital
Erlangen, Germany



MRCP T2 CS SPACE MIP, CS 6.5,
ST 1 mm, TA 04:21 min

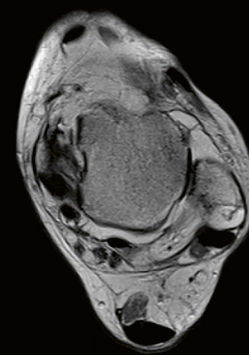


PD TIRM fast-BLADE trig, PAT 2,
ST 6 mm, TA 06:44 min.
Courtesy of University Hospital
Erlangen, Germany



PD TSE SEMAC², PAT 3, ST 4 mm, TA 07:24 min

4aaaa0508



4aaaa0496

PD TSE tra, ST 3 mm, TA 04:56 min. Courtesy of University Hospital Erlangen, Germany



4aaaa0522

PD TSE fatsat cor,
Deep Resolve Gain & Sharp,
ST 3 mm, TA 04:50 min



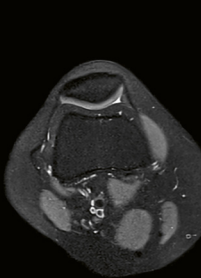
4aaaa0522

PD TSE sag,
Deep Resolve Gain & Sharp,
SMS 2, ST 3 mm, TA 02:40 min



4aaaa0522

PD TSE fatsat sag,
Deep Resolve Gain & Sharp,
ST 3 mm, TA 05:20 min



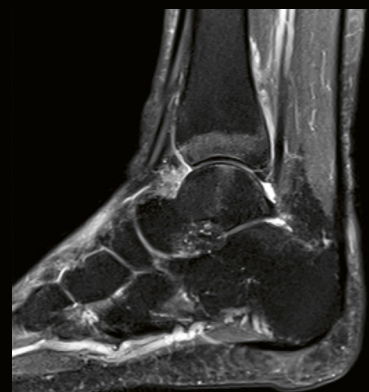
4aaaa0522

PD TSE fatsat tra,
Deep Resolve Gain & Sharp,
ST 3 mm, TA 04:48 min



4aaaa0496

T1 TSE cor, ST 3 mm, TA 05:18 min. Courtesy of University Hospital Erlangen, Germany



4aaaa0496

PD TSE fatsat sag, ST 3 mm,
TA 04:21 min. Courtesy of University Hospital Erlangen, Germany

²The MRI restrictions (if any) of the metal implant must be considered prior to patient undergoing MRI exam. MR imaging of patients with metallic implants brings specific risks. However, certain implants are approved by the governing regulatory bodies to be MR conditionally safe. For such implants, the previously mentioned warning may not be applicable. Please contact the implant manufacturer for the specific conditional information. The conditions for MR safety are the responsibility of the implant manufacturer, not of Siemens Healthineers.

MAGNETOM Free.Max: Access to MRI – How to Make it Big Inside and Small Outside

Stephan Biber, Ph.D.

Senior System Architect & Principal Key Expert at Siemens Healthineers, R&D AEP, Erlangen, Germany

MR systems have always been known to be large, heavy machines that require a complex infrastructure such as the supply of liquid helium and a highly reliable supply of electricity and cooling. While the new DryCool magnet technology has been presented in detail by Simon Calvert [1], this article will focus on how the MAGNETOM Free.Max¹ system is able to be big on the inside with the first-ever 80 cm patient bore on the market, making it at the same time one of the smallest whole-body MRI systems on the market. With a footprint of just 24 m², a transportation height of less than 2 meters, and a weight of only 3.2 tonnes we believe the system defines a new class of MRI systems. This paper will present a number of technical innovations, which in isolation could be seen as simple engineering tasks, but together they help to overcome long-established issues with the installation process and therefore can realize unmet customer needs. Furthermore, we would like to demonstrate how only a holistic system-perspective, which aligns all the engineering disciplines behind a common goal, is able to accomplish this.

How to make it big: Combining field strength and gradient power with new imaging techniques

MR systems with solenoid magnets have been available with 60 cm patient bores since the early 1990s. In 2004, Siemens Healthineers introduced MAGNETOM Espree, the first 1.5T system with a 70 cm bore and MAGNETOM Verio in 2007, the first 3T system with a 70 cm bore. This broadened access to MRI for growing patient groups by improving comfort, counteracting claustrophobia, and accommodating obese patients in the bore. Despite the larger bore on the 70 cm systems, the need remained for even more space in the bore for the same reasons that first triggered the development of 70 cm systems. But whereas 20 years ago, the market was able to deal with

the associated increased costs of 70 cm systems versus 60 cm systems, the situation is different today. Radiology is under severe cost pressure, which calls for new ways of providing high-value imaging with improved patient access at an affordable cost.

The belief in MRI has long been that higher field strengths and gradient powers together with a high receive system channel count delivers better image quality and higher speeds. This belief still holds true but there are other ways to serve markets that require the diagnostic quality of a 1.5T system but not necessarily at exactly the same speed and contrast. A larger bore diameter is essentially what drives up the costs of MRI systems. This, in turn, reduces the accessibility of MRI to a large part of the worldwide population. The costs of the magnet (mainly the superconductive wire) increase rapidly as the size rises. Gradient coil power increases with $\sim R^5$, which would quadruple the power needed when going from a 60 to 80 cm patient bore. The only way out is to go against the grain and question existing assumptions on field strength and gradient power.

During an early prototyping phase back in 2016, a 1.5T MAGNETOM Aera system was ramped down to 0.55T and equipped with modified RF-electronics. With *in vivo* imaging, it was then possible to assess image quality and analyze the impact of different types of gradient engines.

Designed as our most compact whole-body MRI MAGNETOM Free.Max



Open
80 cm



Small
24 m²



Light
< 3.2 t



Low
< 2 m

¹MAGNETOM Free.Max is pending 510(k) clearance, and is not yet commercially available in the United States.

The in-house prototype and a replica of this system installed at the National Institutes of Health (NIH) helped to demonstrate that routine clinical questions in general radiology can be answered at a field strength of 0.55T [2]. Our internal analysis indicated that acceptable image quality and measurement times could be achieved with a gradient engine of 45 T/m/s and a gradient field of approximately 26 mT/m for this application field. In contrast to the 1990s, we were able to combine this MRI system with new imaging techniques that help overcome some of the drawbacks of mid-field imaging. These negative aspects had originally stimulated the design of 1.5T scanners, e.g., DeepResolve Gain and Sharp are image reconstruction methods enabling intelligent, iterative denoising using individual noise maps and an increase in image resolution using a deep neural network. These technologies can be used to reduce acquisition times and improve image quality simultaneously. At the same time, Deep Resolve can be combined with image acceleration techniques such as parallel imaging – which was not available in the 90s – and Simultaneous Multi-slice (SMS) on MAGNETOM Free.Max. In addition, Compressed Sensing has also proven to be a valuable tool for acquisition acceleration. For clinical examples, please refer to the Image Gallery [3].

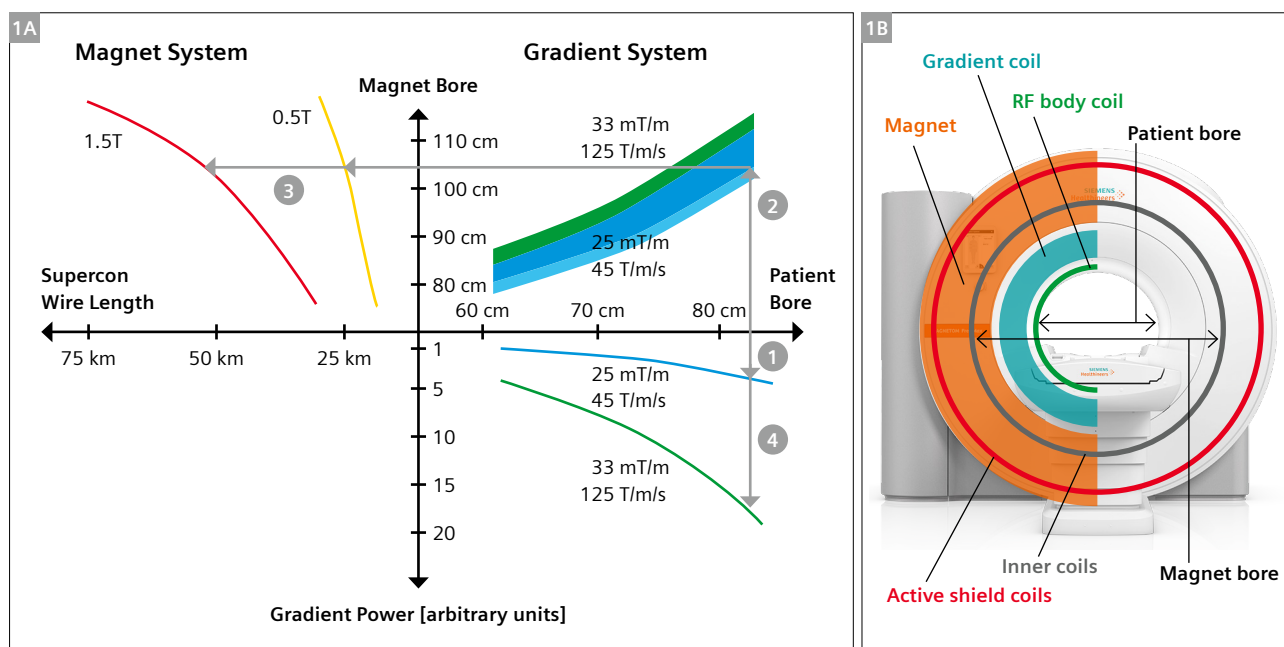
The unique combination of a 0.5T scanner with various powerful new acquisition and reconstruction techniques laid the foundation for the innovation, MAGNETOM Free.Max. The reduced field strength on both the magnet and the gradient engine allowed the bore diameter to be

scaled up from 60 to 80 cm, while still keeping the superconductive wire length and gradient power within a range that would make the system more affordable.

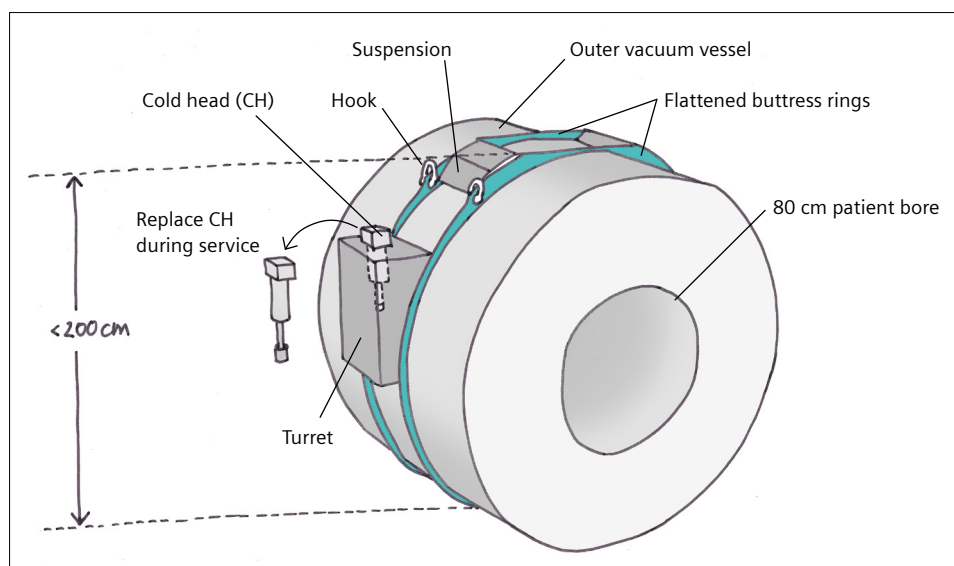
Figure 1A shows the optimization in the multiparameter space: superconductive wire length and costs increase with field strength and magnet bore diameter. When starting with an 80 cm patient bore (1), the thickness needed for the gradient coil and the body coil dictate the magnet bore diameter. For the sake of simplicity here, we assume a range of different thicknesses shown by the blue and green areas, with a slight tendency of gradient coils with higher G_{\max} and SR to also require more radial space (2). With the magnet bore diameter derived from the outer diameter of the gradient coil, the impact on wire length for 0.5T and 1.5T are shown by the yellow and red curves (3), assuming similar boundary conditions on the stray field. These two curves show the huge scale of the nonlinear increase in the superconductive wire for the magnet when field strength and bore diameter are increased.

Starting from the 80 cm bore diameter, looking into the lower right quadrant (4), it becomes evident that the gradient power not only increases with higher SR and G_{\max} , but it increases disproportionately with patient bore diameter.

Increased gradient power usually goes hand in hand with the additional power needed for the cooling system, which has to extract the heat from the gradient coil and the gradient power amplifier (GPA) and dissipate it in the



1 (1A) Scaling of superconductive wire length and gradient power with patient bore and field strength. Figures are merely illustrative to show the main correlations. Please note that the numbers in this article are also indicative to explain the physics and not related to a special design. (1B) When starting with an 80 cm patient bore, the thickness needed for the gradient coil and the body coil dictate the magnet bore diameter.



2 Figure 2 shows the flattened buttress rings, the outer vacuum vessel (OVC) with the shield coils, and the turret with the cold head that is moved further down on the side of the system.

air. Therefore, stronger gradients have a quadruple effect on the system design: They require more power to generate the fields, they require more cooling to extract the resulting heat and together this drives needs on local infrastructure up (connection power, space for chiller, etc.). They tend to also drive the gradient coil thickness and therefore the inner diameter (4) of magnet.

Scaling the Tx subsystem to provide sufficient B_1 amplitude on a 23 MHz system with an 80 cm patient bore is – compared with the magnet and gradient design – the easiest piece in this puzzle. Luckily, a lower Larmor frequency also requires less power to achieve the same B_1 field. Therefore, an existing 63 MHz amplifier can be tuned to 23 MHz and the additional power can be invested in overcoming the lower efficiency $\eta = B_1/P_{BC}$ of a body coil with a larger diameter. The lower conductivity of tissue at a lower frequency also makes SAR an almost negligible issue.

How to keep it small

While the inside of an MRI system should be as large as possible to provide space for the patient, it is more difficult to identify what the system should look like from the outside. When observing an installation process, it immediately becomes clear that the height of the system is a critical parameter: The system should be easily movable through doors. In the past, even removing doors often did not help and MRI installations frequently meant breaking up concrete structures, affecting the structural integrity of the building. Naturally, this was often associated with high costs and organizational efforts as well as other unwanted consequences. In many countries, two-meter high door openings are standard. Here is the simple but effective recipe with five major ingredients how to make sure the MRI system stays below 2 m height:

1. Outer vacuum vessel: Limit shield coil diameter

Underneath the plastic cover of an MRI system is the outer vacuum chamber (OVC), which contains the cryoshield and the superconductive magnet coils (dry magnets do not need a helium vessel). When the inner coils of the magnet are moved outward to accommodate the large patient bore, the shield coils also tend to move further out. Setting a boundary of ~1.95 m for the diameter of the OVC sets a clear design goal for the position of the shield coils. If the OVC is to be within the two-meter limit, it is essential that no other parts of the system design exceed this limit.

2. Buttress rings and magnet suspension

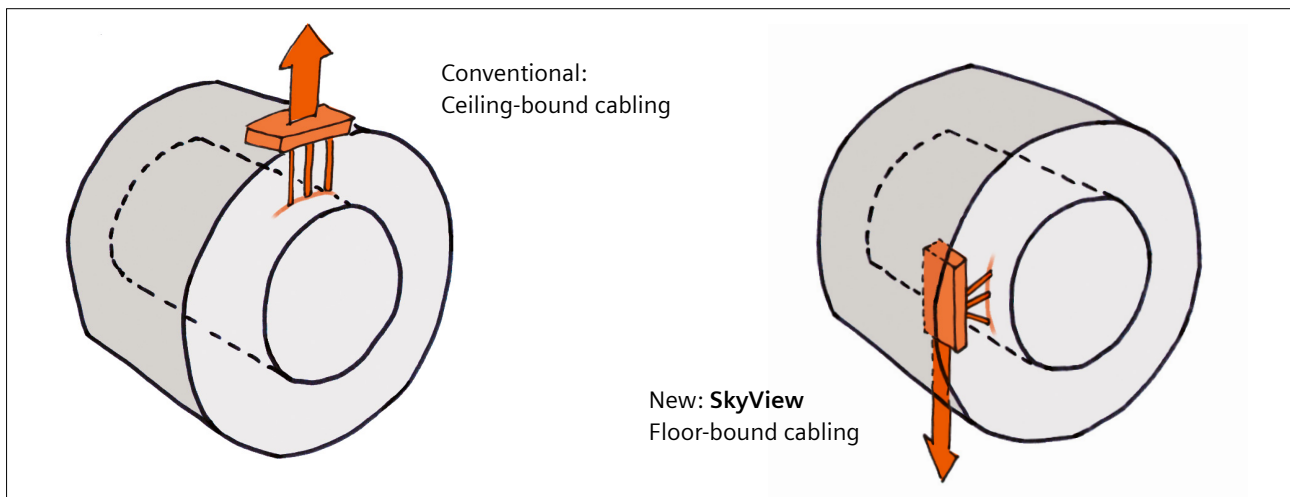
For the OVC to withstand the 1 bar atmospheric pressure from the outside, it is reinforced using circumferential buttress rings. These rings are flattened at the top of the magnet without any negative impact on their structural stiffness, which in turn allows the shield coils to be moved out as far as possible inside the OVC. Another structure that potentially affects the overall height of the system are the suspensions that hold the magnet coils in place. A tensile suspension connects the 4 K cold inside of the magnet with the warm outer vacuum chamber (OVC). The mechanical structure required to mount the tensile suspension to the outside of the OVC needs to be very slim so that this is not the highest point.

3. Quench pipe

The dry magnet does not need a quench pipe. It follows that there is no pipework on top of the magnet that could require extra height on top of the OVC and would require the connection of the magnet to the ceiling. This makes the new SkyView option possible (Fig. 3), which gives the system a unique visual impression by removing any connection between the MR scanner and the ceiling.



3 (3A) Conventional system with quench pipe. (3B) MAGNETOM Free.Max with DryCool magnet technology and easy siting.



4 Gradient connection and SkyView

4. Gradient connections

The gradient coil needs to be connected to the gradient cables that deliver the current from the gradient power amplifier (GPA). As in every electrical connection, the point where two cables are joined together is critical to maintaining good electrical contact. The gradient cables carry currents over 300 A and voltage up to 1200 V, so any loose connections could generate sparks that must be avoided. The connection of gradient cables is particularly critical due to the high Lorentz forces:

$$|\vec{F}_L| = |I| |\vec{\ell}| |\vec{B}| \sin \alpha$$

Locally, the actual field at the end of the magnet can be higher by up to a factor of 2–3 than the nominal field at the isocenter. For a 1.5T system with a strong gradient engine ($I = 900$ A), a 40 cm long gradient cable at the end of the magnet will experience a force of approx. 500–1500 N (equaling 50–150 kg) oscillating with the gradient pulses. This is why, historically, the connection of the gradient cables from the GC to the cables from the GPA on scanners from Siemens Healthineers was on top of the magnet. Here, the fields perpendicular to the wires and the resulting Lorentz forces are lower. This location for the gradient connection was never an issue on wet MRI magnets, because other parts (e.g., the cold head or pipework for the quench line) were located even higher.

I = current, ℓ = length of wire/cable, B = magnetic flux density aka magnetic field, α = angle between wire/cable and B



5 MAGNETOM Free.Max installation at University Hospital Basel in Switzerland. Even during one of the very first installations, the small size of the system and the eliminated quench pipe paid off to make the installation process much easier.

With the lower field strength and the lower gradient current, it was possible to reduce the forces by almost one order of magnitude. This facilitates a gradient connection on the rear side of the magnet rather than on the top. This is also required for the SkyView siting option. Here, gradient cables are routed together with all other cables through the floor rather than the ceiling (Fig. 3B).

5. Cold head

The cold head in conventional MRI magnets, where the superconductive coils are submerged in a liquid helium bath, needs to be located above the liquid helium level to allow recondensation of the gaseous helium. In dry magnets that have just a small helium reservoir as a liquid heat buffer rather than a large helium vessel, the cold head can sit in any vertical position. On MAGNETOM Free.Max, the cold head is located inside a turret, mounted on the side ~30 cm below the upper boundary of the OVC. This not only allows unhindered transportation through 2 m high doors, but also means that all later service activities (e.g., cold head replacement) can be performed within a ceiling height of just 2.2 m – even after the system has been installed in its final location. Since MAGNETOM Free.Max can be both installed and serviced in low-height

premises, MR diagnostics can now be brought to new places such as small imaging centers. These are often located in residential buildings with limited available space.

This overview shows how a complete design overhaul of the magnet and gradient system together with the use of new imaging and reconstruction techniques results in an MRI system that achieves somewhat contradictory goals: A large 80 cm bore for the patient with a scanner that delivers diagnostic image quality AND easy installation with a small physical footprint and low connection power.

More background information on MAGNETOM Free.Max and DryCool magnet technology will be available soon on: www.siemens-healthineers.com/magnetom-world.

References

- 1 Calvert S. A Brief History of the DryCool Magnet Development. MAGNETOM Flash. 2020; MAGNETOM Free.Max special issue. Available at <https://www.magnetomworld.siemens-healthineers.com/hot-topics/lower-field-mri>
- 2 Campbell-Washburn AE, Ramasawmy R, Restivo MC, et al. Opportunities in Interventional and Diagnostic Imaging by Using High-Performance Low-Field-Strength MRI. Radiology. 2019;293(2):384-393.
- 3 MAGNETOM Free.Max Image Gallery. MAGNETOM Flash (78) 1/2021. Available at <https://www.magnetomworld.siemens-healthineers.com/publications/magnetom-flash>

Contact

Stephan Biber, Ph.D.
Siemens Healthineers
SHS DI MR R&D AEP
Postbox 32 60
91050 Erlangen
Germany
stephan.biber@siemens-healthineers.com



Important Updates for Advanced Imaging Topics, with a Perspective on Improved Patient Throughput

Val M. Runge, M.D.; Johannes T. Heverhagen, M.D., Ph.D.

Department of Diagnostic, Interventional and Pediatric Radiology, University Hospital of Bern, Inselspital, University of Bern, Bern, Switzerland

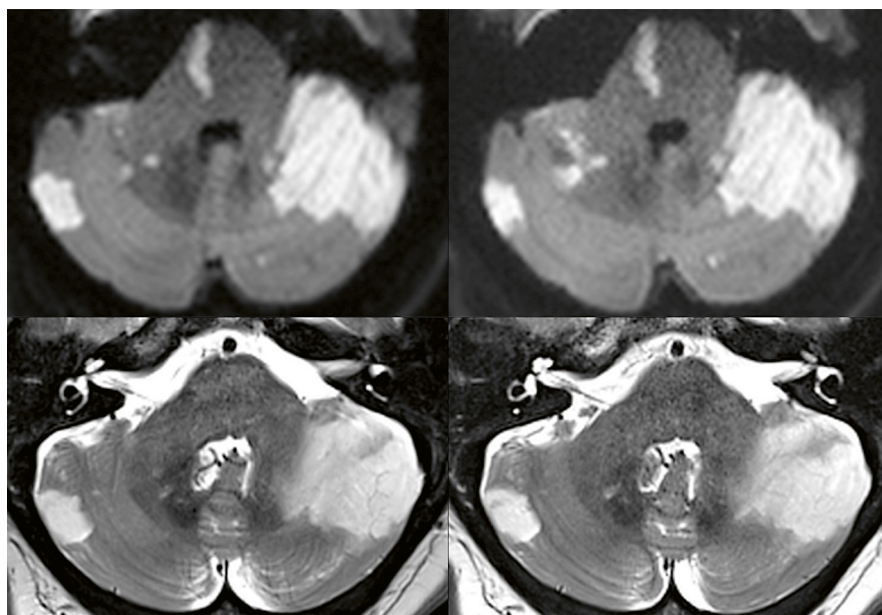
Introduction

Five important relatively recent innovations involving MR scan techniques and the approach to the patient are described. These include specifically simultaneous multi-slice (SMS), compressed sensing, GRASP (and its variants), respiratory sensing (using a sensor embedded into the patient table), and monitoring cardiac contraction employing a Pilot Tone¹ (as opposed to the ECG). Each offers potentially major time savings relative to any patient's exam time, impacting in a positive way patient throughput.

¹ Work in progress: the application is currently under development and is not for sale in the U.S. and in other countries. Its future availability cannot be ensured.

Simultaneous Multi-slice (SMS)

In simultaneous multi-slice (SMS) technique, multiple slices are excited at the same time, with each slice subsequently individually reconstructed. This is a major innovation in scan acquisition that occurred in the past decade. By use simply of an acceleration factor of two – the most common implementation clinically, scan times for applicable sequences can be reduced nearly in half. The physics involved is somewhat complex, with the details not important for clinical application. To give a brief summary of how such scans can be acquired, blipped CAIPIRINHA is applied during the echo train (minimizing *g*-factor-related SNR loss) – with for example two non-adjacent slices excited.



1 Multiple early subacute cerebellar infarcts with high signal intensity on both DWI and T2-weighted scans. The conventionally acquired scans are on the left, the SMS scans on the right. The scans were acquired at 3T, with 2x (for DWI) and 3x (for T2) acceleration factors employed using SMS. Adapted with permission from *Invest Radiol* 2019;54:383-95.

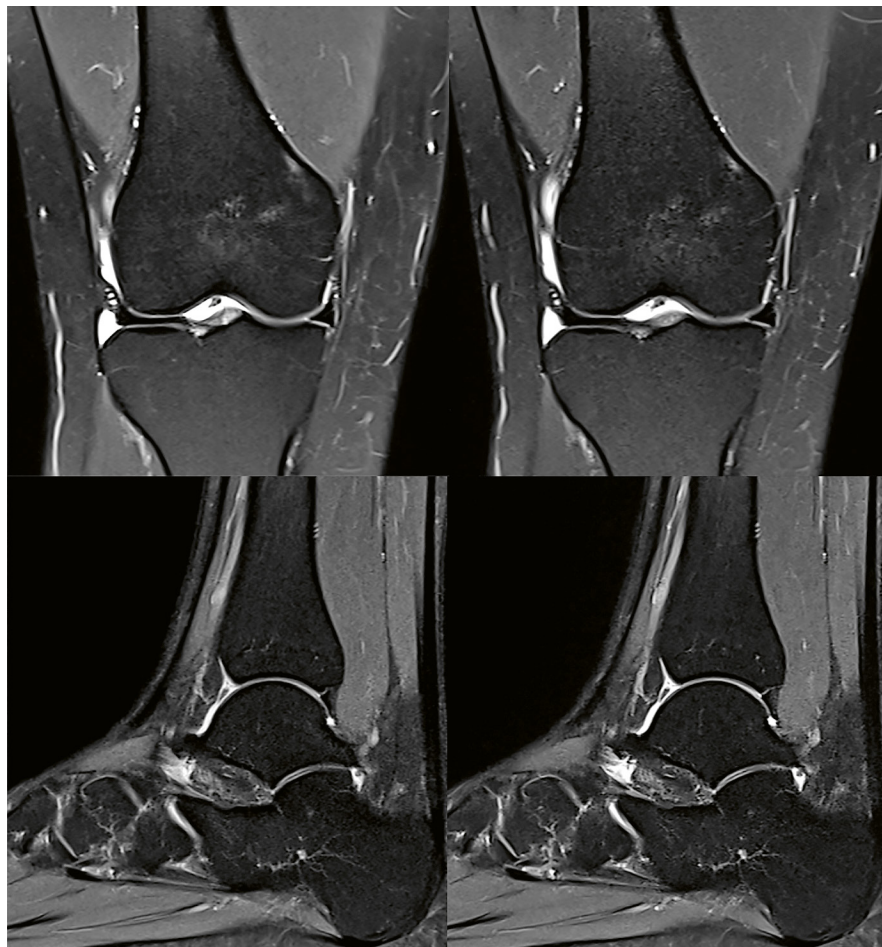
Reconstruction of the images is then accomplished by first applying slice GRAPPA-based unaliasing, and subsequently in-plane GRAPPA-based unaliasing. Otherwise the single reconstructed image would represent the sum of the two slices [1].

There is an important difference between parallel imaging and SMS. Both are commonly used to reduce scan time, however with parallel imaging SNR is markedly decreased (but not with SMS). In parallel imaging, fewer k -space lines are acquired, the cause of the reduction in SNR. The fundamental basis of parallel imaging is the use of coil sensitivity information (from a multichannel coil) to reconstruct missing k -space lines. The loss in SNR with parallel imaging is proportional to both the coil specific geometry (g) factor and the square root of the acceleration factor. The g -factor is a noise amplification factor that varies across the image volume, a result of the estimation process of the unwrapping algorithm. Because blipped CAIPIRINHA is employed in SMS, the g -factor loss is minimized. And, since there is no reduction of acquired k -space lines, there is no related SNR penalty.

An important clinical tip when employing SMS is to use the receiver coil with the highest coil density available.

For example, given the choice between a 20-channel and a 64-channel head coil, the latter should be chosen. Higher coil density specifically when using SMS generally provides a higher signal-to-noise ratio.

SMS can be utilized with both echoplanar and turbo spin echo (TSE) scan sequences (Fig. 1) [2]. The technique was first introduced for diffusion-weighted imaging, and then subsequently for TSE. Important applications of SMS single-shot (ss) EPI DWI include scan time reduction for liver imaging, due to the number of slices needed, and, although it might not be immediately evident, in a similar fashion for scan time reduction in imaging of the prostate – due to the thin sections required. In another DWI application, SMS is commonly employed at 3T with readout-segmented EPI scans (rs-EPI, RESOLVE). RESOLVE offers reduced geometric distortion and blurring at 3T, which leads to poor image quality when using single shot EPI. Susceptibility artifacts, such as those caused by the air filled sinuses, are also decreased substantially by the use of RESOLVE. However, an important limitation of RESOLVE is the longer scan time when compared with ss-EPI. Thus, SMS is used routinely today for scan time reduction with RESOLVE. This is achieved by reducing the



2 Proton density-weighted, fat suppressed, TSE scans at 1.5T of the knee (upper row) and ankle (lower row). The conventional acquisitions are displayed on the left, the SMS acquisitions on the right. In both instances 2x acceleration was employed, resulting in scan time reductions respectively of 45% and 32%. In clinical practice SMS scans are often preset with minor variations in other parameters, to achieve the best combined image quality and slice coverage, thus leading to less reduction in scan time than a factor of 2 (a 50% reduction) – for instance with the ankle scan presented. Adapted with permission from *Invest Radiol* 2019;54:383-95.

TR in combination with the application of SMS. Another application of rs-EPI is acoustic noise-optimized DWI (reducing the noise of the scan for increased patient acceptance). In this application, echo spacing is increased and thus the noise due to the reduced gradients. On the negative side, image distortion and bulk susceptibility artifacts are increased – which can be countered by the use of readout-segmented EPI.

Following the successful implementation of SMS for DWI, this innovation was extended to TSE technique. SMS TSE is not restricted to any one tissue contrast, but can be used with proton density-, T1-, and T2-weighted imaging. SMS TSE is implemented for scans that would otherwise need multiple concatenations to acquire the required number of slices. SMS with a factor of 2 allows in essence twice the number of slices to be sampled within the same TR, thus making possible the number of concatenations to be halved and thus also scan time. It is used in certain instances for brain and soft tissue neck imaging, and in particular for musculoskeletal imaging.

SMS was first introduced at 3T, and subsequently extended to 1.5T systems (Fig. 2). It has excellent applicability at both fields, with little difference in terms of efficacy – specifically in terms of reducing scan time. In regard to next generation low-field (0.55T) MR units, SMS will also likely play an important role [3]. However, this will be different than what it is applied for at 1.5 and 3T, which is mainly to decrease scan time. At 0.55T SMS is likely to be implemented to increase SNR while maintaining scan time, due to the lower intrinsic SNR at 0.55T.

Compressed Sensing (CS)

Compressed sensing has been available clinically now for several years for specific applications, leading to a substantial reduction in scan time. The time required for image reconstruction was originally quite long with this technique. However, this process has been streamlined,

and new hardware introduced, making reconstruction times suitable for routine clinical use of CS scan sequences.

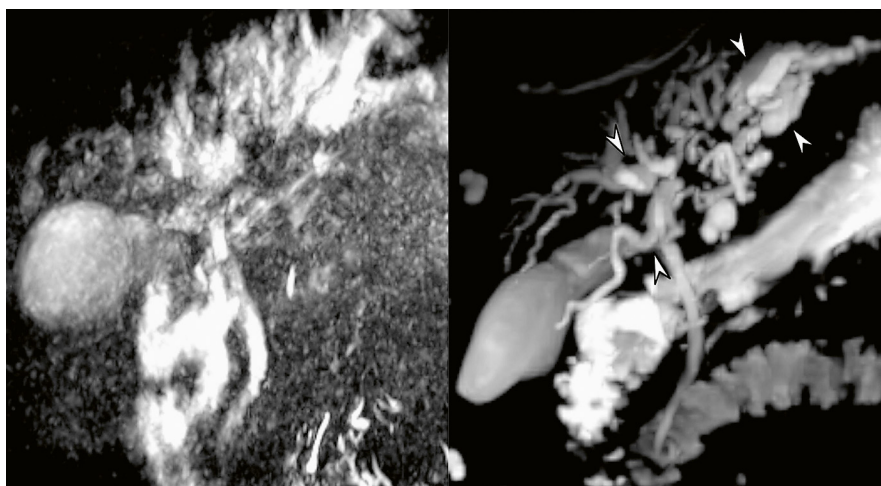
The compressed sensing variants of VIBE, including GRASP-VIBE, XD-GRASP¹, CS-VIBE and XD-VIBE¹, will be discussed in the next section. These scans have specific applicability for liver imaging. These also allow liver perfusion calculations to be made from a free-breathing dynamic post-contrast scan, thus eliminating an additional contrast injection and not further prolonging exam time. XD-GRASP deserves special note, with this scan technique providing free breathing motion-resolved reconstructions, thus making available diagnostic quality multiphase images following contrast administration.

Compressed sensing magnetic resonance cholangiopancreatography (MRCP) enables a major reduction in scan time for this specific application. At 1.5T when applied to a conventional sequence, CS enables imaging in as little as 1/3rd of the original scan time. At 3T, diagnostic quality single breath-hold MRCP scans are a very viable clinical alternative (Fig. 3) [4]. Given the long scan time of conventional MRCP scans and the associated motion artifacts, CS MRCP exams are advocated for improved diagnosis and reduced exam time.

In cardiac imaging, compressed sensing variants are available for myocardial perfusion and CINE imaging. Single breath-hold 3D CS CINE imaging of the left ventricle is also available, offering an alternative to conventional 2D CINE with multiple breath-holds. Acceleration using CS is also possible for first-pass cardiac perfusion, providing quantification of myocardial blood flow while allowing increased anatomic coverage and higher spatial resolution.

In musculoskeletal imaging, CS versions of SEMAC have made high quality metal artifact reduction clinically feasible. SEMAC was previously limited by its long scan times, with CS permitting a marked acceleration of the acquisition

¹ Work in progress: the application is currently under development and is not for sale in the U.S. and in other countries. Its future availability cannot be ensured.



3 Magnetic resonance cholangiopancreatography (3D acquisition), cholangiocarcinoma invading the portal hilum, comparison of a conventional seven minute acquisition and a breath-hold (16 second) compressed sensing (CS) exam. There is marked degradation of the conventional scan due to breathing artifacts. Note the substantial improved depiction of dilated intrahepatic ducts (arrowheads) on the CS exam. Adapted with permission from Invest Radiol 2017;52:612-9.

with excellent resultant image quality. Scan times of 2 to 6 minutes are now routine with this technique.

Compressed sensing applications have even been demonstrated for the brain, where specialty exams with a lengthy scan time are candidates. Double inversion recovery, which finds clinical use in multiple sclerosis (for improved detection of cortical lesions), can be acquired with compressed sensing, reducing scan time in half (down to about 3 minutes). Time of flight MRA is another lengthy scan technique where the application of compressed sensing has been demonstrated, halving scan time yet providing equivalent diagnostic information.

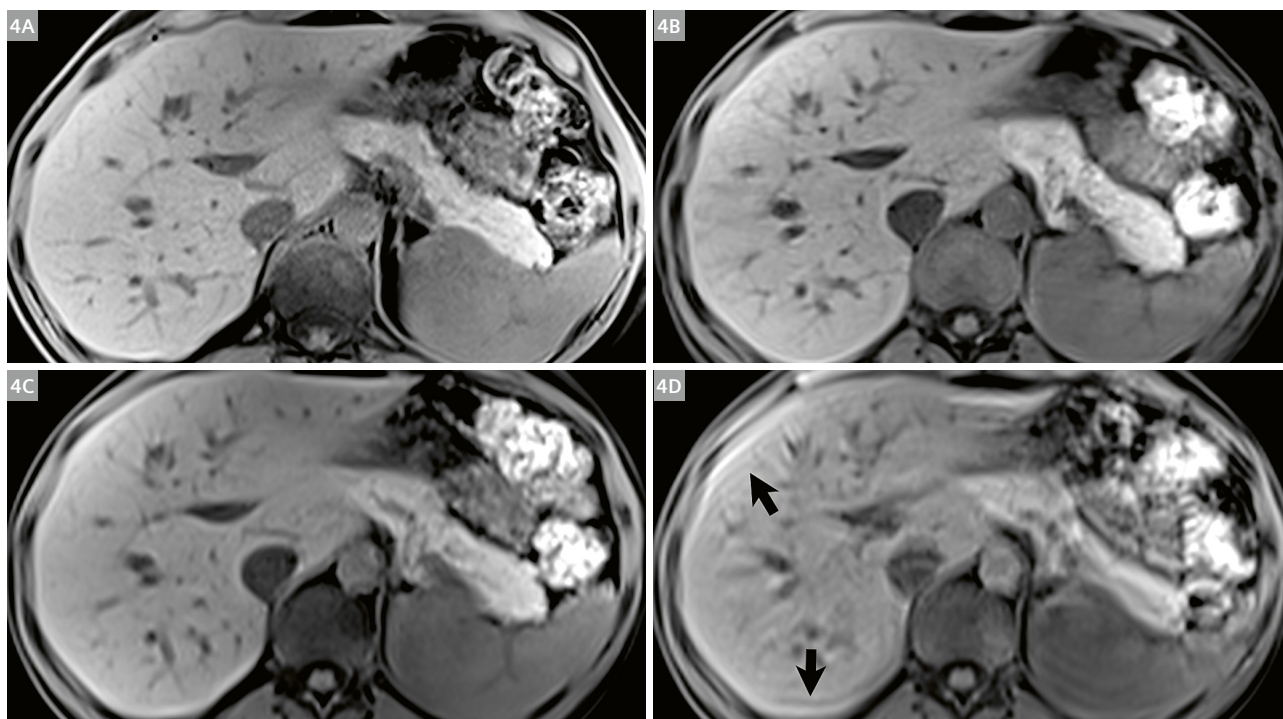
GRASP (Golden-angle radial sparse parallel imaging)

StarVIBE employs radial acquisition in-plane in combination with a fat-suppressed spoiled gradient-echo sequence. Extending this to 3D, with Cartesian sampling in the z-direction, this approach is known as a stack-of-stars (*k*-space trajectory). In-plane the acquisition is radial, through-plane it is Cartesian. The scan sequence can tolerate moderate under-sampling and is motion robust. StarVIBE was first used in liver imaging ten years or so ago. Today it has

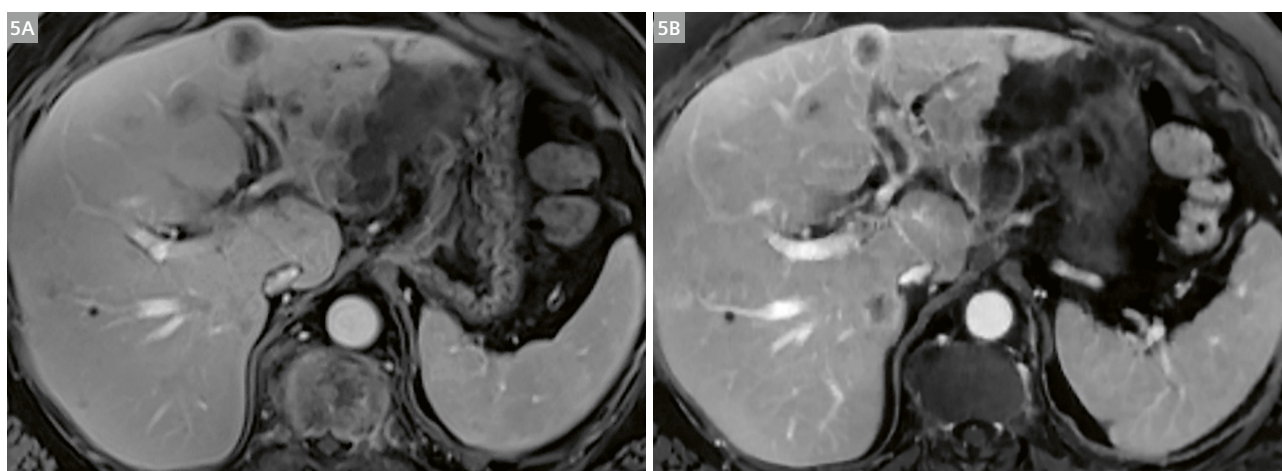
applicability in many different body regions, for example the orbits, the head and neck, the chest, the abdomen and the bowel, as well as in pediatric imaging². When acquired with golden-angle radial sampling, retrospective gating is possible and the sequence itself can provide the respiratory signal (self-gating). Self-gated isotropic radial scans have been used for example following Eovist/Primovist injection to demonstrate the hepatobiliary excretion of the contrast agent. The image quality is superior using this approach to conventional StarVIBE.

With golden-angle radial sampling, the consecutively acquired spokes cover *k*-space almost uniformly when the total spokes constitute a Fibonacci number (a series of numbers in which each is the sum of the two preceding). Temporal resolution can likewise be adjusted. Using this sampling approach, data acquisition is not repetitive over the whole scan but instead can be considered temporally incoherent, a necessary condition for compressed sensing. StarVIBE thus evolves, in combination with the use of compressed sensing reconstruction, to GRASP-VIBE (Fig. 4).

² MR scanning has not been established as safe for imaging fetuses and infants less than two years of age. The responsible physician must evaluate the benefits of the MR examination compared to those of other imaging procedures.



4 Comparing breath-hold VIBE and GRASP during normal breathing for liver imaging. High-resolution VIBE (**4A**) is compared with a slightly lower resolution GRASP scan (**4B** obtained during free-breathing), a VIBE scan with resolution close to that of the GRASP scan (**4C**) and the VIBE scan obtained without breath-holding (**4D**). Respiratory artifacts (arrows) markedly degrade VIBE scans when acquired during normal breathing, or as common in certain patient populations, without a good breath-hold. Scan times were all within the range used normally for breath-hold scans (10–20 sec). As expected, GRASP and the breath-hold VIBE scan with matched voxel size are of equivalent image quality. The high resolution breath-hold VIBE scan offers the best image quality in the current comparison (due to the spatial resolution and the excellent breath-hold), although this is not achievable in many elderly patients. Adapted with permission from *Invest Radiol* 2019;54:383-95.



5 Free-breathing scans can provide image quality comparable to breath-hold scans, a time-saving strategy that makes post-contrast imaging feasible for patients who cannot hold their breath. This is illustrated with the comparison of breath-hold VIBE (**5A**) and free-breathing XD-VIBE (**5B**) scans, both in the venous phase. Multiple liver metastases from colorectal cancer are visualized by both exams, with XD-VIBE superior in this instance due to better contrast timing. XD-VIBE is a Cartesian acquisition that enables motion state reconstruction. It provides during free breathing excellent image quality, good temporal resolution, and accurate lesion detection.
Adapted with permission from Invest Radiol 2017;52:708–714.

Free-breathing contrast-enhanced multiphase liver MR becomes possible, with flexible spatiotemporal resolution tailored to clinical needs. Self-gating is an integrated part, reducing the impact of respiratory motion.

GRASP-VIBE (which is also referred to as simply GRASP) is extremely useful in dynamic abdominal MR for patients who cannot cooperate with breathing instructions or who have difficulty holding their breath. Using this free breathing approach, liver perfusion metrics (including specifically total plasma flow, portal venous flow, arterial perfusion fraction, mean transit time and hepatocellular uptake rate – the latter if Eovist/Primovist is administered) can also be acquired, without an additional contrast injection or additional scan time. Outside of the liver, GRASP-VIBE finds many other applications, due to its inherent robustness to motion, including the female pelvis and prostate/rectum.

By including respiratory motion state resolved reconstruction GRASP-VIBE further evolves to XD-GRASP.¹ Instead of including only data from a certain motion window, the data is binned into multiple different motion states which are then likewise reconstructed. This approach can further improve image quality. Arterial phase reconstructions with XD-GRASP, acquired in free-breathing, can potentially surpass conventional breath-hold Cartesian acquisition in terms of image quality. Breath-hold scans can suffer due to limitations imposed by balancing temporal and spatial resolution with the need for anatomic coverage and also from the transient dyspnea seen with Eovist/Primovist.

Compressed sensing variants have been developed as well for Cartesian *k*-space sampling strategies. CS-VIBE is the Cartesian counterpart to respiratory gated

GRASP. XD-VIBE¹ is the Cartesian counterpart to XD-GRASP. Both CS-VIBE and XD-VIBE allow dynamic, self-gated data acquisition with free-breathing [5]. Like their radial counterparts, CS-VIBE uses data from the dominating motion state for a given gating acceptance, whereas XD-VIBE bins the data into different motion states and provides motion state resolved images (Fig. 5). Both approaches have been shown to be useful clinically.

Respiratory Sensing

Today, patient respiration is automatically monitored by a coil that lies within the patient table (and is more specifically part of the spine coil insert). This represents a major innovation, providing substantial time savings. Respiratory monitoring with a bellows type device, allowing respiratory gating for image acquisition and reconstruction, has a long history in MR. It was first suggested in 1984 [6], but requires substantial setup time and offers a poor solution for efficient respiratory gated scan acquisition. Navigator echoes were subsequently invented, and are still in use today, but have the disadvantages of requiring operator setup, being prone to misplacement, and requiring time within the scan sequence.

In contrast to these older approaches, using a respiratory sensor embedded in the table requires no setup, is automatic, and provides a reliable, reproducible respiratory trace. The signal itself is generated from a single simple, transmit/receive loop coil. To allow the signal to be differ-

¹ Work in progress: the application is currently under development and is not for sale in the U.S. and in other countries. Its future availability cannot be ensured.



6 The location of the two transmit/receive coils used for respiratory sensing are indicated on the surface of the patient table/spine coil by the lung icons (at the top and bottom). The patient can be positioned head or feet first, with the diaphragm thus lying close to one of these two coils, for detection of respiration.

entiated from that used for imaging, the coil operates at 30 MHz for 1.5 and 3T systems, far away from the Larmor frequency. Respiration causes a change in the coil loading, which leads to current changes in the coil that can be detected and monitored. A small current is fed into the coil, and the resulting current output takes the form of the respiratory cycle, with slightly higher current during inhalation and lower during exhalation.

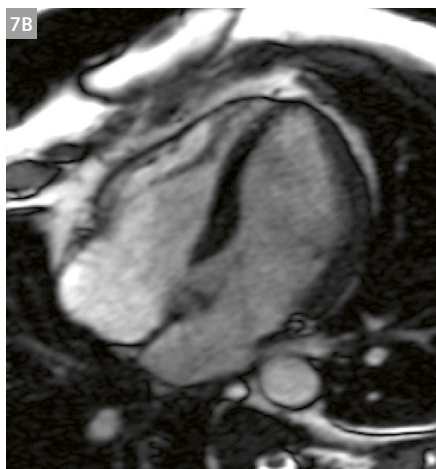
Because the coil for respiratory sensing needs to be placed near the diaphragm of the patient, there are in reality two such coils (Fig. 6). One coil is located in the appropriate place for patients positioned head first in the scanner. The other coil is used for feet-first studies, as well as for exceptionally tall or short individuals and pediatric patients.

The respiratory signal is detected and displayed as soon as the patient is placed on the scanner table, regardless of whether the patient is inside or outside of the magnet bore. In addition to its use with scan acquisition (for respiratory-triggered scans), the respiratory sensor plays an important role for patient monitoring and as a quality control measure for breath-hold scans, allowing the technologist to monitor the patient's ability to hold their breath for the duration of the scan.

Monitoring Cardiac Contraction (the Pilot Tone¹)

In the future, the ECG – as a monitoring and triggering device for MR – is likely to be replaced by direct monitoring of heart motion, using a reference radiofrequency signal described in telecommunications as a Pilot Tone¹ [7]. Such a sensor design would allow automatic capture/monitoring of the cardiac cycle, to some extent like that provided today but using different principles by the respiratory sensor. There are many negatives to the use of the ECG. These include the difficulty and time consumed for placement of the leads, the poor signal sometimes obtained, and the artifacts contaminating the observed signal. Particularly at higher field strengths, the MR gradients and the magnetohydrodynamic effect cause artifacts in the ECG, leading to poor triggering. Blood, a conductive fluid, when flowing through a magnetic field induces a voltage – a well-known phenomenon in fluid mechanics, the magnetohydrodynamic effect. This causes a change in the observed ECG – which can interfere with gating as well as masking cardiac ischemia in the observed ECG, when the patient is in an MR scanner, and is greater at 3T when compared to 1.5T.

For MR, a small magnetic field generator embedded in an anterior coil generates the Pilot Tone. That signal is then modulated by heart motion, more specifically the changes



7 Early-diastolic images, comparing that triggered by the use of the Pilot Tone (7A) vs the ECG (7B), from a cardiac cine scan, courtesy of Mario Bacher (Siemens Healthineers).

in conductive geometry, and sampled using local receive coils. This signal correlates well with the ECG, is detectable during free breathing, and can be used to acquire high quality images of the heart. The frequency used for the Pilot Tone is just outside that employed for image reconstruction (the Larmor frequency). This design should generate a much more robust signal than that from the ECG. Flexible trigger time point placement is also possible, unlike with the ECG, triggering for example at maximum cardiac contraction. This single device will also provide both cardiac and respiratory signals, as both influence the Pilot Tone. Figure 7 shows good correlation between images acquired with the Pilot Tone and the ECG. Whether this additional way to observe respiration will be further developed lies in the future.

In terms of clinical utilization, receive coils are already available containing the necessary hardware, with implementation of the Pilot Tone sensor system ongoing in next generation MR systems.

A potential advantage of Pilot Tone navigation – in addition to the ease of use – is that cardiac volume is measured directly as opposed to observation of the electrical activity of the heart (by the ECG). Any trigger time point can also be used, during the cardiac cycle, as previously noted. Pilot Tone navigation can be employed with any scan sequence, and unlike navigator echoes does not require the use of additional RF pulses.

Summary

Five important innovations for MR scanning are described, all with a very positive affect upon patient throughput. Simultaneous multi-slice offers with many scan techniques a method to halve scan time. Compressed sensing also offers a major reduction in scan time, by utilizing the concept of data sparsity and a sophisticated algorithmic approach. Its applicability is widespread in terms of types of patient studies, including brain, cardiac, abdominal, and musculoskeletal exams. Compressed sensing further makes possible many advanced imaging techniques including GRASP and its variants. This scan sequence group has its major impact in abdominal and pelvic imaging. Extremely important as well are two major hardware advances – automatic respiratory sensing and, using the Pilot Tone¹, cardiac monitoring/gating, both enabling from a clinical perspective a major reduction in set up time. Also achieved is excellent image quality and access to scan techniques that require high quality physiologic input.

Acknowledgment

Portions of the text as well as the figures are adapted with permission from “The Physics of Clinical MR Taught Through Images”, 5th edition and reference #1.

References

- 1 Runge VM, Richter JK, Heverhagen JT. Motion in Magnetic Resonance: New Paradigms for Improved Clinical Diagnosis. *Invest Radiol.* 2019;54(7):383-95.
- 2 Runge VM, Richter JK, Heverhagen JT. Speed in Clinical Magnetic Resonance. *Invest Radiol.* 2017;52(1):1-17.
- 3 Runge VM, Heverhagen JT. Advocating Development of Next Generation, Advanced Design Low-Field MR Systems. *Invest Radiol.* 2020;55(12):747-53.
- 4 Yoon JH, Lee SM, Kang HJ, et al. Clinical Feasibility of 3-Dimensional Magnetic Resonance Cholangiopancreatography Using Compressed Sensing: Comparison of Image Quality and Diagnostic Performance. *Invest Radiol.* 2017;52(10):612-9.
- 5 Kaltenbach B, Bucher AM, Wichmann JL, et al. Dynamic Liver Magnetic Resonance Imaging in Free-Breathing: Feasibility of a Cartesian T1-Weighted Acquisition Technique With Compressed Sensing and Additional Self-Navigation Signal for Hard-Gated and Motion-Resolved Reconstruction. *Invest Radiol.* 2017;52(11):708-14.
- 6 Runge VM, Clanton JA, Partain CL, James AE, Jr. Respiratory gating in magnetic resonance imaging at 0.5 Tesla. *Radiology.* 1984;151(2):521-3.
- 7 Vahle T, Bacher M, Rigie D, et al. Respiratory Motion Detection and Correction for MR Using the Pilot Tone: Applications for MR and Simultaneous PET/MR Examinations. *Invest Radiol.* 2020;55(3):153-9.



Contact

Professor Dr. med. Val Murray Runge
Editor-in-Chief, Investigative Radiology
Department of Diagnostic, Interventional
and Pediatric Radiology
University Hospital of Bern, Inselspital
Bern
Switzerland
ValMurray.Runge@insel.ch

¹ Work in progress: the application is currently under development and is not for sale in the U.S. and in other countries. Its future availability cannot be ensured.

Initial Clinical Experience with an Iterative Denoising Algorithm Applied to Reduced-data 2D Turbo Spin Echo Acquisitions

Johan Dehem, M.D.¹; Stephan Kannengießer, Ph.D.²; Uvo Christoph Hoelscher, Ph.D.²

¹Jan Yperman Ziekenhuis, Ieper, Belgium

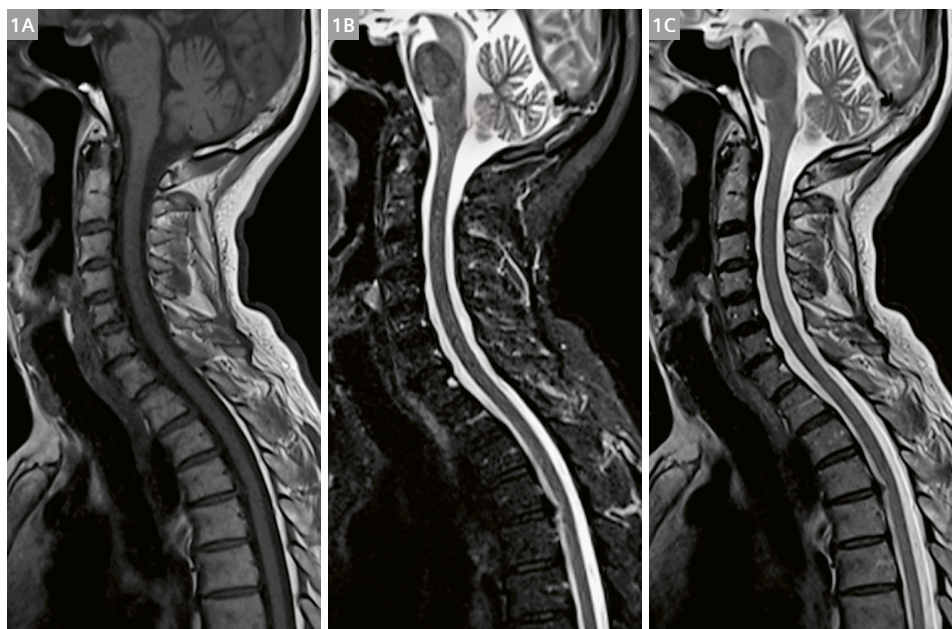
²Siemens Healthineers, Erlangen, Germany

Introduction

Magnetic Resonance Imaging (MRI) with standard 2D Turbo Spin Echo (TSE) sequences is a trusted technique to guarantee excellent soft tissue contrast in musculoskeletal (MSK), neurological, and abdominal imaging. The signal and contrast behavior are well understood and appreciated by the reading radiologist and referring physicians alike. The acquisition time of these 2D TSE sequences is in the order of several minutes, hence has always been a point of attention. With the introduction of parallel imaging [1], acquisition times could be sped up, typically by an acceleration factor (p) of two or three, by only acquiring a fraction of the data lines in k -space and calculating the missing data lines taking into account the coil-sensitivity profiles. The well-known standard 2D TSE soft tissue contrast behavior is not affected by this acceleration. However, as a rule of thumb, higher acceleration factors do induce some noise in the image by a factor of $\sqrt{p} \cdot G$ where G stands for geometry factor (G is close to 1 in a perfect system), limit-

ing the practical acceleration factor to two or three. Note that it is common practice to combine parallel imaging and multiple averages, since motion effects can be minimized by the shorter acquisition times of the former, while regaining SNR with the latter, which has advantages over un-accelerated acquisitions of the same duration.

At the same time elaborate denoising methods have been developed which have to balance noise removal and preservation of details [2]. A recently introduced acceleration technique with strong data under-sampling, allowing for significantly higher acceleration factors, for example five or higher, is Compressed Sensing (CS) [3]. CS works best in combination with random undersampling of multi-dimensional data, and the reconstruction algorithm can achieve both image restoration and denoising. Pushed to the limit, the CS images may appear unnatural, so that both radiologist and referring physician need to get used to this new sequence, to gain experience with a new



1 Parallel imaging p_2 : halving acquisition time with acceleration factor 2 comes with a signal loss by $\sqrt{2} \cdot G$, best noticeable in the T2 stir images; acquisition time 46 seconds T1 TSE (**1A**), 47 seconds T2 IR TSE (**1B**), and 68 seconds T2 TSE (**1C**).

signal and contrast behavior, a new look and feel of the soft tissue contrast. Regular 2D TSE data does not seem to be optimal for CS reconstruction.

Image reconstruction based on artificial intelligence (AI) / deep learning (DL) is the latest development capable of denoising [4]. These techniques, however, require large amounts of training data, which was beyond the scope of this study.

Iterative denoising (ID) is a technique which uses similar noise-suppressing operations as Compressed Sensing, but which is specifically designed to be combined with standard parallel imaging and other standard imaging techniques, allowing for shorter scan times and/or higher resolution while compensating for the resultant SNR loss [5]. First applications focused on volumetric acquisitions [6]. This study presents initial experience with this technique applied to standard 2D TSE data in multiple body regions.

Methods and materials

The goal of this study was to investigate whether the new iterative denoising technique can compensate for the resultant SNR loss when using higher acceleration in standard 2D TSE imaging. To make this comparison between images with higher acceleration versus standard acceleration as accurate as possible, instead of rescanning patient with higher acceleration factors, higher acceleration was simulated by discarding one average from the raw data sets. By applying this simulated acceleration, it was possible to obtain datasets that are – except for the virtual acceleration – completely identical.

Eleven clinical data sets from the perineum, uterus, prostate, l-spine, and sacroiliac joint were acquired on a 1.5T clinical MR scanner (MAGNETOM Sola, Siemens Healthcare, Erlangen, Germany) with the standard turbo spin echo (TSE) sequence. Raw data allowing retrospective image reconstruction with subsets of the originally acquired averages was collected from regular patient examinations so that no additional or modified scans had to be performed. Informed consent from patients was obtained to reprocess anonymized data for clinical research. All raw data sets featured Parallel Imaging under-sampling and comprised two or more signal averages.

Data processing was performed offline and with the help of a prototype implementation of the ID algorithm as described in [4], integrated into the image reconstruction pipeline. Quantitative noise measurements were drawn from the system's adjustment framework. Taking into account all noise-modifying operations, a noise map was calculated which describes the spatial noise distribution in coil-combined, complex-valued images after the parallel imaging reconstruction [7, 8]. Then the wavelet thresholding is automatically adjusted for MMSE-optimal noise

removal according to "Stein's Unbiased Risk Estimator" (SURE) [9]. This automated parameter selection allows the algorithm to adapt to both the noise and signal characteristics of each individual image and to generalize to multiple body regions and scan protocols without additional manual tuning. Some edge enhancement was applied after the ID to compensate for perceived loss in sharpness.

From each multi-average raw data set three different versions of the images were reconstructed. The first version (called "original") used all available averages and corresponds to the regular reconstruction; it does not use the denoising algorithm. To simulate accelerated acquisition, the second reconstruction version discarded one signal average from the raw data sets, e.g. one out of two; it also did not use the iterative denoising algorithm and is called "accelerated". The third reconstruction version discarded the same signal average from the raw data sets, and additionally applied the described iterative denoising algorithm. These images are called "accelerated + ID".

The versions "accelerated" and "accelerated + ID" simulate accelerated acquisition by lowering the number of averages. With this simulation approach the three versions are based upon as similar data sets as possible so that they can be directly compared. They derive from the same acquisition so that all variations between repeated scans can be avoided. However, the data is not identical because version two and three only use a subset of the data. Hence effects like physiological motion still can have a different effect on the different versions – especially if the motion happens during the discarded part of the raw data.

The described versions of the images were viewed side-by-side on an open source DICOM viewer (Horos™) and ranked by an experienced radiologist according to image quality in terms of perceived signal to noise ratio as well as noticeable artifacts like blurring. Any non-diagnostic image quality was marked. Given the obvious differences between the image versions, no effort at blinding was made.

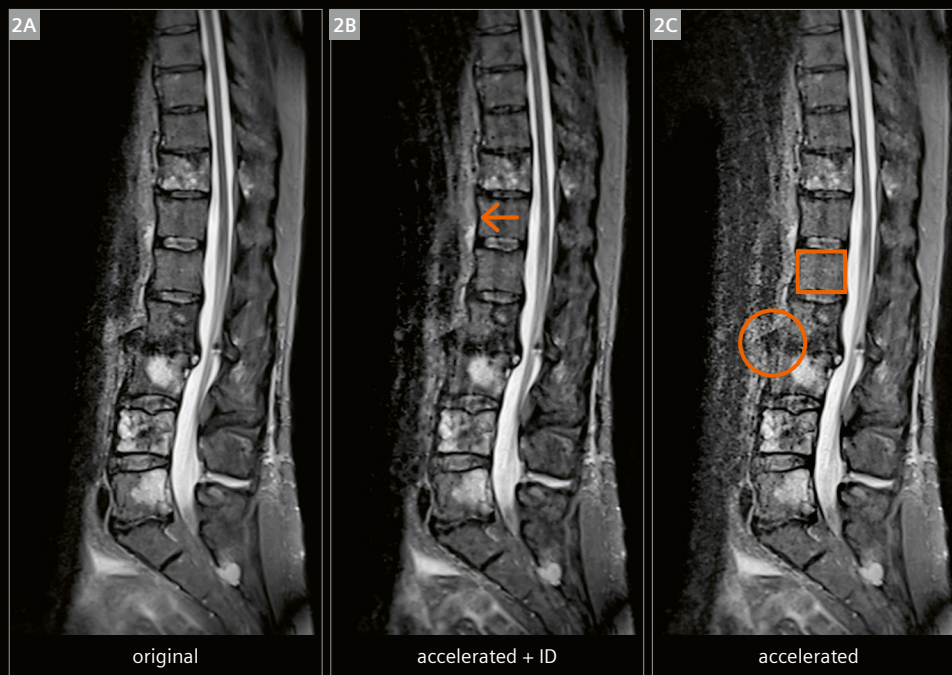
Results

Table 1 lists the ranking results. In 10 out of 11 cases (91%), the "original" version was ranked best. Of the "accelerated" versions, study 2 (Figs. 2, 3) is no longer diagnostic (marked as X). All "accelerated + ID" versions were ranked better than the "accelerated" versions, and all were diagnostic. In study 5 (Fig. 5) the image quality in the "accelerated + ID" version equals the image quality of the "original" version. In study 11 (Figs. 7, 8) the image quality of the "original" is less than the image quality of both the "accelerated + ID" images and "accelerated" images. Example image features are described in the figure captions.

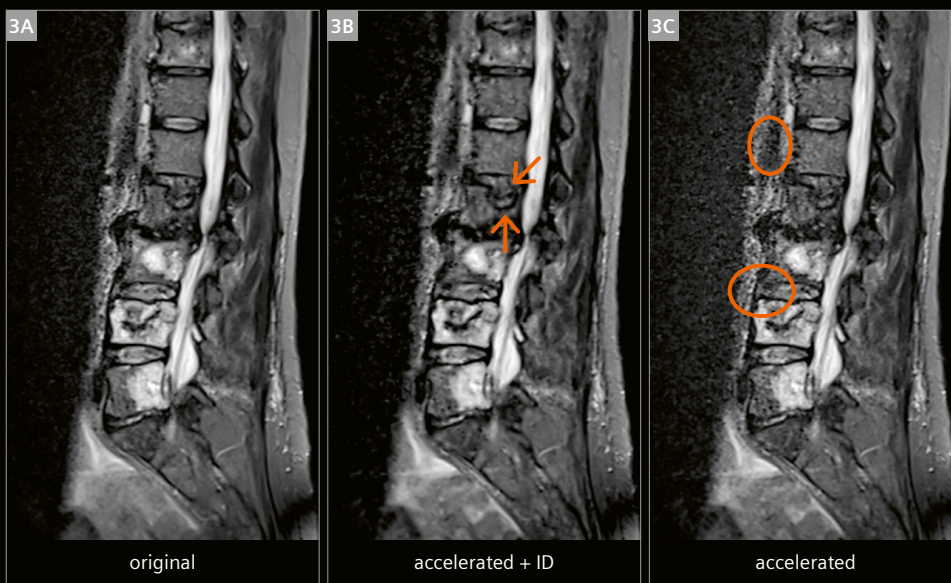
study #	contrast	# of averages, [timesaving]	best image	2 nd best image	3 rd best image
1	STIR SI joint, cor	2 [50%]	"original"	"accelerated + ID"	"accelerated"
2	STIR L-spine, sag	2 [50%]	"original"	"accelerated + ID"	"accelerated" (X)
3	T1 L-spine, sag	2 [50%]	"original"	"accelerated + ID"	"accelerated"
4	T1 L-spine, sag	2 [50%]	"original"	"accelerated + ID"	"accelerated"
5	T2 uterus, cor	3 [33%]	"original" = "accelerated + ID"	"accelerated"	–
6	T2 prostate, ax	3 [33%]	"original"	"accelerated + ID"	"accelerated"
7	STIR SI joint, cor	2 [50%]	"original"	"accelerated + ID"	"accelerated"
8	STIR SI joint, cor	2 [50%]	"original"	"accelerated + ID"	"accelerated"
9	STIR SI joint, cor	2 [50%]	"original"	"accelerated + ID"	"accelerated"
10	T2 uterus, sag	2 [50%]	"original"	"accelerated + ID"	"accelerated"
11	T2 perineum, ax	4 [25%]	"accelerated + ID"	"accelerated"	"original"

Table 1: Results from the side-by-side reading of an experienced radiologist.

Study 2

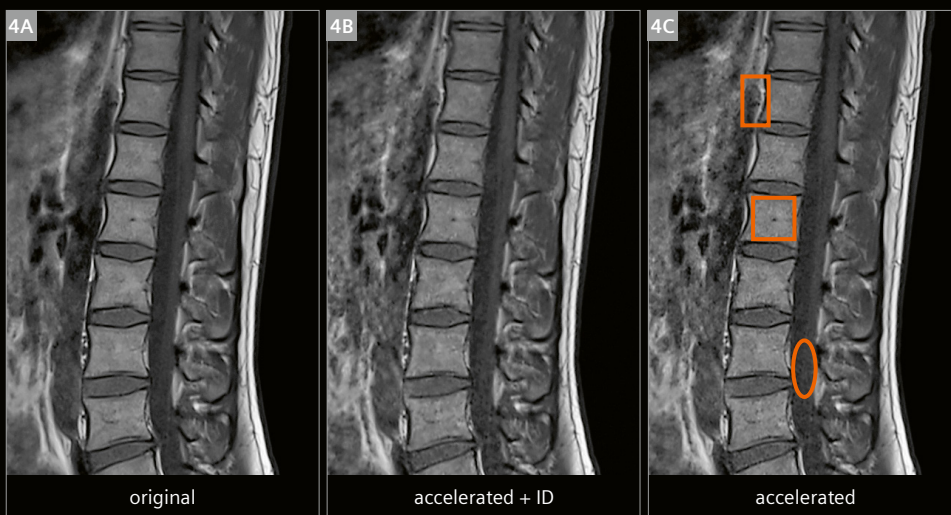


- 2** The "original" version (2A) with two averages has the best image quality since two averages are effectively averaging out the ghosting artifact. On top of the ghosting, version "accelerated" (2C) has a very low SNR with a "grainy unsharpness" e.g. in the body of vertebra L1 (square box) or prevertebral space (red circle) and intervertebral space level L2–L3 making this image non-diagnostic. In version "accelerated + ID" (2B) the "grainy blurriness" is effectively removed (arrow points to substantial SNR gain in prevertebral space). This leads to a still challenging but more diagnostic image quality resembling the morphology and contrast of the "original" version, e.g. in the endplates L2–L3. Simulated acquisition time saving: 50%. Scanning parameters: TE 99 ms, TR 4570 ms, TI 140 ms, duration for original (two averages) 1:17 min.



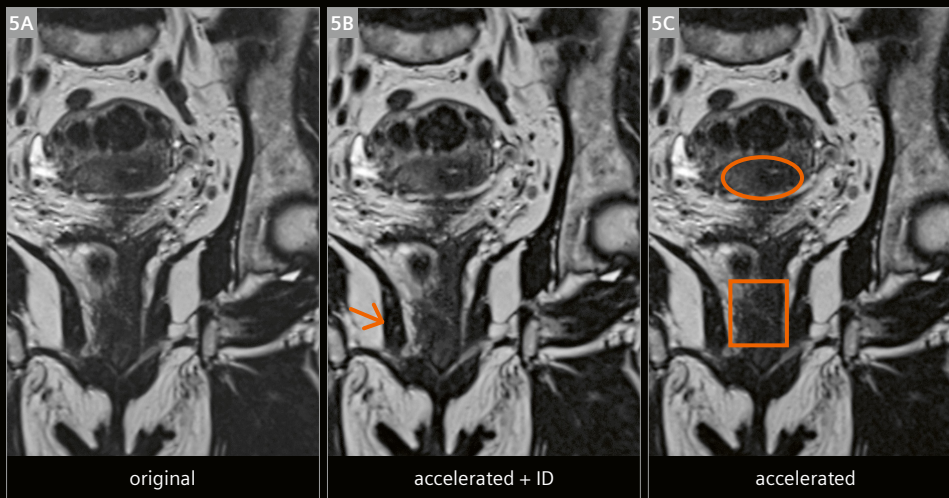
3 Same patient as Figure 1. Image zoomed in and slightly off midline. Version “accelerated” (3C) is severely impaired by both low SNR and ghosting artifact. The exaggerated noise level makes it of questionable diagnostic value (red circles indicate low SNR). Version “accelerated + ID” (3B) still suffers from ghosting artifact, however the ID algorithm processing of the image effectively removes the grainy pattern over the vertebral bodies and prevertebral fat plane. The resulting image quality improvement makes it easy to delineate the intravertebral disc herniation (red arrows).

Study 3



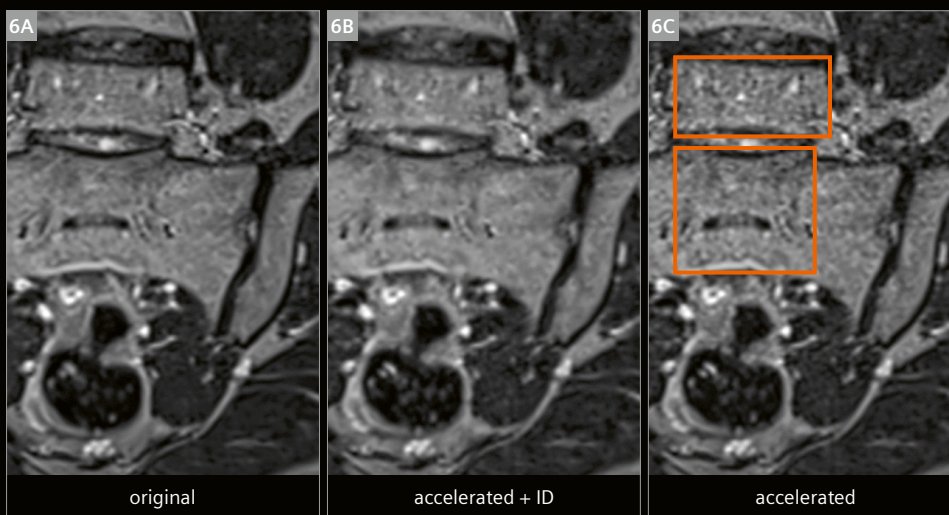
4 The “original” version (4A) with two averages has crisp image quality in this “perfect patient”. Version “accelerated” (4C) features an exaggerated noise level in comparison to the “original” (red squares). The SNR of version “accelerated + ID” (4B) is still lower than in the “original” version; however, in comparison to the “accelerated” version SNR is clearly higher. Simulated acquisition time saving: 50%. Scanning parameters: TE 8 ms, TR 603 ms, duration for original 1:38 min.

Study 5



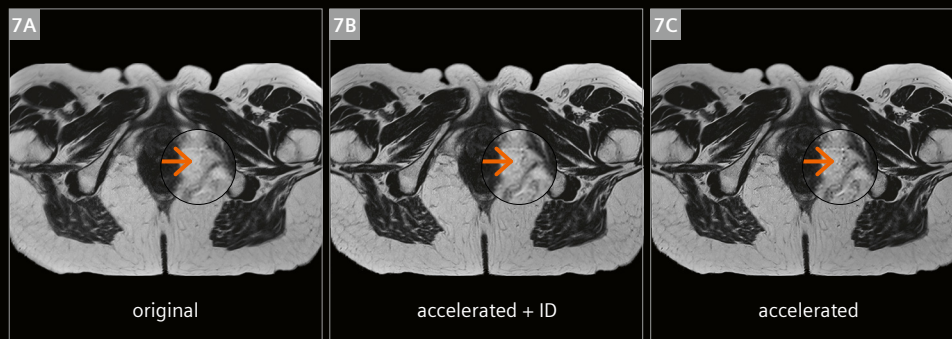
- 5** All three images are of diagnostic quality with high signal. Some graininess indicating lower SNR is present in the "accelerated" image (5C) over the uterus (red oval) and vagina (red box). This grainy superposition is removed after ID in version "accelerated + ID" (5B). The resulting image in version "accelerated + ID" (center) matches very closely the image quality of the "original" version (5A). The version "accelerated + ID" (center) has the highest overall SNR without graininess. Taking a closer look at details e.g. the fatty streaks in the right ischiococcygeal muscle (red arrow): these small fatty streaks are depicted with the same confidence as on the original image, indicating that no image detail is lost during ID. Simulated time saving: 33%. Scanning parameters: TE 132 ms, TR 7780 ms, duration for original 1:25 min.

Study 7

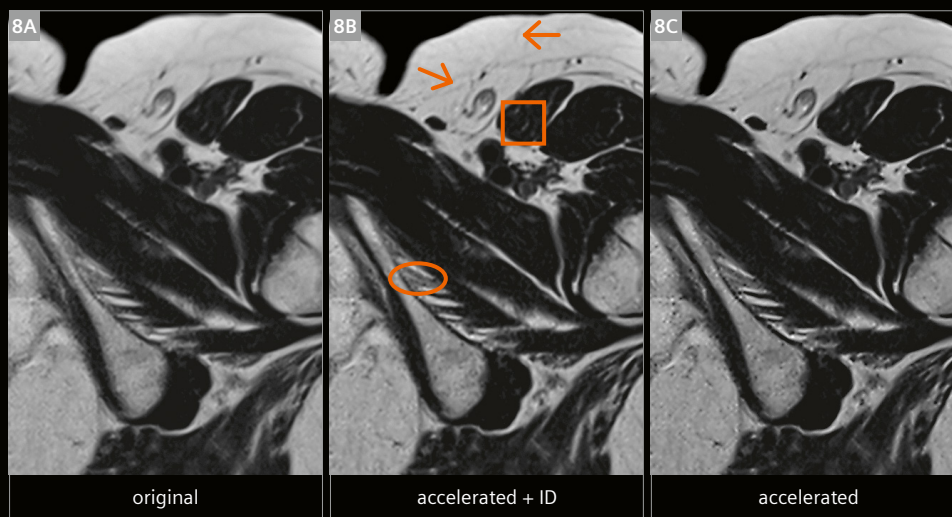


- 6** The "original" version (6A) with two averages has the best image quality. Version "accelerated" (6C) has a low signal to noise with impressive "graininess" (square boxes) over the fifth lumbar and first sacral vertebra. In version "accelerated + ID" (6B) the overlying "graininess" is effectively removed resulting in an image with SNR resembling the "original" version. Simulated acquisition time saving: 50%. Scanning parameters: TE 87 ms, TR 3400 ms, TI 140 ms, duration for original 0:52 min.

Study 11



- 7** Version "original" (7A) has abundant signal, however, some blurring is present. Version "accelerated" (right) and "accelerated + ID" (7B) have less blurring since less measurement time leads to less patient movement, but still have abundant signal. This abundance in signal results in an image quality where for instance the veins in the ischiorectal fossa are better depicted in both versions "accelerated" (7C) and "accelerated + ID" (center) than on the original version. Although high enough SNR is present in version "accelerated" (right), ID further enhances the image quality in "accelerated + ID" (center) image: the small venous bifurcation (red arrow, magnifying glass) in the left ischiorectal fossa is better depicted after ID (center). Simulated time saving: 25%. Scanning parameters: TE 106 ms, TR 814 ms, duration for original 4:12 min.



- 8** Same study as Figure 7: In version "original" (8A) the small fibrous strands in subcutaneous fat are hard to depict even though they are clearly present on the "accelerated" version (8C) and really stand out on the "accelerated + ID" version (red arrows). The fatty streaks (red circle) in between the muscle fibers of the external obturator cannot be seen on the "original" version, they are however visible on the "accelerated" version and really stand out on the "accelerated + ID" version (8B). The ID algorithm does not only increase SNR but also enhances image details, for example the fatty streaks in the iliac muscle (red box). The internal structure with fat-containing hilum of the left inguinal lymph node (between the red arrow and red box) is again best depicted on the "accelerated + ID" version. Simulated time saving: 25%. Scanning parameters: TE 106 ms, TR 814 ms, duration for original 4:12 min.

Discussion

Acquiring a dataset that is substantially accelerated (by reducing the number of averages) leads to a discernible drop in signal to noise ratio. This is rendering the resulting images grainy and harder or even sometimes impossible to interpret, with an obvious drop in image quality in comparison to the "original" images. The results of this small-scale study provide evidence that the process of ID as described above can compensate for the drop in signal to noise ratio in substantially accelerated 2D datasets.

In this study the perceived gain in image quality after ID was obvious in images which are already by design inherently lower in signal to noise ratio like e.g. Short-TI Inversion Recovery (STIR) imaging. Studies 7 and 8 with coronal STIR imaging of sacroiliac joints demonstrate the benefit from the ID bringing image quality back to the standard imaging quality. Apparently, ID is reducing the noise level in the signal and image quality thereby approaches the image quality of the "original" images.

Less intuitive, even in images with abundant signal, the image quality of "accelerated + ID" can be as good (study 5) or even better (study 11) than the original. A plausible explanation is that by removing an average also removes the blurring that can occur due to slight patient movement between multiples averages.

Iterative denoising, in contrast to conventional noise-removing image filters, has the advantage of supplementary quantitative noise distribution information, which would otherwise have to be estimated from the images themselves. Consequently, over- or under-filtering is inherently avoided. In combination with the SURE-optimizing iteration, this is especially important for preserving small image details and sharpness, although some additional edge enhancement appears to be beneficial. Preserved image details and sharp edges are striking in study 11 (Figs. 7) where the small venous bifurcation in the left ischiofemoral fossa is clearly sharper delineated in the "accelerated + ID" image than on the images without denoising. Figure 8 is another excellent example that no

over-filtering occurs: the small septae in the subcutaneous fat are better depicted on the accelerated images with denoising when compared to the accelerated version as well as to the original version. This can be seen in the fatty streaks in the external obturator muscle.

Conclusion

Image quality in standard 2D MRI sequences, accelerated in simulation beyond the threshold of standard acceptable noise levels, can be substantially improved by applying an ID algorithm using supplementary information about the image noise level. It is expected that standard 2D MRI can profit from ID when natively scanning with lower numbers of averages and hence shorter acquisition times. More clinical studies with different clinical perspectives are required to show if ID could become as indispensable a tool in MRI as iterative reconstruction is in CT.

Acknowledgements

The authors are grateful to Dr. Boris Mailhe for developing the core of the iterative denoising technique and Dr. Carmel Hayes for her support in algorithm implementation and data processing.

References

- 1 Heidemann RM et al. A brief review of parallel magnetic resonance imaging. *European Radiology*, Vol 13 2003: 2323–2337.
- 2 Mohan J, Krishnavenib V, and Guo Y. A survey on the magnetic resonance image denoising methods. *Biomed Signal Process Control*, Vol 9 2014: 56–69.
- 3 Geethanath S et al. Compressed sensing MRI: a review. *Crit Rev Biomed Eng*, Vol 41(1) 2013: 183–204.
- 4 Lin DJ et al. Artificial Intelligence for MR Image Reconstruction: An Overview for Clinicians. *J Magn Reson Imaging* 2020 Feb 12. Online ahead of print.
- 5 Kannengiesser SAR et al. Universal iterative denoising of complex-valued volumetric MR image data using supplementary information. *Proc. Intl. Soc. Mag. Reson. Med.*, Vol 24 2016: 1779.
- 6 Kang HJ et al. Clinical Feasibility of Gadoteric Acid-Enhanced Isotropic High-Resolution 3-Dimensional Magnetic Resonance Cholangiography Using an Iterative Denoising Algorithm for Evaluation of the Biliary Anatomy of Living Liver Donors. *Invest Radiol.*, Vol 54(2) 2019: 103–109.
- 7 Breuer FA et al. General formulation for quantitative G-factor calculation in GRAPPA reconstructions. *Magn Reson Med.*, Vol 62(3) 2009: 739–46.
- 8 Kellman P, and McVeigh ER. Image reconstruction in SNR units: a general method for SNR measurement. *Magn Reson Med.*, Vol 54(6) 2005: 1439–47.
- 9 Blu F, and Lüscher T. The SURE-LET Approach to Image Denoising. *IEEE Trans Im Proc*, Vol 16:11 2007: 2778 - 2786.

Contact

Johan Dehem, M.D.
Jan Yperman Ziekenhuis
Briekestraat 12
8900 Ypres
Belgium
Phone: +32 57 35 74 00
johan.dehem@yperman.net



Deep Resolve – Mobilizing the Power of Networks

Nicolas Behl, Ph.D.

Global Marketing Manager MRI Systems, Siemens Healthineers, Erlangen, Germany

The limitations of conventional image reconstruction

MRI is established as one of the key modalities in diagnostic imaging. The absence of ionizing radiation and the unmatched soft tissue contrast distinguish MRI from other imaging modalities. While these features have helped to establish MRI as the method of choice for the diagnosis of many pathologies, the main limitation of MRI is the acquisition time.

With conventional reconstruction methods, the acceleration of an acquisition can only be achieved by accepting compromises with respect to image resolution or signal-to-noise ratio (SNR). In general, acquisition speed, image resolution, and SNR are tightly linked and increasing one of the three automatically has a negative effect on at least one of the two others (Fig. 1).

The use of receive arrays and parallel imaging has been an important breakthrough in MR image reconstruction and is an essential part of clinical routine in MRI [1, 2].

Parallel imaging, however, usually comes at the price of higher image noise, especially in regions further away from the receive coils. This results in inhomogeneous

noise distribution, especially if high acceleration factors are used. Compressed Sensing was another major development when it comes to image acceleration [3]. It benefits especially dynamic and non-cartesian 3D imaging but comes at the cost of a higher computational burden. Also, 2D cartesian imaging, which still is building the backbone of routine MR imaging, benefits less from Compressed Sensing.

Over the last years, artificial intelligence (AI) technologies have made their appearance in a various research publications [4, 5]. Especially the use of deep neural networks has proven to be helpful when trying to address the limitations of conventional MR image reconstruction, especially also for routine 2D imaging. Deep learning image reconstruction has the potential to tackle all three limiting factors of MR imaging simultaneously: image resolution, SNR, and acquisition speed.

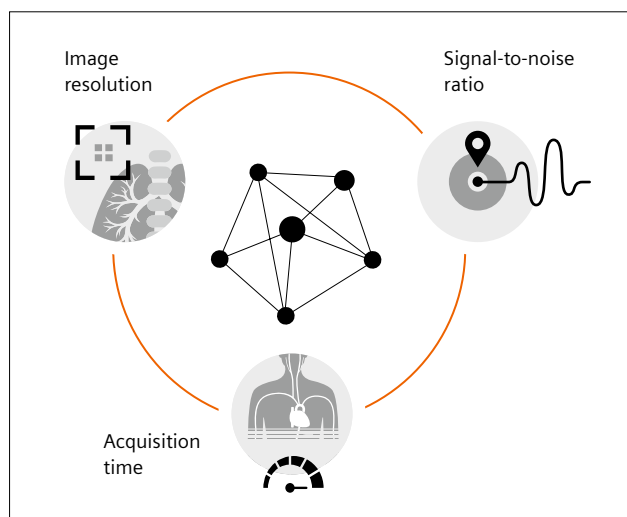
Deep Resolve Gain & Deep Resolve Sharp

Deep Resolve brings deep learning and AI to the MR image reconstruction process. Deep Resolve is an advanced reconstruction technology, which in its first step brings intelligent denoising and deep-learning-based image reconstruction directly to the core of the imaging chain.

Deep Resolve Gain is a solution for intelligent denoising. As mentioned above, in MRI, image noise is not uniformly distributed across the image. This can be due to coil array geometries since the SNR is usually higher close to the receive coils. Also the use of parallel imaging reconstruction techniques can lead to varying noise levels in the reconstructed image. These local variations in image noise can not be addressed by conventional noise filters, as these operate globally on the entire reconstructed image. Deep Resolve Gain incorporates specific noise maps, which are acquired together with the original raw data, directly into the image reconstruction [6].

These noise maps are generated without needing to spend additional scan time and can be extracted from the raw data. The reconstruction algorithm takes local noise variations into account and enables stronger denoising where noise would be most dominant when reconstructing with conventional methods.

Deep Resolve Gain helps to mitigate noise that is introduced when accelerating the acquisition e.g. by reducing

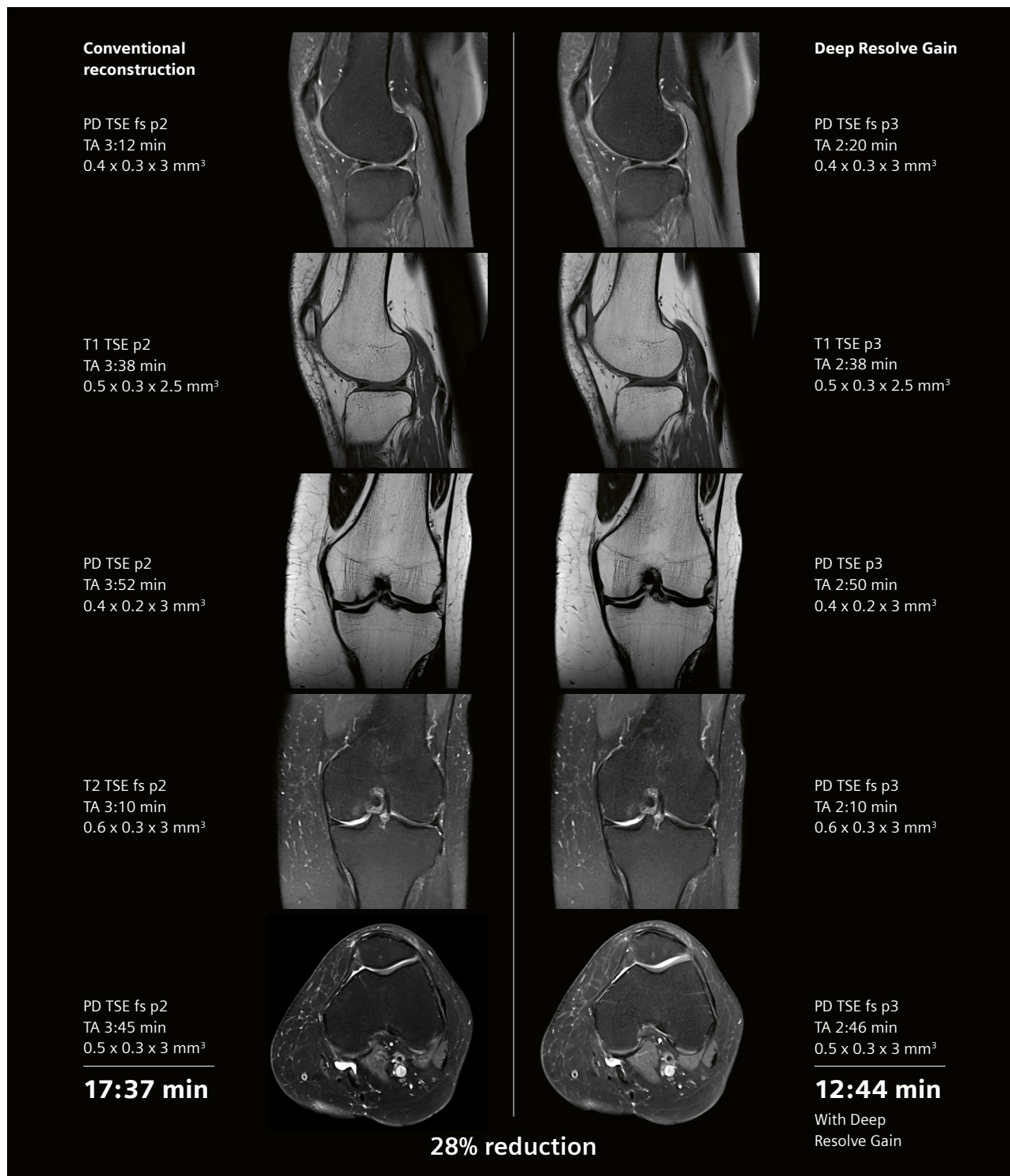


1 Image resolution, SNR, and acquisition time are the three limiting factors of MRI. Using conventional methods, changing one of them directly affects at least one of the two others. Deep learning reconstruction has the potential to disrupt this convention.

the number of averages or by increasing the acceleration factor in parallel imaging.

As the noise maps can be generated from the originally acquired raw data, no additional acquisition time is

needed, and the results are available in real-time. Figure 2 shows how Deep Resolve Gain can be employed to accelerate an entire knee exam. Images acquired with increased acceleration and reconstructed with Deep



300001620

- 2** The increase in SNR achievable with Deep Resolve enables you to accelerate entire knee exams. The targeted reduction of image noise allows for the use of higher acceleration factors, without having to pay with increased image noise. Images are acquired on a MAGNETOM Vida 3T scanner.

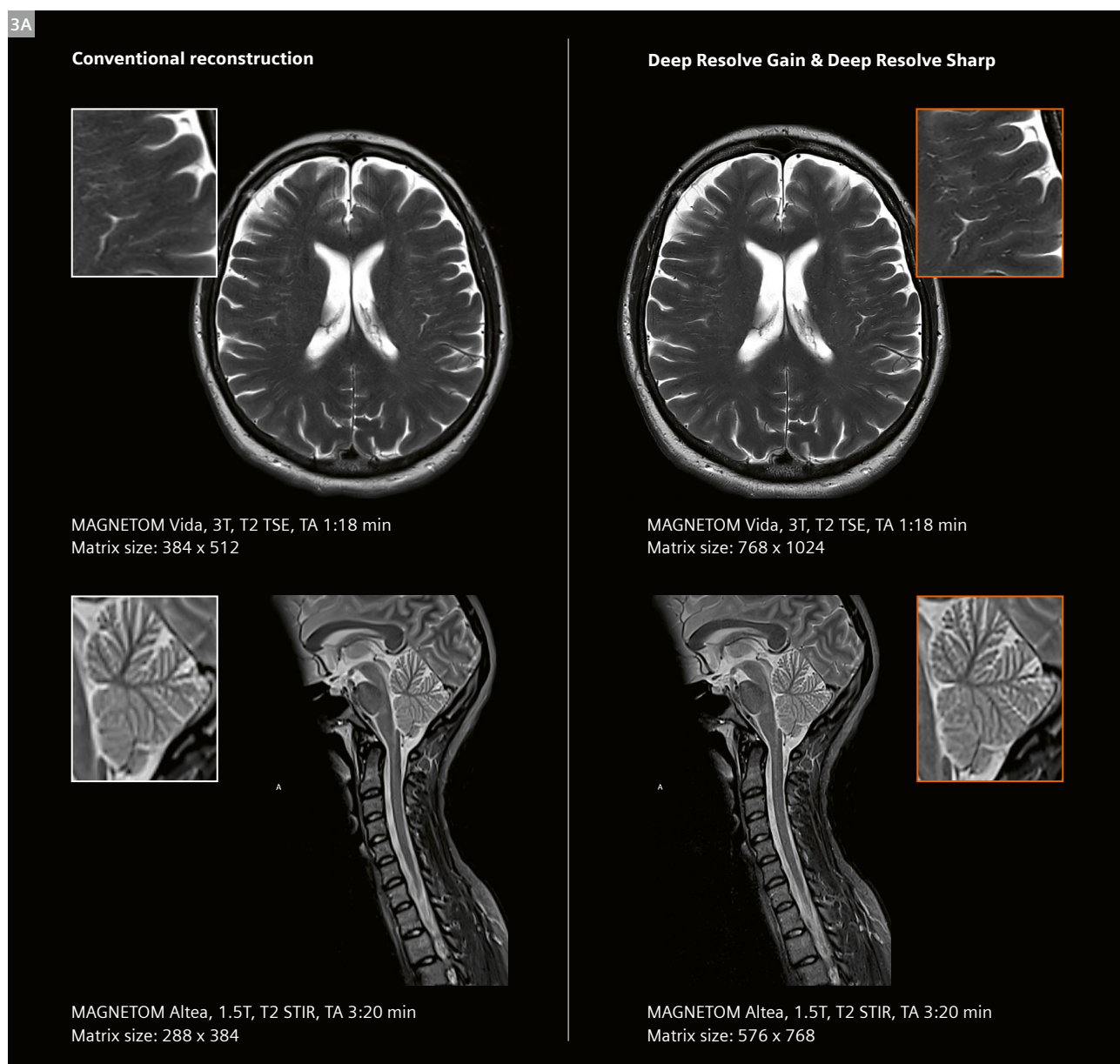
Resolve Gain are similar in quality to the standard protocols which are conventionally reconstructed. In this example it results in an acceleration by 28% over the entire exam.

Deep Resolve Sharp is a novel image reconstruction technology to generate images with increased sharpness. The deep neural network at the core of Deep Resolve Sharp generates a high-resolution image from low resolution input data. The network was trained on a large number of pairs of low-resolution and high-resolution data.

As the training data for Deep Resolve Sharp covered a wide range of anatomies, the reconstruction network can be applied to all body regions. Deep Resolve Sharp can

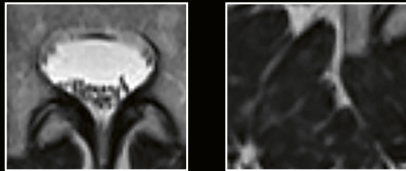
increase the matrix size by a factor of up to two along both in-plane axis, resulting in substantially increased image sharpness.

To ensure robust results, the acquired raw data is directly incorporated into the reconstruction and ensures consistency with the data from the scanner. The inclusion of the cross-check with the acquired raw data is essential for the robustness of the reconstruction and to ensure that contrasts are correctly represented in the final output. Figure 3 shows how Deep Resolve Sharp can be used to increase the sharpness of reconstructed images, without having to extend the acquisition time. Deep Resolve Sharp

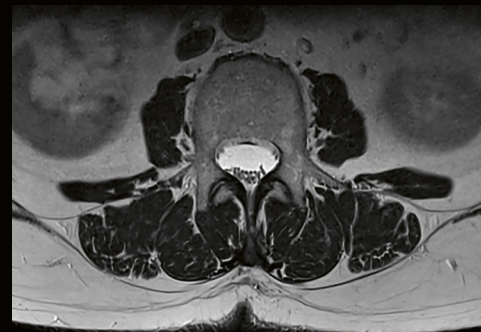
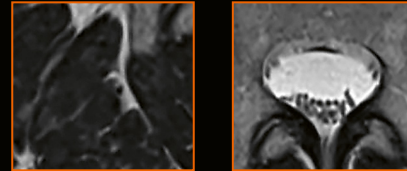


- 3** Deep Resolve Sharp uses a deep neural network to generate sharper images than ever before, enabling a clear depiction of fine structures and sharp edges. The use of raw data within the reconstruction process ensures robust results.

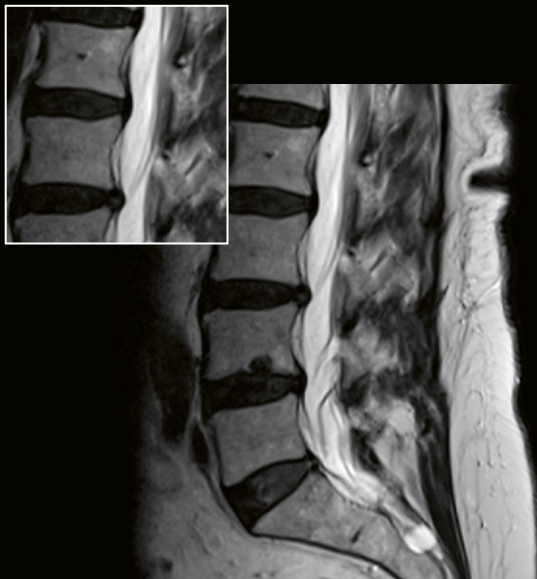
3B

Conventional reconstruction

MAGNETOM Sola, 1.5T, T2 TSE, TA 3:45 min
Matrix size: 256 x 320

Deep Resolve Gain & Deep Resolve Sharp

MAGNETOM Sola, 1.5T, T2 TSE, TA 3:45 min
Matrix size: 512 x 640



MAGNETOM Sola, 1.5T, T2 TSE, TA 2:24 min
Matrix size 307 x 384



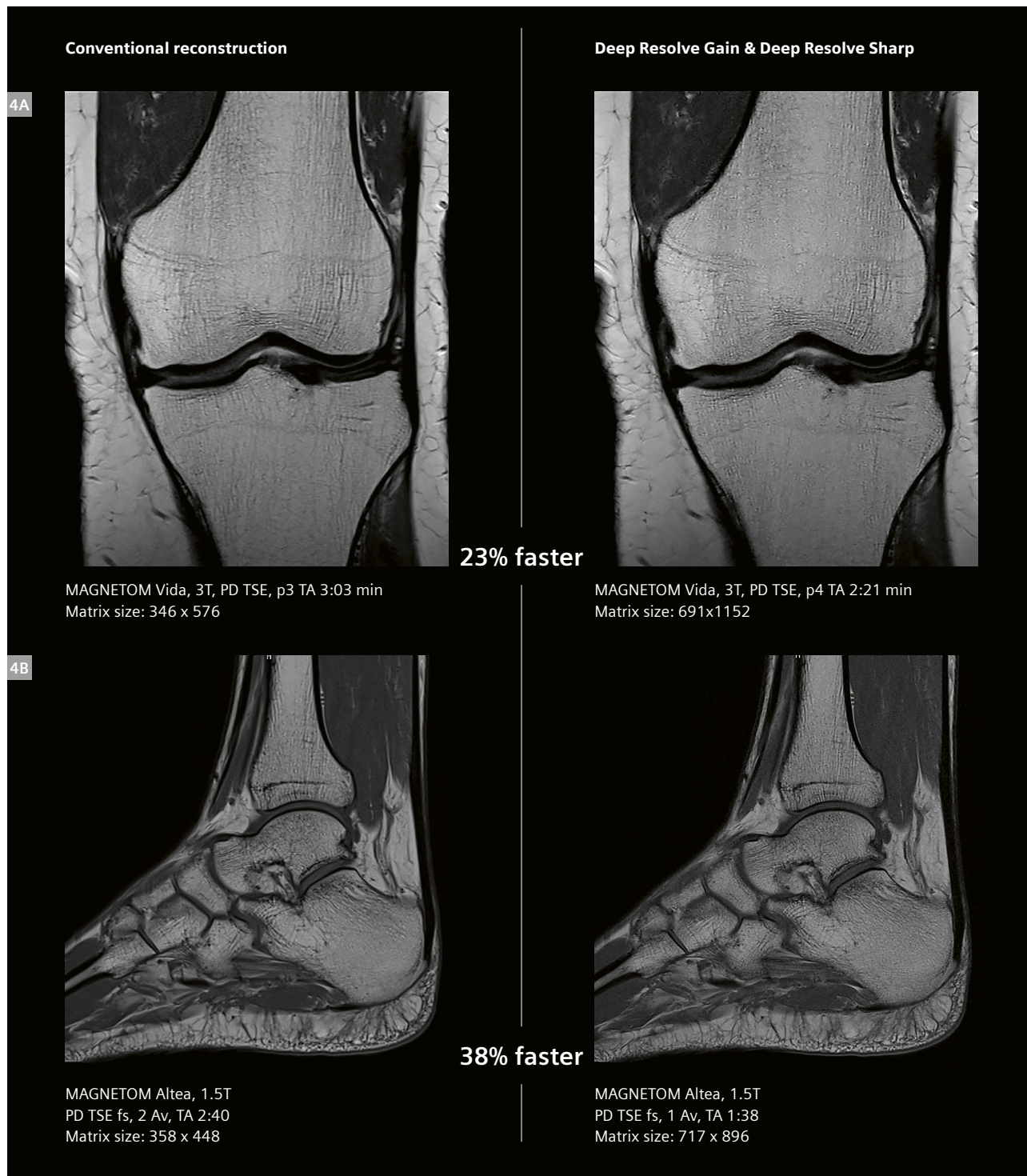
MAGNETOM Sola, 1.5T, T2 TSE, TA 2:24 min
Matrix size 614 x 768

1a0aa3595

1a0aa3588

can also be used to enable quicker scans. The phase resolution can be reduced in the acquisition and Deep Resolve Sharp can be employed to recover the resolution in the reconstruction process. An example is given in Figure 4B.

In Figure 4 you can see how Deep Resolve enables accelerated acquisition while simultaneously increasing image quality and sharpness.



- 4** Together, the Deep Resolve technologies enable faster acquisitions, while increasing the image sharpness simultaneously. The targeted denoising achieved with Deep Resolve Gain allows for the use of higher acceleration, while Deep Resolve Sharp increases the sharpness of the image by increasing the matrix size.

Technology corner

Deep Resolve Gain uses individual noise maps as input for an iterative reconstruction process. This iterative process, together with the noise maps as prior knowledge reflecting where more noise is to be expected in the image, enables an effective denoising in the reconstruction process. This is similar to the reconstruction process used in Compressed Sensing, extending it to cartesian 2D imaging. For Deep Resolve Gain, the denoising in every iteration step takes place in the wavelet-domain. Denoising in the wavelet domain is more efficient than denoising in image or frequency domain. It enables a better separation between noise and small structures that are part of the image to be reconstructed. The denoising strength of Deep Resolve Gain can be adjusted, depending on the amount of noise and personal preference.

Deep Resolve Sharp uses a deep neural network to increase the sharpness in reconstructed images. The convolutional neural network operates on complex data and enables a reduction of the voxel size by up to a factor of two along each axis in-plane compared to conventional reconstruction. During the reconstruction using Deep Resolve Sharp, the information content corresponding to the originally acquired raw data remains unaffected. Incorporating the acquired raw data along the reconstruction process ensures robust results and correct representation of image contrast. The deep neural network used in Deep Resolve Sharp is rather used to predict the contents of remote areas within k -space. Conventional reconstruction using interpolation expands k -space with zeros, therefore not adding any information or contributing to image sharpness. The neural network at the core of Deep Resolve

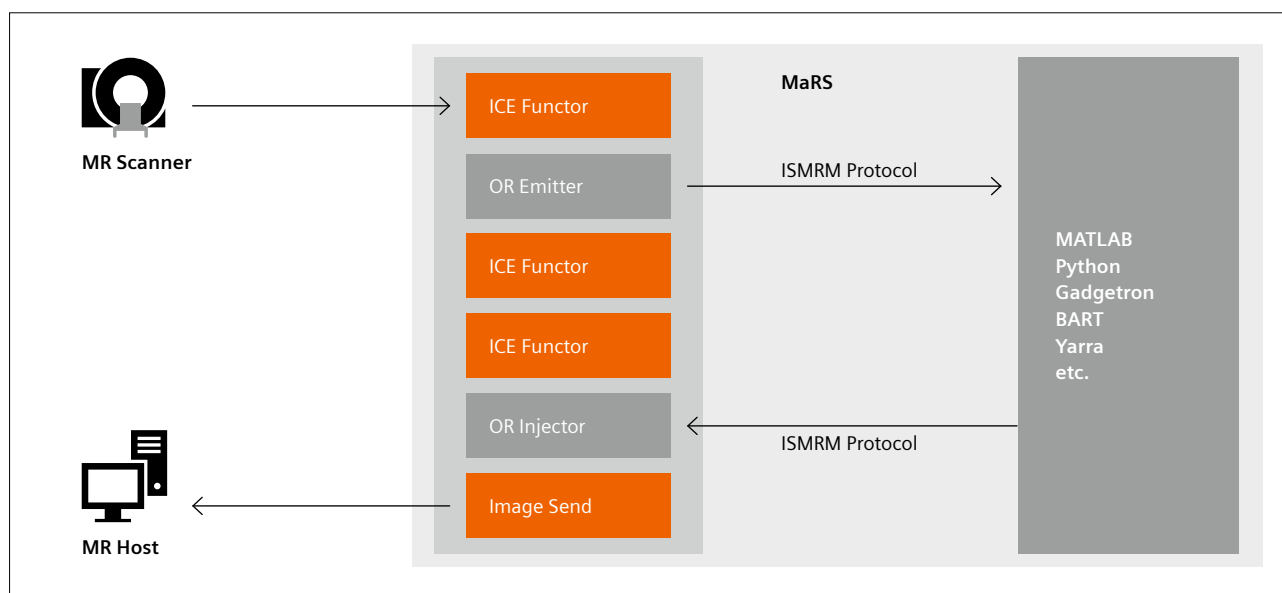
Sharp, on the other hand, was trained with a large number of pairs of low- and high-resolution data. It can therefore enhance the image with meaningful information corresponding to the outer parts of k -space, beyond the originally acquired data.

Open innovation platform¹

Deep learning reconstruction is a very active field for researchers, demonstrating great potential for the future of MR image reconstruction, including denoising, artifact reduction, and possibly even the reconstruction of multiple contrasts from one single acquisition [7]. Deep Resolve gives you access to the plentitude of deep learning applications being developed in the field. Via an open innovation interface, Deep Resolve is planned to enable our partners to position their solutions in the Digital Marketplace, powered by the teamplay Digital Health Platform.

Currently, prototyping for image reconstruction algorithms is usually done offline, which means that the raw data has to be transferred from the scanner to a workstation, where they are finally reconstructed using a prototype developed e.g. in MATLAB or Python. These reconstructions then have to be converted to DICOM again if a clinician wants to evaluate them for a clinical study. Deep Resolve is planned to facilitate clinical transition for image reconstruction prototypes by enabling online reconstruction, directly at the scanner. The open innovation protocol is designed to support open community standards, such as the ISMRM raw data format and Gadgetron (Fig. 5).

¹The product is still under development and not commercially available yet. Its future availability cannot be ensured.



- 5 With an open innovation protocol, Deep Resolve is planned to facilitate translational research by enabling researchers to run their image reconstruction prototypes directly on the scanner.

Conclusion

Deep Resolve Gain and Deep Resolve Sharp introduce targeted, iterative denoising and deep learning reconstruction into clinical imaging. These technologies enable us to reduce acquisition times and improve image quality simultaneously. The unique inclusion of individual noise maps in an iterative reconstruction process enables intelligent, targeted denoising and Deep Resolve Sharp leverages the potential of deep learning reconstruction to achieve image resolutions beyond what is possible with conventional reconstruction methods. All this is done while including the acquired raw data along the entire reconstruction process, therefore ensuring robust and consistent results.

The potential of deep learning image reconstruction is immense, and current research is indicating a multitude of fascinating applications to come. Collaboration is key in MRI, so let us join our efforts in driving this exciting technology forward!

References

- 1 Pruessmann KP, Weiger M, Scheidegger MB, et al. SENSE: sensitivity encoding for fast MRI. *Magn Reson Med*. 1999;42(5):952-962.
- 2 Griswold MA, Jakob PM, Heidemann RM, et al. Generalized autocalibrating partially parallel acquisitions (GRAPPA). *Magn Reson Med*. 2002;47(6):1202-1210.
- 3 Lustig M, Donoho D, Pauly JM. Sparse MRI: The application of compressed sensing for rapid MR imaging. *Magn Reson Med*. 2007;58(6):1182-1195.
- 4 Hammernik K, Klatzer T, Kobler E, et al. Learning a variational network for reconstruction of accelerated MRI data. *Magn Reson Med*. 2018;79(6):3055-3071.
- 5 Hammernik, Kerstin, et al. Deep Learning for Parallel MRI Reconstruction. *MAGNETOM Flash* (75) 4/2019:10–15.
- 6 Kannengiesser SAR, Mailhe B, Nadar M, et al. Universal iterative denoising of complex-valued volumetric MR image data using supplementary information. *Proceedings of the ISMRM*, Abstract 1776, 2016.
- 7 Knoll F, Hammernik K, Zhang C, et al. Deep-learning methods for parallel magnetic resonance imaging reconstruction: A survey of the current approaches, trends, and issues. *IEEE Signal Processing Magazine* 37.1 (2020): 128–140.



Contact

Nicolas Behl, Ph.D.
Siemens Healthineers
DI MR M&S SYS
Erlangen
Germany
nicolas.behl@siemens-healthineers.com

The DICOM files of the figures in this article are available for download

www.magnetomworld.siemens-healthineers.com

> Clinical Corner > Protocols > DICOM Images



Phoenix is a unique syngo-tool that allows you to click on an image, drag it into the measurement queue, and instantly duplicate the extracted protocol – TR, TE, bandwidth, number of slices, echo spacing, etc.

- Phoenix ensures reproducibility, e.g., for patient follow-up.
- Phoenix shares optimized protocols on the different MAGNETOM systems you work with.
- Phoenix supports multi-center protocol standardization.

You'll find DICOM images from various systems and all aspects of MRI at magnetomworld.siemens-healthineers.com
> Clinical Corner > Protocols > DICOM Images

4D Flow Characteristics After Aortic Valve Neocuspidization in Pediatric Patients: a Comparison with the Ross Procedure

Paolo Ciancarella¹; Elena Milano^{2,3}; Matteo Trezzi⁴; Claudio Capelli²; Paolo Ciliberti⁴; Enrico Cetrano⁴; Davide Curione¹; Teresa Pia Santangelo¹; Carmela Napolitano¹; Veronica Bordonaro¹; Sonia B. Albanese⁴; Adriano Carotti⁴; Aurelio Secinaro¹

¹Department of Imaging, Advanced Cardiovascular Imaging Unit, Bambino Gesù Children's Hospital, IRCCS, Rome, Italy

²University College London, Institute of Cardiovascular Science, and Great Ormond Street Hospital for Children, London, United Kingdom

³Department of Surgery, Paediatrics and Obstetrics, University of Verona, Verona, Italy

⁴Department of Pediatric Cardiology and Cardiac Surgery, Bambino Gesù Children's Hospital, IRCCS, Rome, Italy

Introduction

The optimal management of aortic valve (AV) disease in children is still challenging. If AV replacement (AVR) is indicated, four main types of AV substitutes are generally considered: pulmonary autografts (i.e., the Ross procedure), mechanical valves, biological valve prostheses, or homografts [1]. Although each option has specific advantages and drawbacks [2], the Ross procedure, first reported in 1967 [3], currently represents the preferred choice in children¹ with severe AV dysfunction [4, 5]. However, concerns regarding autograft dilatation and durability of both autograft and pulmonary conduit are far from negligible, suggesting a growing need for development of alternative solutions [6]. In this context, there is a rising interest in AV neocuspidization (AV Neo) using the technique described by Ozaki [7], which showed satisfactory freedom from reoperation at follow-up in an adult population [8]. The use of the Ozaki technique in children, as an alternative to the Ross procedure, has shown promising results, but it is burdened by limited follow-up and hemodynamic profile data [9, 10].

Aortic blood flow visualization and quantification throughout the cardiac cycle have recently been studied by 4D flow cardiovascular magnetic resonance imaging (CMR) in both congenital and acquired heart disease, such as bicuspid AV (BAV) [11], ascending aorta (AAo) dilatation [12], and aortic coarctation [13]. Specifically, in AV disease, asymmetrical leaflet opening causes

abnormal rotational flow that hits the aortic wall [14] and is associated with increased wall shear stress and AAo diameters [11, 12].

In Ross patients, 4D flow CMR studies showed a laminar flow pattern in the AAo [15], comparable to a physiological hemodynamic profile. On the other hand, there is no data in the literature regarding AV Neo patients.



1 Aortic valve reconstruction with Ozaki procedure

The neo-cusps were reconstructed and then sutured to the annulus with the creation of three commissures, in line with the Ozaki neocuspidization technique.

¹MR scanning has not been established as safe for imaging fetuses and infants younger than two years of age. The responsible physician must evaluate the benefits of the MR examination compared to those of other imaging procedures.

We therefore aimed to study a population of patients undergoing either Ross or AV Neo surgery at our institution to compare the hemodynamic profile following the two procedures. The study was conducted using 4D flow CMR and the hemodynamic assessment included both aortic root and AAO analysis in all patients.

Methods

Study population

Twenty patients who underwent AV replacement at our institution were prospectively recruited for this study. The study population included a group of ten consecutive patients who underwent AV Neo (AV Neo group) and a group of ten Ross patients (Ross group), enrolled for a follow-up CMR study.

The study complied with the Declaration of Helsinki and was approved by the local ethics committee; written informed consent was obtained for all participants.

Surgical procedures

The Ross procedure was mainly performed in patients with AV stenosis, while the AV Neo procedure was performed regardless of the preponderant anatomic lesion. The Ross procedure was carried out by autograft transplantation of the native pulmonary root using a standard full root technique, with coronary reimplantation and allograft reconstruction of the right ventricular outflow tract.

The details of the surgical technique used for AV Neo have been previously reported [16]; briefly, the aortic cusps were independently reconstructed with pericardium and sutured to the aortic annulus, with the creation of three new commissures (Fig. 1). The rationale of this technique is to preserve the anatomy of the aortic root and the physiological response throughout the whole cardiac cycle, including the coordination between aortic valve, annulus, left ventricle, sinus of Valsalva, and aorta. Moreover, by creating a large coaptation area with the reconstructed pericardial leaflets, it also ensures valve competence during annular growth and avoids lifelong anticoagulation therapy.

CMR acquisition protocol

All patients included in this study were prospectively recruited for follow-up CMR performed on a 1.5T scanner (MAGNETOM Aera, Siemens Healthcare, Erlangen, Germany) with an 18-channel body coil. Image acquisition settings and protocols were uniform throughout the study. The CMR protocol included conventional, retrospectively ECG-gated breath-hold balanced steady-state free precession (bSSFP) cine sequences. These were acquired in standard cardiac planes (long-axis views and short-axis stack) to quantify left ventricular volumes and function,

and in dedicated AV and aortic root planes to evaluate leaflet excursion. Post-contrast ECG-gated 3D bSSFP magnetic resonance angiography (MRA) encompassing the whole thoracic aorta and triggered in mid-to-late diastole was obtained in the sagittal plane to measure aortic diameters.

A prototype 4D Flow gradient-echo sequence² (3D time-resolved phase-contrast imaging with three-directional velocity encoding) was acquired with retrospective ECG gating during free-breathing using a respiratory navigator placed at the lung-liver interface. The image acquisition volume was obtained in the sagittal plane encompassing the whole thoracic aorta. Technical parameters were as follows: isotropic voxel size ranging from 2.4 to 2.8 mm; field-of-view (FOV) read, 360–380 mm; FOV phase, 68.8–75%; matrix, 128 x 128 or 160 x 160; TR, 38 ms; TE, 2.3 ms; flip angle, 7°; receiver bandwidth, 496 Hz/pixel; parallel imaging (GRAPPA) along the phase encoding direction with a reduction factor $R = 2$ or 3. In order to optimize the velocity-to-noise ratio (VNR), the velocity encoding (VENC) range was determined using the lowest non-aliasing arterial velocity calculated on conventional 2D phase-contrast images. In our population, VENC values ranged between 180 and 400 cm/s depending on the presence and severity of valve acceleration. The sequence was acquired after intravenous contrast administration (gadoterate meglumine, DOTAREM, Roissy, Guerbet, France) at 0.2 mmol/kg, to improve image quality.

Image processing and analysis

Image processing and analysis was performed with a commercial software package (CMR42, Circle Cardiovascular Imaging Inc., Calgary, Canada). Left ventricular end-diastolic volume (LVEDV), end-systolic volume (LVESV), end-diastolic mass (LVEDM), and ejection fraction (LVEF) were calculated for each patient from short-axis cine bSSFP images. Papillary muscles and trabeculae were included in the blood pool. LVEDV, LVESV, and LVEDM were indexed for body surface area (BSA), calculated with the Mosteller formula.

Aortic measurements were obtained from 3D bSSFP MRA images; the diameter of the sinuses of Valsalva was the maximum value among the three sinus-to-sinus measurements, and the mid-AAo diameter was the maximum value between two orthogonal measurements in a cross-sectional plane at the level of pulmonary bifurcation. All the aortic measurements were taken from inner edge to inner edge of the vessel wall.

Pre-processing correction strategies were applied to all 4D Flow datasets in order to reduce phase offset errors and image noise. Moreover, data-quality evaluation was

²Work in progress: the application is currently under development and is not for sale in the U.S. and in other countries. Its future availability cannot be ensured.

performed to confirm measurement accuracy according to the literature [17], with quantitative comparison of 4D results and standard 2D phase-contrast sequences. 4D Flow datasets were processed to generate 3D interactive images of blood flowing through the thoracic aorta, visualized as Doppler-like color-coded streamlines and velocity vectors. After initial segmentation of the region of interest (from the left-ventricular outflow tract to the mid-descending aorta), the vessel centerline was automatically computed and manually adjusted when needed. Two reference planes perpendicular to the vessel centerline were identified at the sinotubular junction (P1) and at the point where the mid-AAo crosses the pulmonary bifurcation (P2). These landmarks were used to measure conventional flow and velocity parameters: forward flow (FF), backward flow (BF), net flow (NF), regurgitation fraction (RF), and maximum velocity (Vmax). The flow eccentricity index and wall shear stress were analyzed at the same levels. Blood flow eccentricity was evaluated on 2D color-coded velocity maps obtained in systole, and was semi-quantitatively graded by two operators (EM, PC) as central (grade 0), mildly eccentric (grade 1), or markedly eccentric (grade 2), in line with previous descriptions in the literature [18, 19] (Fig. 2). Wall shear stress (WSS, unit N/m^2) is a time-resolved 3D force obtained from

4D Flow datasets and calculated as axial, circumferential, and global components (Fig. 2). Both maximum and average WSS values were obtained.

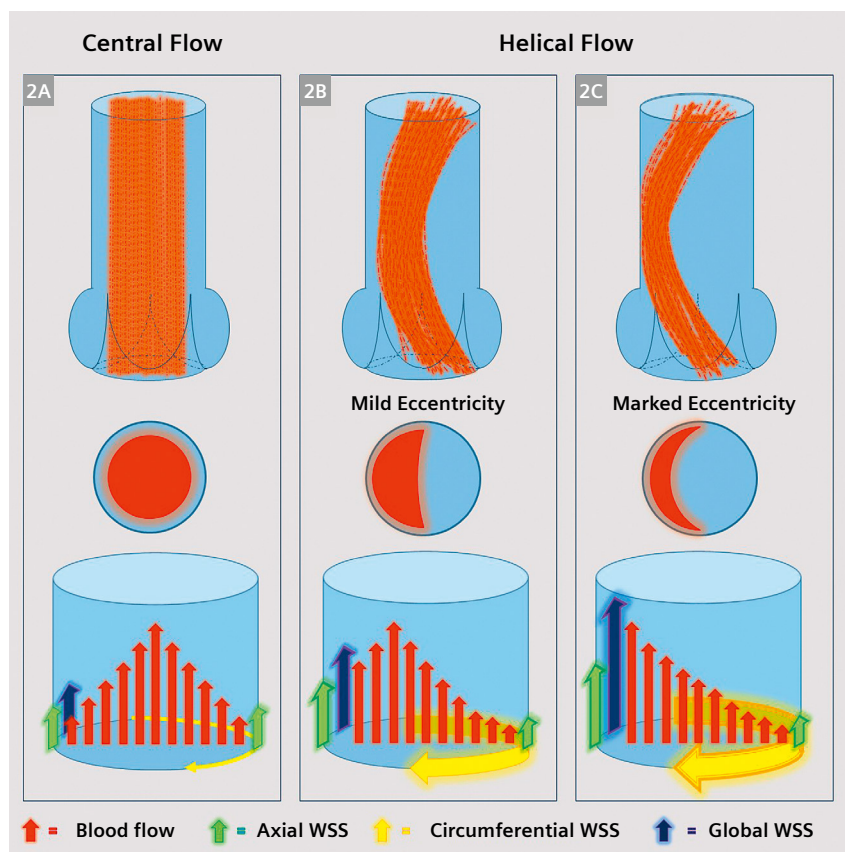
Statistical analysis

Data analysis was performed using MedCalc ver. 15.8 (MedCalc Software Ltd., Ostend, Belgium). For statistical analysis, the Wilcoxon signed-rank test, the Mann-Whitney U test and the ANOVA test were used. A p value ≤ 0.05 was considered to be significant. Values are presented as mean \pm standard deviation (SD) or as median and range, as appropriate.

Results

Aortic valvulopathy at the time of surgery was in most cases a congenital lesion, with BAV as the predominant diagnosis (65%). The baseline characteristics of patients are summarized in Table 1.

A data-quality check performed on phase-contrast datasets showed consistency of 4D Flow, with no significant discrepancies between 4D and 2D results. In addition, neither gross aliasing, nor aberrant streamlines/pathlines were visualized.



2 Wall shear stress in the ascending aorta

Different flow and wall shear stress patterns at the level of the ascending aorta: In central flow, high linear systolic flow is focused at the center and occupies the majority of the vessel lumen; axial WSS represents the main wall shear stress vector of global WSS (2A). In helical flow, the high systolic blood stream vectors are placed eccentrically toward the periphery of the vessel lumen and fill between one- and two-thirds of the vessel lumen (mild eccentricity, 2B) or one-third or less of the vessel lumen (marked eccentricity, 2C), with circumferential WSS representing the dominating vector of global WSS.

Ross procedure group

Median age at surgery was 10.6 years (range 3.9–16.5 years). Indications for the Ross procedure were aortic stenosis (n = 8), aortic regurgitation (n = 1), or mixed stenosis-regurgitation (n = 1). CMR imaging was performed at a median of 34 months after the operation (range 6–205 months). At follow-up, patients in the Ross group showed normal transvalvular max velocity (130 ± 33 cm/s) and peak gradient (7.0 ± 3.7 mmHg) across the aortic valve (Table 2), with mild regurgitation (RF $10.5 \pm 12.7\%$).

AV Neo group

Median age at surgery was 11.4 years (range 7.1–15.9 years). Indications for the AV Neo procedure were aortic regurgitation (n = 5), aortic stenosis (n = 4), or mixed stenosis-regurgitation (n = 1).

CMR imaging was performed at a median of 4 months after the operation (range 1–10 months). At follow-up, patients in the AV Neo group showed slightly increased maximum velocity across the aortic valve (220 ± 73 cm/s) with no significant regurgitation (RF $9.3 \pm 4.0\%$).

	Ross (n = 10)	AV Neo (n = 10)	p
Female (%)	1 (10%)	4 (40%)	0.12
Aortic valve defect (%)			
Bicuspid aortic valve	6 (60%)	7 (70%)	0.22
Aortic stenosis	8 (80%)	4 (40%)	0.07
Aortic regurgitation	1 (10%)	5 (50%)	0.05
Mixed stenosis/regurgitation	1 (10%)	1 (10%)	1
Age at surgery (years)	10.6 ± 4.2	11.4 ± 3.1	0.64
Age at scan (years)	16.2 ± 7.9	9.6 ± 2.9	*0.008
Surgery-to-scan time (months)	63.8 ± 64	4 ± 2.4	*0.0091
Body weight at scan (kg)	58.8 ± 17.8	47.5 ± 20.0	0.19
BSA at scan (m ²)	1.60 ± 0.33	1.36 ± 0.38	0.15
Aortic root indexed (mm/BSA)	24.2 ± 3.8	18.8 ± 5.6	*0.022
AAo indexed (mm/BSA)	17.0 ± 3.4	18.5 ± 5.0	0.45

Table 1: **Patient demographics**

Values expressed as average and standard deviation;

*statistically significant p values (p < 0.05)

	Ross (n = 10)	AV Neo (n = 10)	p
LVEDVi (ml/m ²)	91.2 ± 18.8	79.2 ± 14.4	0.12
LVESVi (ml/m ²)	37.6 ± 10.8	31.2 ± 13.4	0.19
LVEF (%)	59 ± 5	61.1 ± 7.2	0.46
CI (L/min/m ²)	3.47 ± 1.01	3.97 ± 1.04	0.29
LVEDMi (g/m ²)	64.7 ± 13.5	71.5 ± 11.1	0.23
Ao RF (%)	10.5 ± 12.7	9.3 ± 4.0	0.77
Ao Vmax (cm/sec)	130 ± 33	220 ± 73	*0.0024
Ao Gmax (mmHg)	7.1 ± 3.7	21 ± 13.8	*0.0065

Table 2: **Functional parameters**

Values expressed as average and standard deviation;

*statistically significant p values (p < 0.05).

Blood flow pattern and wall shear stress

Analysis of the flow pattern in patients who underwent either the Ross or the AV Neo procedure showed no clear association between an eccentric flow pattern and the operation performed ($p = 0.058$ at the sinotubular junction and $p = 0.17$ at the mid-AAo) (Figs. 3, 4).

At the sinotubular junction, Ross patients showed central flow in 40% of cases and mild eccentricity in 60% of cases, while AV Neo patients had central flow in 90% of cases and marked eccentricity in 10% of cases (inter-rater agreement Weighted K = 0.867). At the mid-AAo, Ross patients showed central flow in 30% of cases and mild eccentricity in 70% of cases, whereas AV Neo patients had central flow in 70% of cases, mild eccentricity in 20% of cases, and marked eccentricity in 10% of cases (inter-rater agreement Weighted K = 0.653). Figure 5 shows aortic fluid dynamics following AV Neo repair.

No significant differences between the two groups were observed in axial, circumferential, or global WSS

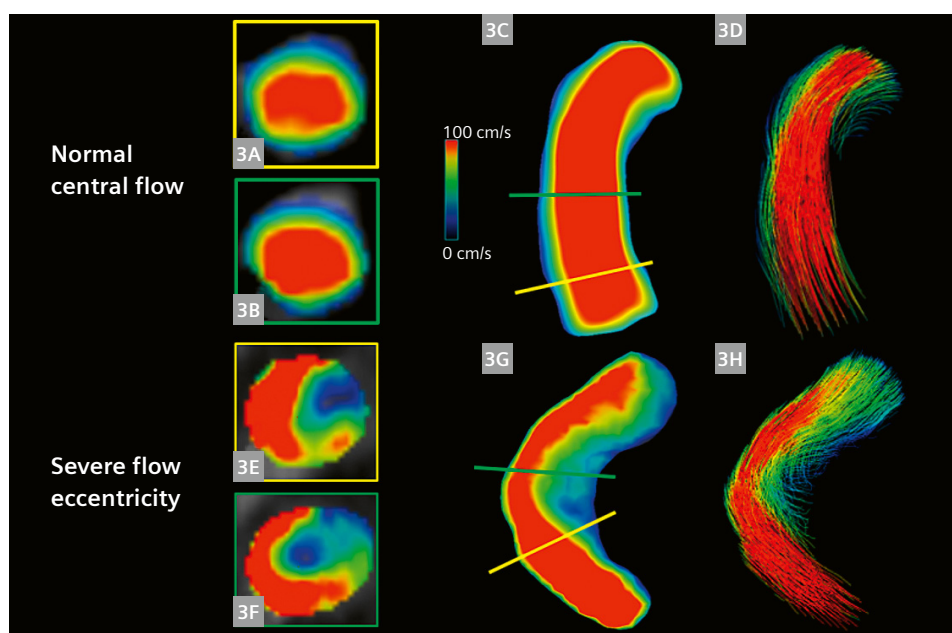
measured at the sinotubular junction and at the mid-AAo (Table 3).

Discussion

In this study, we demonstrated that the Ross procedure and the AV Neo procedure show similar hemodynamic profiles, analyzed by 4D Flow CMR.

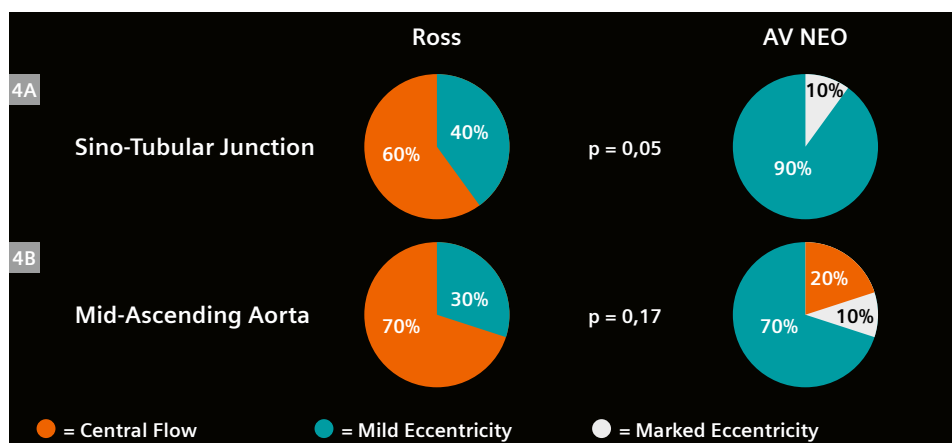
The influence of hemodynamic shear stress due to spatial and temporal alterations in shear forces on the endothelium has been described by others, showing regionally different flow and arterial remodeling [20]. The mechanical shear forces induced by blood flow seem to play an important role in the process of valve leaflet injury and vascular remodeling.

4D Flow CMR has been extensively applied in the *in vivo* investigation of many cardiovascular conditions [17], historically for research purposes [11, 13] and more recently as a viable clinical tool [17]. Although there is lack



3 Flow eccentricity

Evaluation of flow eccentricity: Upper panels (3A–3D) show an example of velocity maps of normal central flow at the level of the sinotubular junction (3A) and the mid-ascending aorta (3B); lower panels (3E–3H) show an example of velocity maps of a case with severe flow eccentricity at the level of the sinotubular junction (3E) and the mid-ascending aorta (3F).



4 Flow patterns after Ross and AV Neo procedures: Results of flow evaluation at the level of the sinotubular junction (4A) and the mid-ascending aorta (4B) are shown, with no statistically significant differences found between the two groups.

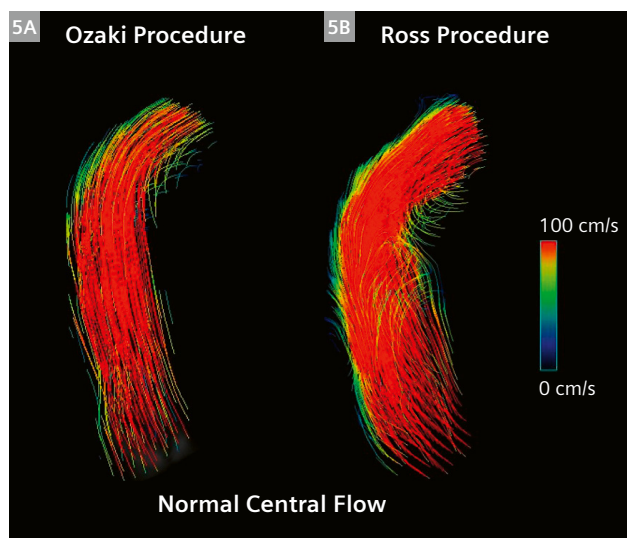
of standardization, especially in children, several reports have provided WSS reference values for the thoracic aorta [21, 22]. In addition, hemodynamic consequences of aortopathies have been well investigated, even in children [19, 23].

In the current study, we measured and calculated *in vivo* cardiodynamic data in patients who underwent either the Ross or the AV Neo procedure.

Firstly, we recognized that average Vmax values were higher in the AV Neo group than in the Ross group, which was probably related to the smaller indexed aortic root diameters of AV Neo patients. The presence of flow acceleration in the early postoperative period after AV Neo has been previously described [8]. Interestingly, mid-term follow-up confirms that the natural excursion and

“remodeling” of autologous cusps are distinctive features of the novel technique and that they can both contribute to a progressive and remarkable improvement of AV Neo hemodynamics compared to conventional AVR. Supporting this statement, blood flow distribution seemed to have a more prominent laminar flow at the sinotubular junction for AV Neo patients, with a p value close to statistical significance ($p = 0.058$).

Secondly, despite minor discrepancies among established determinants of theoretical WSS (velocity, vessel diameter, and flow eccentricity), both groups were comparable in terms of aortic WSS. In fact, no significant differences were observed in axial, circumferential, and global WSS measured at the sinotubular junction and at the mid-AAo. Although the main fluid-dynamic components differed between the two procedures when considered separately, overall WSS quantification by 4D Flow CMR showed similar hemodynamic performance. Notably, our results suggest that laminar flow and smaller vessel diameters probably balance the higher Vmax in the AV Neo group, while lower flow velocities seem to compensate for larger aortic roots and more prominent eccentric flow in the Ross group.



5 Comparison of ascending aortic 4D Flow profiles after the AV Neo procedure (5A) and the Ross procedure (5B): Despite evidence of minor flow turbulences, both the Ozaki and the Ross procedure are equally able to restore fluid-dynamic conditions very close to normal physiology.

Conclusion

Nowadays, 4D Flow CMR has become a valuable tool for investigating fluid-dynamics in congenital and acquired cardiovascular disease such as aortic valvular disorders, providing new advanced features to assess blood-flow characteristics and their effects on the vessel wall.

The AV Neo procedure shows similar hemodynamic results to the Ross procedure in the short-term. Although slightly higher flow velocities are found in the AAo after AV Neo, both procedures are equally able to restore physiological tri-leaflet fluid-dynamic conditions. The AV Neo procedure generates similar short-term hemodynamic results in children needing AVR. The long-term durability of the technique remains to be proven.

		Ross (n = 10)	AV Neo (n = 10)	p
Sinotubular junction	WSS global _{average} (N/m ²)	0.13 ± 0.05	0.16 ± 0.05	0.22
	WSS axial _{average} (N/m ²)	0.14 ± 0.04	0.14 ± 0.07	0.93
	WSS circ _{average} (N/m ²)	0.07 ± 0.03	0.07 ± 0.02	0.52
Mid-ascending aorta	WSS global _{average} (N/m ²)	0.13 ± 0.05	0.14 ± 0.04	0.92
	WSS axial _{average} (N/m ²)	0.13 ± 0.04	0.12 ± 0.02	0.36
	WSS circ _{average} (N/m ²)	0.08 ± 0.02	0.08 ± 0.03	0.74

Table 3: Wall shear stress (WSS) values according to the surgical procedure

Values expressed as average and standard deviation;

*statistically significant p values ($p < 0.05$).

Acknowledgments

We would like to thank the 4D Flow “work in progress” sequence developers Daniel Giese and Jin Ning from Siemens Healthineers. We are also very thankful to the entire group of CMR radiographers and nurses collaborating in the CMR.

References

- Akins CW, Miller DC, Turina MI, Kouchoukos NT, Blackstone EH, Grunkemeier GL, et al. Guidelines for reporting mortality and morbidity after cardiac valve interventions. *Ann Thorac Surg.* 2008;85(4):1490–1495.
- Sharabiani MTA, Dorobantu DM, Mahani AS, Turner M, Peter Tometzki AJ, Angelini GD, et al. Aortic Valve Replacement and the Ross Operation in Children and Young Adults. *J Am Coll Cardiol.* 2016;67(24):2858–2870.
- Ross DN. Replacement of aortic and mitral valves with a pulmonary autograft. *Lancet.* 1967;2(7523):956–958.
- Elkins RC, Thompson DM, Lane MM, Elkins CC, Peyton MD. Ross operation: 16-year experience. *J Thorac Cardiovasc Surg.* 2008;136(3):623–30, 630.e1–5.
- Takkenberg JJM, Kappetein AP, van Herwerden LA, Witsenburg M, van Osch-Gevers L, Bogers JJC. Pediatric autograft aortic root replacement: A prospective follow-up study. *Ann Thorac Surg.* 2005;80(5):1628–1633.
- Etnel JRG, Elmont LC, Ertekin E, Mokhles MM, Heuvelman HJ, Roos-Hesselink JW, et al. Outcome after aortic valve replacement in children: A systematic review and meta-analysis. *J Thorac Cardiovasc Surg.* 2016;151(1):143–152.e1–3.
- Ozaki S, Kawase I, Yamashita H, Uchida S, Nozawa Y, Matsuyama T, et al. Aortic valve reconstruction using self-developed aortic valve plasty system in aortic valve disease. *Interact Cardiovasc Thorac Surg.* 2011;12(4):550–553.
- Ozaki S, Kawase I, Yamashita H, Uchida S, Takatoh M, Kiyohara N. Midterm outcomes after aortic valve neocuspidization with glutaraldehyde-treated autologous pericardium. *J Thorac Cardiovasc Surg.* 2018;155(6):2379–2387.
- Wiggins LM, Mimic B, Issitt R, Ilic S, Bonello B, Marek J, et al. The utility of aortic valve leaflet reconstruction techniques in children and young adults. *J Thorac Cardiovasc Surg.* 2020;159(6):2369–2378.
- Baird CW, Sefton B, Chávez M, Sleeper LA, Marx GR, Nido PJ del. Congenital aortic and truncal valve reconstruction utilizing the Ozaki technique: Short-term clinical results. *J Thorac Cardiovasc Surg.* 2020;S0022-5223(20)30438-4.
- Bissell MM, Hess AT, Biasioli L, Glaze SJ, Loudon M, Pitcher A, et al. Aortic dilation in bicuspid aortic valve disease: Flow pattern is a major contributor and differs with valve fusion type. *Circ Cardiovasc Imaging.* 2013;6(4):499–507.
- Meierhofer C, Schneider EP, Lyko C, Hutter A, Martinoff S, Markl M, et al. Wall shear stress and flow patterns in the ascending aorta in patients with bicuspid aortic valves differ significantly from tricuspid aortic valves: a prospective study. *Eur Heart J Cardiovasc Imaging.* 2013;14(8):797–804.
- Kelm M, Goubergrits L, Fernandes JF, Biocca L, Pongiglione G, Muthurangu V, et al. MRI as a tool for non-invasive vascular profiling: A pilot study in patients with aortic coarctation. *Expert Rev Med Devices.* 2016;13(1):103–12.
- Guzzardi DG, Barker AJ, Ooij P Van, Malaisrie SC, Puthumana JJ, Belke DD, et al. Valve-Related Hemodynamics Mediate Human Bicuspid Aortopathy: Insights From Wall Shear Stress Mapping. *J Am Coll Cardiol.* 2015;66(8):892–900.
- Bissell MM, Loudon M, Hess AT, Stoll V, Orchard E, Neubauer S, et al. Differential flow improvements after valve replacements in bicuspid aortic valve disease: a cardiovascular magnetic resonance assessment. *J Cardiovasc Magn Reson.* 2018;20(1):10.
- Polito A, Albanese SB, Cetrano E, Cicienia M, Rinelli G, Adriano C. Aortic valve neocuspidization in paediatric patients with isolated aortic valve disease: early experience. *Interact Cardiovasc Thorac Surg.* 2021;32(1):111–117.
- Dyverfeldt P, Bissell M, Barker AJ, Bolger AF, Carlhäll C-J, Ebbers T, et al. 4D flow cardiovascular magnetic resonance consensus statement. *J Cardiovasc Magn Reson.* 2015;17(1):72.
- Hope MD, Hope TA, Crook SES, Ordozav KG, Urbania TH, Alley MT, et al. 4D flow CMR in assessment of valve-related ascending aortic disease. *JACC Cardiovasc. Imaging.* 2011;4(7):781–787.
- von Knobelsdorff-Brenkenhoff F, Trauzeddel RF, Barker AJ, Gruettner H, Markl M, Schulz-Menger J. Blood flow characteristics in the ascending aorta after aortic valve replacement – a pilot study using 4D-flow MRI. *Int J Cardiol.* 2014;170(3):426–433.
- Chivers SC, Pavy C, Vaja R, Quarto C, Ghez O, Daubeney PEF. The Ozaki Procedure With CardioCel Patch for Children and Young Adults With Aortic Valve Disease: Preliminary Experience – a Word of Caution. *World J Pediatr Congenit Heart Surg.* 2019;10(6):724–730.
- Davies PF. Hemodynamic shear stress and the endothelium in cardiovascular pathophysiology. *Nat. Clin. Pract. Cardiovasc Med.* 2009;6(1):16–26.
- Callaghan FM, Grieve SM. Normal patterns of thoracic aortic wall shear stress measured using four-dimensional flow MRI in a large population. *Am J Physiol Heart Circ Physiol.* 2018;315(5):H1174–H1181.
- Callaghan FM, Kozor R, Sherrah AG, Vallely M, Celermajer D, Figtree GA, et al. Use of multi-velocity encoding 4D flow MRI to improve quantification of flow patterns in the aorta. *J Magn Reson Imaging.* 2016;43(2):352–363.
- Rose MJ, Rigsby CK, Berhane H, Bollache E, Jarvis K, Barker AJ, et al. 4-D flow MRI aortic 3-D hemodynamics and wall shear stress remain stable over short-term follow-up in pediatric and young adult patients with bicuspid aortic valve. *Pediatr Radiol.* 2019;49(1):57–67.

Contact

Aurelio Secinaro, M.D.
Bambino Gesù Children's Hospital IRCCS
Department of Imaging
Piazza S. Onofrio 4,
00165 Rome
Italy
Phone: + 39 06 68592792
Fax: + 39 06 68592394
aurelio.secinaro@opbg.net



Aurelio Secinaro



Paolo Ciancarella

MRI Depicts Olfactory Bulbs and Cortical Involvement in COVID-19 Patients with Anosmia

Letterio S. Politi, M.D.^{1,2}; Marco Grimaldi, M.D.¹; Luca Balzarini, M.D.³

¹Department of Neuroradiology, IRCCS Humanitas Research Hospital, Rozzano, Milan, Italy

²Department of Biomedical Sciences, Humanitas University, Pieve Emanuele, Milan, Italy

³Department of Radiology, IRCCS Humanitas Research Hospital, Rozzano, Milan, Italy

Abstract

Anosmia and ageusia are very common symptoms in SARS-CoV-2 infections. Here we present magnetic resonance imaging evidence of brain signal alterations in the olfactory bulbs and the piriform cortex, presumably caused by SARS-CoV-2.

Key points

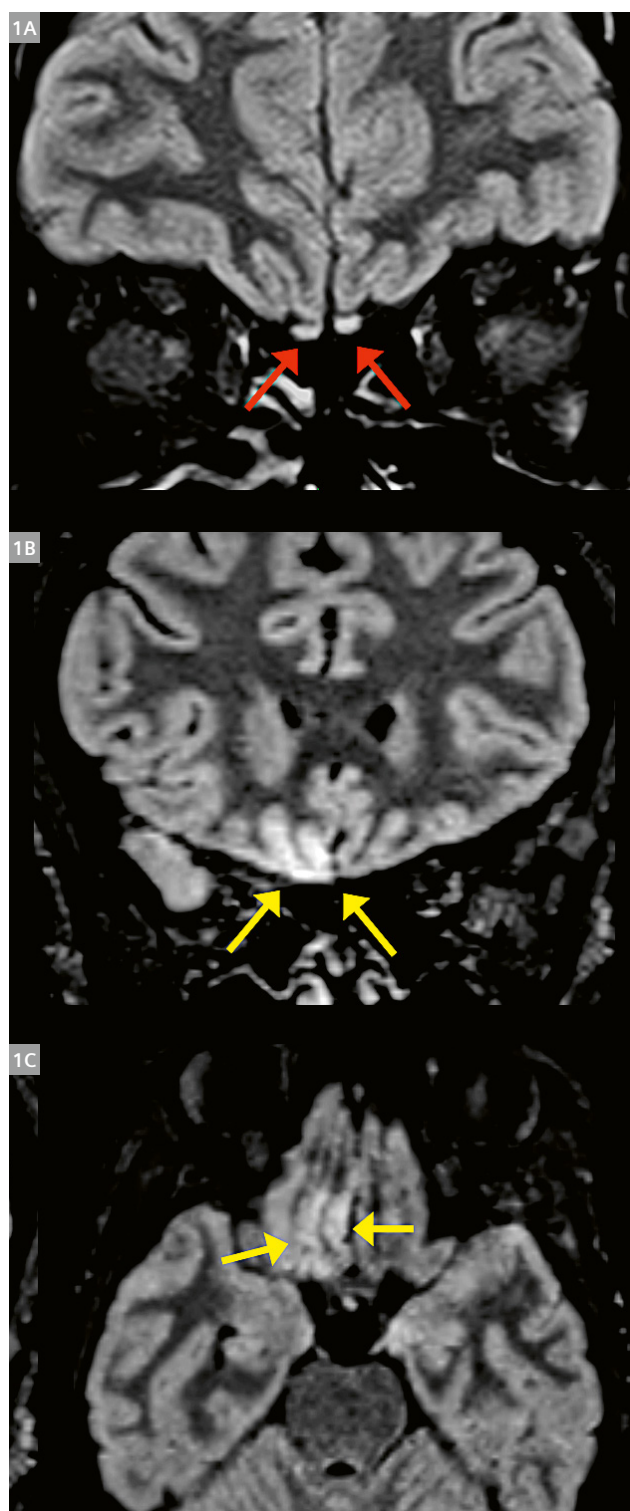
- In COVID-19 patients presenting with anosmia, T2-FLAIR hyperintensity can be depicted in the olfactory bulbs and anterior piriform cortex, suggesting possible viral invasion of the brain.
- The signal alteration is reduced when patients recover from the symptoms.
- Anosmia can be the predominant COVID-19 manifestation, and this should be taken into account when identifying and isolating infected patients in order to avoid disease spread.

The neurotropism of human coronaviruses has already been demonstrated in small animals [1]. In autaptic studies, the severe acute respiratory syndrome coronavirus (SARS-CoV), which was responsible for the SARS outbreak in 2002–2003, was found in the brain of infected patients [2]. It has been proposed that the neuroinvasive potential of the novel SARS-CoV-2 virus, which causes coronavirus disease 2019 (COVID-19), might be at least partially responsible for respiratory failure in COVID-19 patients [3]. In this paper, we will share magnetic resonance imaging (MRI) evidence of *in vivo* brain alteration presumably caused by SARS-CoV-2, and we will stress that anosmia can be the predominant symptom of COVID-19.

A 25-year-old female radiographer with no significant prior medical history who had been working in a COVID-19 ward presented with a mild dry cough that lasted for one day. This was followed by persistent and severe anosmia and ageusia. She was always nonfebrile. Three days later, a nasal fibroscopy was unremarkable, and non-contrast chest and maxillofacial computed tomography were negative. On the same day, a brain MRI was also performed,

using a 1.5 Tesla scanner (MAGNETOM Aera, Siemens Healthcare, Erlangen, Germany) equipped with a 20-channel phase array head and neck coil. On 2D and 3D fluid-attenuated inversion recovery (FLAIR) images, hyperintensity was evident in the bilateral olfactory bulbs (red arrows) and in the right rectus gyrus (yellow arrows). This signal alteration in the cortex of the brain area that is responsible for olfaction is highly suggestive of viral infection. Since many patients in the Italian outbreak complain of anosmia [4], a swab was performed and RT-PCR analysis was positive for COVID-19. In a follow-up MRI performed 28 days later, the signal alteration had almost completely disappeared and the patient had recovered from anosmia.

Similar but less-obvious MRI findings were depicted in a 39-year-old female COVID-19 patient who presented only with anosmia. In this case, the brain MRI was performed eight days after symptom onset. Furthermore, no brain abnormalities were seen in two other patients who presented with anosmia and underwent an MRI exam at 12 and 25 days from symptom onset, respectively.



1 Brain MRI alterations in a COVID-19 patient presenting with anosmia (three days after symptom onset). Coronal 2D FLAIR (1A, B) and axial reformatted 3D FLAIR images showing hyperintensity in bilateral olfactory bulbs (red arrows) and in the right gyrus rectus (yellow arrows).

Here we report on human brain involvement in patients who tested positive for COVID-19. We show signal alterations that are consistent with viral brain invasion in regions that are congruent with the patients' symptoms. It should be noted that the posterior part of the gyrus rectus and medial orbital gyrus encompasses the so-called anterior piriform cortex, which receives input from the olfactory bulb through the lateral olfactory tract. The anterior piriform cortex and the posterior piriform cortex (the latter is located in the temporal lobe) are considered the most important olfactory cortical areas. Curiously, in humans, the anterior piriform cortex seems to play a crucial role in encoding the difference between groups of odors. In anosmic animals like the dolphin, this entry zone is so undeveloped and flat that Broca called the area the "olfactory desert" (*désert olfactif*) [5].

Although the presence of SARS-CoV-2 in the cortical FLAIR hyperintense areas is not demonstrated by the MR images, we believe that the congruence between the clinical manifestations in our patient (i.e., olfactory dysfunction) and the cortical brain MRI abnormalities is highly suggestive of possible viral invasion; similar focal abnormalities are definitely unusual and alternative diagnoses are very difficult to find, especially in the clinical setting of anosmia (for instance, anti-NMDAR encephalitis can cause transient FLAIR hyperintensities, but the clinical manifestations rule out this entity; status epilepticus may cause transient gyral edema with T2-FLAIR hyperintensity, but olfactory aura continua / simple partial status epilepticus is exceptional, typically originates from the mesial temporal lobe, and causes olfactory hallucinations but not loss of smell). By contrast, viral infections are commonly considered potential causes of transient or permanent sensorineural olfactory dysfunctions. In the presented cases, no analysis of cerebrospinal fluid (CSF) was performed; however, it should be noted that the clinical sensitivity of CSF analysis with molecular testing for intraparenchymal brain diseases remains undefined (with the exception of herpes simplex (HSV) encephalitis), negative results may not exclude infection, and in some cases cerebral biopsy may be necessary to confirm the diagnosis. Overall, we believe that the abovementioned MRI findings support the hypothesis that the SARS-CoV-2 virus can invade the brain. Based on the MRI findings, our hypothesis is that, following initial replication in the nasal mucosa, SARS-CoV-2 may, as is the case with other coronaviruses, spread from the olfactory epithelium to the olfactory bulb, and subsequently to the posterior gyrus rectus through the lateral olfactory tract [1, 2].

Overall, the presence of MRI abnormalities in the posterior part of the gyrus rectus could conceivably be related to the centripetal spreading of SARS-CoV-2 through the lateral olfactory tract, and the olfactory dysfunction experienced by our patient may have a sensorineural

origin. Our own and others' observations of normal brain imaging in subjects with COVID-19-related olfactory dysfunctions [6], and the disappearance of the MRI abnormalities in a follow-up study in one of our patients suggest that these imaging changes might not always be present in COVID-19, or are limited to the very early phase of the infection. Further, anosmia can be the predominant COVID-19 manifestation, and this should be taken into account when identifying and isolating infected patients in order to avoid disease spread.

Acknowledgments

We are grateful to Simona Superbi for providing us with technical support.

References

- 1 Dubé M, Le Coupanec A, Wong AHM, Rini JM, Desforges M, Talbot PJ. Axonal Transport Enables Neuron-to-Neuron Propagation of Human Coronavirus OC43. *J Virol*. 2018;92(17):e00404–18.
- 2 Gu J, Gong E, Zhang B, Zheng J, Gao Z, Zhong Y, et al. Multiple organ infection and the pathogenesis of SARS. *J Exp Med*. 2005;202(3):415–24.
- 3 Li YC, Bai WZ, Hashikawa T. The neuroinvasive potential of SARS-CoV2 may play a role in the respiratory failure of COVID-19 patients. *J Med Virol*. 2020;92(6):552–555.
- 4 Giacomelli A, Pezzati L, Conti F, Bernacchia D, Siano M, Oreni L, et al. Self-reported Olfactory and Taste Disorders in Patients With Severe Acute Respiratory Coronavirus 2 Infection: A Cross-sectional Study. *Clin Infect Dis*. 2020;71(15):889–890.
- 5 Schiller F. A memoir of olfaction. *J Hist Neurosci*. 1997;6(2):133–46.
- 6 Eliezer M, Hautefort C, Hamel AL, Verillaud B, Herman P, Houdart E, et al. Sudden and Complete Olfactory Loss of Function as a Possible Symptom of COVID-19. *JAMA Otolaryngol Head Neck Surg*. 2020;146(7):674–675.



Luca Balzarini, M.D.



Marco Grimaldi, M.D.



Letterio S. Politi, M.D.

Contact

Letterio S. Politi, M.D.
Department of Neuroradiology
IRCCS Humanitas Research Hospital
Via Alessandro Manzoni 56,
Rozzano (MI), 20089
Italy
letterio.politi@hunimed.eu

Advertisement

View one of our most popular sessions from the 11th MAGNETOM World Summit: Quantitative, Robust Neuro MRI

Multi-parametric MRI in Stroke Imaging

Shan Shan Lu (First Affiliated Hospital of Nanjing Medical University, Nanjing, Jiangsu, China)

Clinical Benefits of MR Fingerprinting¹

Meiyun Wang (Henan People's Hospital, China)

MRI Techniques in Multiple Sclerosis:

New Diagnostic and Research Developments

Matilde Inglese (Università degli Studi di Genova, Italy)

Morphometry. Measuring Brain Maturation with Quantitative MRI

Baptiste Morel (Service de Radiologie Pédiatrique, Hôpital Clocheville, CHRU, Tours, France)

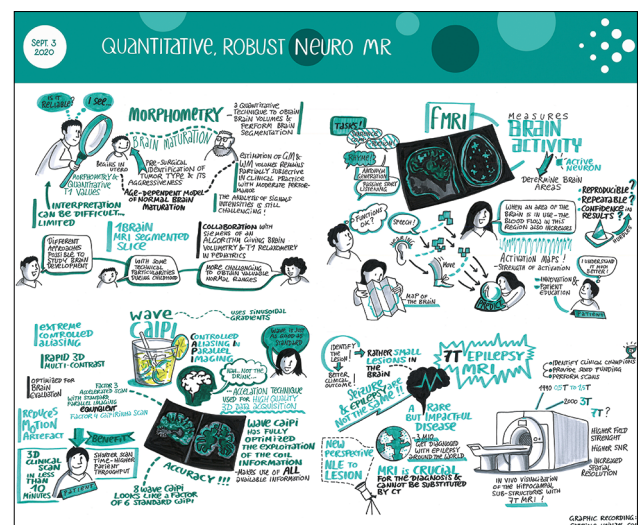
Wave CAIPI for Routine Clinical Brain MRI

Susie Huang (Massachusetts General Hospital, Boston, MA, USA)

Clinical Translation of 7T MRI: Epilepsy Imaging

Srinivasan Mukundan (Brigham and Women's Hospital, Boston, MA, USA)

[Siemens-Healthineers.com/MWS2020-recordings](https://www.siemens-healthineers.com/MWS2020-recordings)



Graphic recording: www.gabriele-heinzel.com

¹ MR Fingerprinting is not commercially available in some countries. Due to regulatory reasons its future availability cannot be ensured. Please contact your local Siemens Healthineers organization for further details.

Case Series: Clinical Application of Compressed Sensing Time-of-Flight MR Angiography

Luigi Cirillo^{1,3}; Gianfranco Vornetti¹; Caterina Tonon^{2,3}; Fiorina Bartiromo^{2,3}; Francesco Toni³; Tommaso Kaswalder³; Arianna Rustici¹; Raffaele Lodi^{2,3}

¹Department of Experimental, Diagnostic and Specialty Medicine, University of Bologna, Italy

²Department of Biomedical and Neuromotor Sciences, University of Bologna, Italy

³IRCCS Institute of Neurological Sciences of Bologna, Functional and Molecular Neuroimaging Unit, Bologna, Italy

Background

Cerebrovascular disease is a leading cause of morbidity and mortality worldwide and can arise from several intracranial vessel pathologies [1]. Time-of-flight MR angiography (TOF MRA) is a widely used technique for producing angiographic images. It is non-invasive, free from radiation exposure, and does not require contrast media [2]. Digital subtraction angiography (DSA) is the reference standard for evaluating cerebrovascular pathology, thanks to its high spatial and temporal resolutions. However, it is invasive, involves radiation exposure, and can cause possible adverse reactions to iodinated contrast material.

TOF MRA has therefore gained wide clinical acceptance as the preferred method of visualizing the cerebral vasculature. Several studies using DSA as reference showed that TOF MRA has high sensitivity and specificity for the detection of cerebrovascular pathologies, including cerebral aneurysms, arterio-venous shunts, and steno-occlusive disease [3, 4]. TOF MRA is also – especially when combined with other sequences – a reliable alternative to DSA in the follow-up of patients treated for cerebral aneurysm with either surgical or endovascular techniques, and those with arteriovenous malformations and fistulas [5–8].

However, TOF MRA is a time-consuming technique that reduces patient throughput and is susceptible to motion artifacts. This limits its applicability for uncooperative

patients. Parallel imaging (PI) is commonly used to reduce TOF MRA scan times, but acceleration factors rarely exceed 2 or 3, as further reduction of phase-encoding steps will rapidly increase noise and aliasing, resulting in typical scan times no shorter than 5 or 6 minutes [9].

Compressed sensing (CS) is a mathematical framework that reconstructs missing data from highly undersampled measurements. CS has been applied to MRI to achieve higher acceleration factors by incoherent *k*-space undersampling, through exploitation of the underlying sparsity in the appropriate transform domain [10–12]. TOF MRA is a good candidate for CS-based acceleration, as angiographic images feature sparse vessels with high signal over a well-suppressed background [13]. Recent studies have shown that CS TOF MRA¹ has comparable sensitivity and specificity to PI TOF MRA in the detection of various cerebrovascular pathologies, including aneurysms, stenosis, and arteriovenous shunts, while allowing a 2-to-3-fold reduction in scan time [14–18].

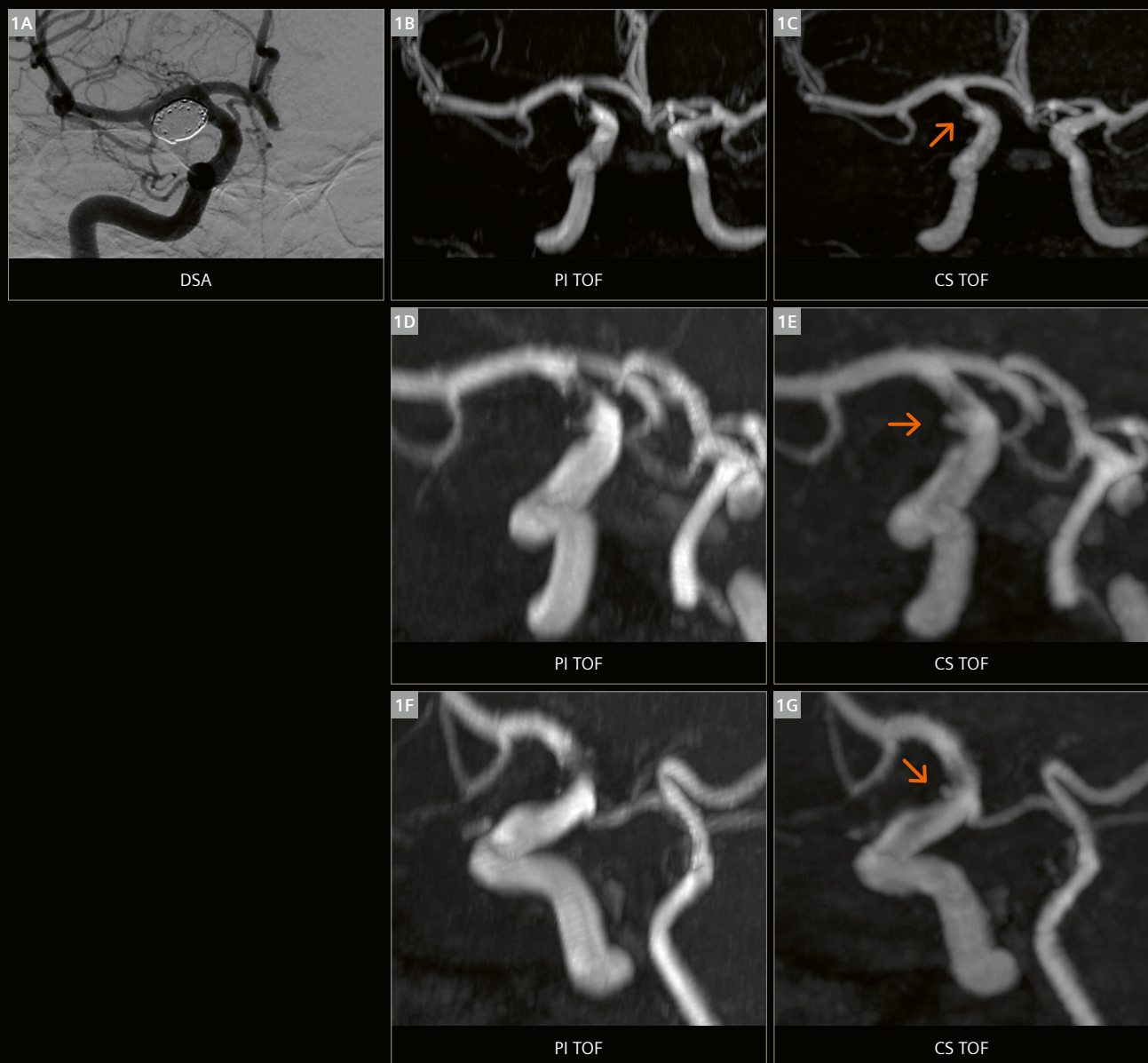
Here we show a comparison of PI and CS TOF MRA in the evaluation of patients with intracranial aneurysms, carotid artery stenosis, and arteriovenous malformation.

¹The product is still under development and not commercially available yet. Its future availability cannot be ensured.

Case 1

A 65-year-old female presenting with severe, sudden headache: Neuroimaging revealed a 9 mm unruptured aneurysm of the supraclinoid segment of the right internal carotid artery, which was treated with coil embolization. The day after the procedure, the patient underwent MRI that included MRA with both PI TOF (acquisition time:

7.5 minutes) and CS TOF sequences (acquisition time: 2.5 minutes). PI TOF MRA shows blurring at the interface between the coils and the parent vessel, which hinders the evaluation of coil protrusion. CS TOF MRA allowed clearer visualization of the parent vessel lumen, making it possible to identify a small neck remnant.

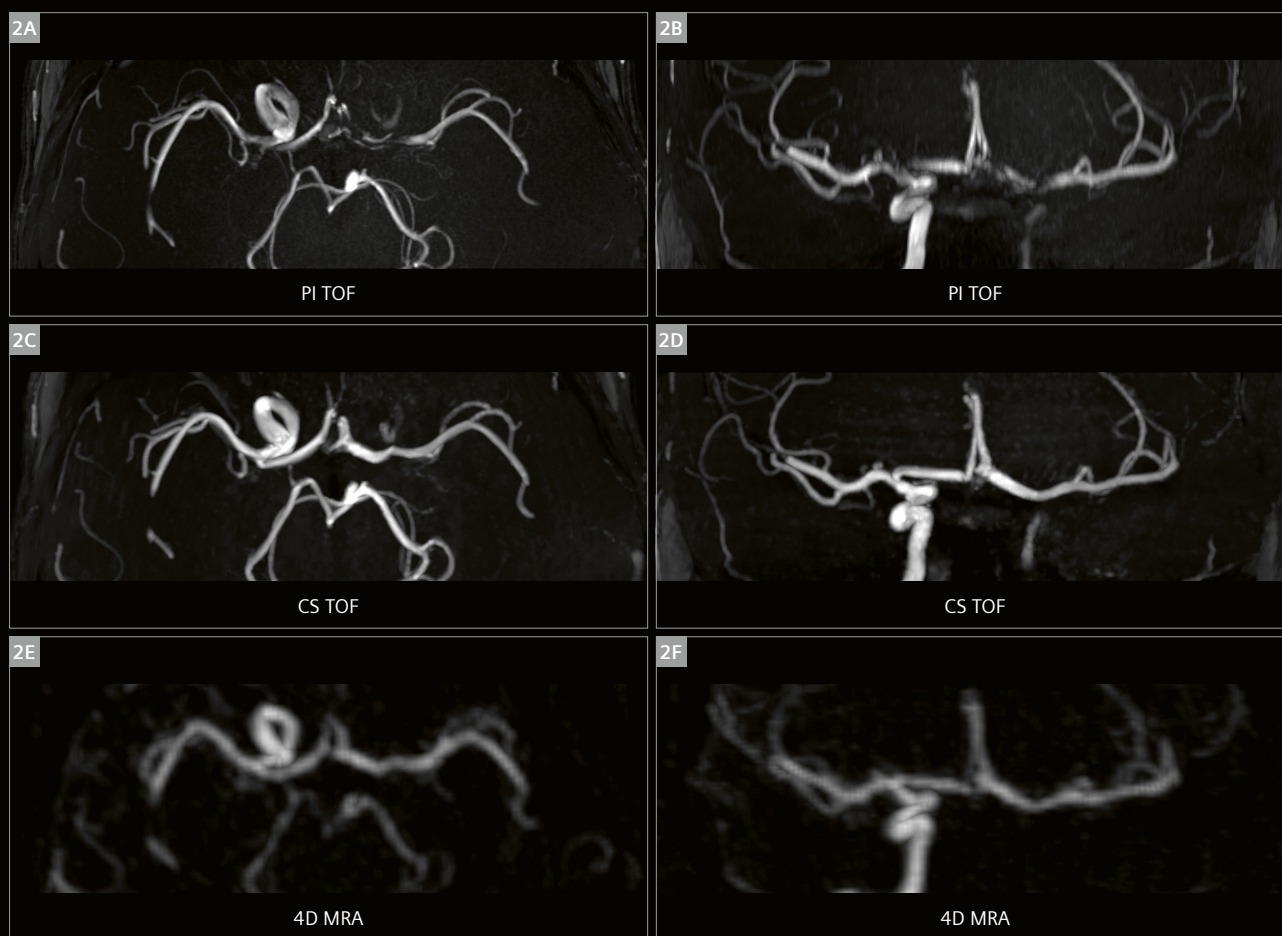


1 (1A) DSA with anterior-posterior view of the right internal carotid after aneurysm embolization. Coronal (1B, C), oblique coronal (1D, E), and oblique sagittal (1F, G) MIP images from PI TOF MRA (1B, D, F) and CS TOF MRA (1C, E, G). CS TOF MRA shows a clearer interface between the coils and the parent vessel, allowing the identification of a small neck remnant (orange arrows).

Case 2

A 42-year-old female with multiple intracranial aneurysms detected at neuroimaging screening for a family history of aneurysmal subarachnoid hemorrhage: A 4 mm aneurysm of the anterior communicating artery was treated with coil embolization, and two small wide-neck aneurysms of the supraclinoid segment of the left internal carotid artery were managed with flow-diverter placement. Follow-up imaging three years after the procedure revealed neointimal hyperplasia at the site of stent placement with marked

reduction of the vessel lumen. PI TOF MRA (acquisition time: 7.5 minutes) failed to clearly visualize the A1 segment of the left anterior cerebral artery, which might be due to turbulent flow caused by residual anterograde flow from the stenotic internal carotid artery and by retrograde flow from the anterior communicating artery. CS TOF MRA (acquisition time: 2.5 minutes) showed normal patency of the left A1 segment, which was confirmed by contrast-enhanced 4D MRA.

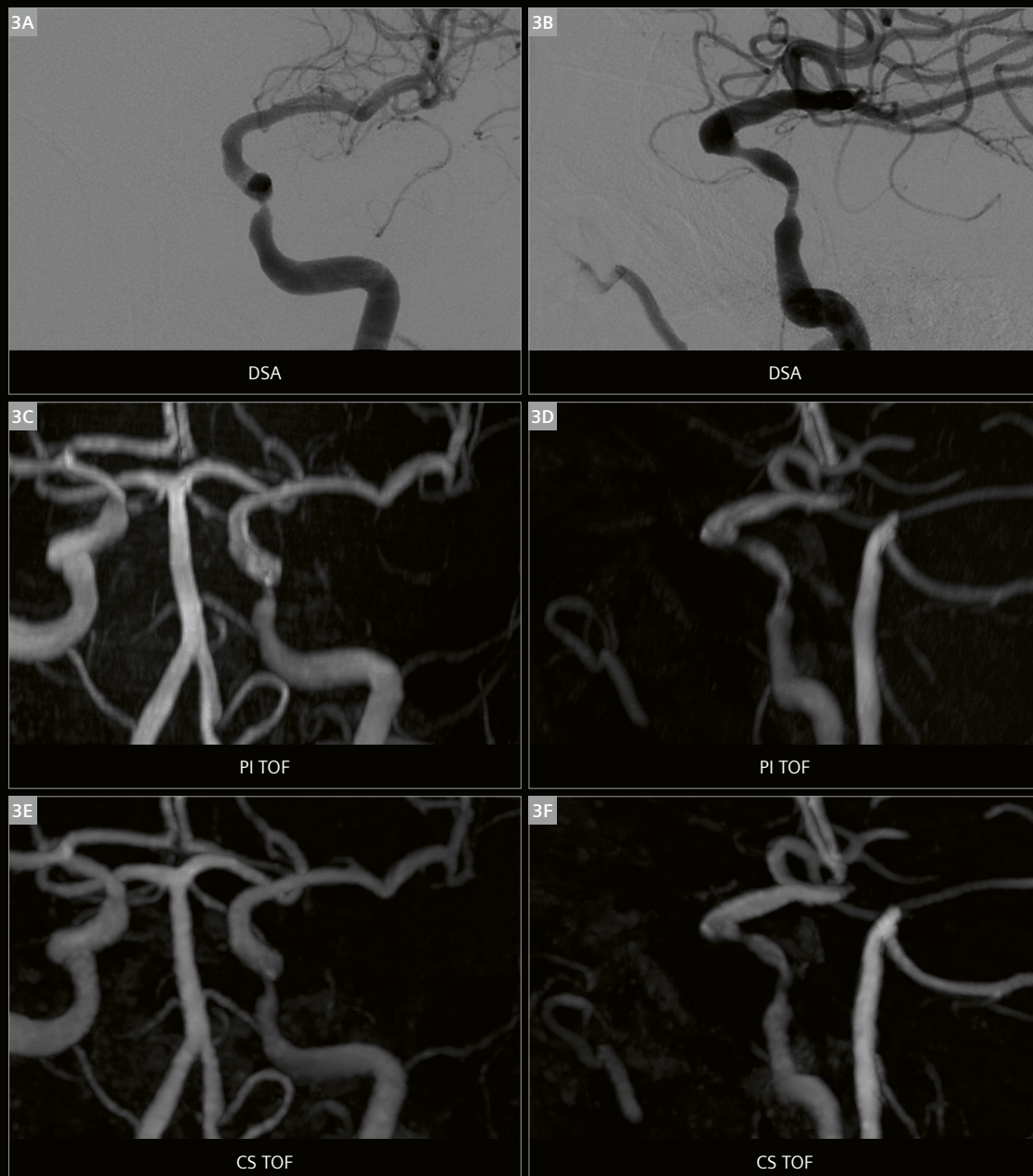


2 Axial (2A, C, E) and coronal (2B, D, F) MIP images from PI TOF MRA (2A, B), CS TOF MRA (2C, D), and arterial phase of contrast-enhanced 4D MRA (2E, F). CS TOF MRA shows normal patency of the left A1 segment, as detected by contrast-enhanced 4D MRA.

Case 3

A 71-year-old male presenting after spontaneous regression of right-sided motor impairment and aphasia: Neuroimaging revealed stenosis of the proximal and distal portion of the cavernous segment of the left internal carotid artery. Both PI and CS TOF MRA showed adequate

characterization of the stenosis when compared to angiographic images, but the latter showed higher signal homogeneity in the post-stenotic portion of the vessel, as well as sharper borders at the level of distal stenosis.

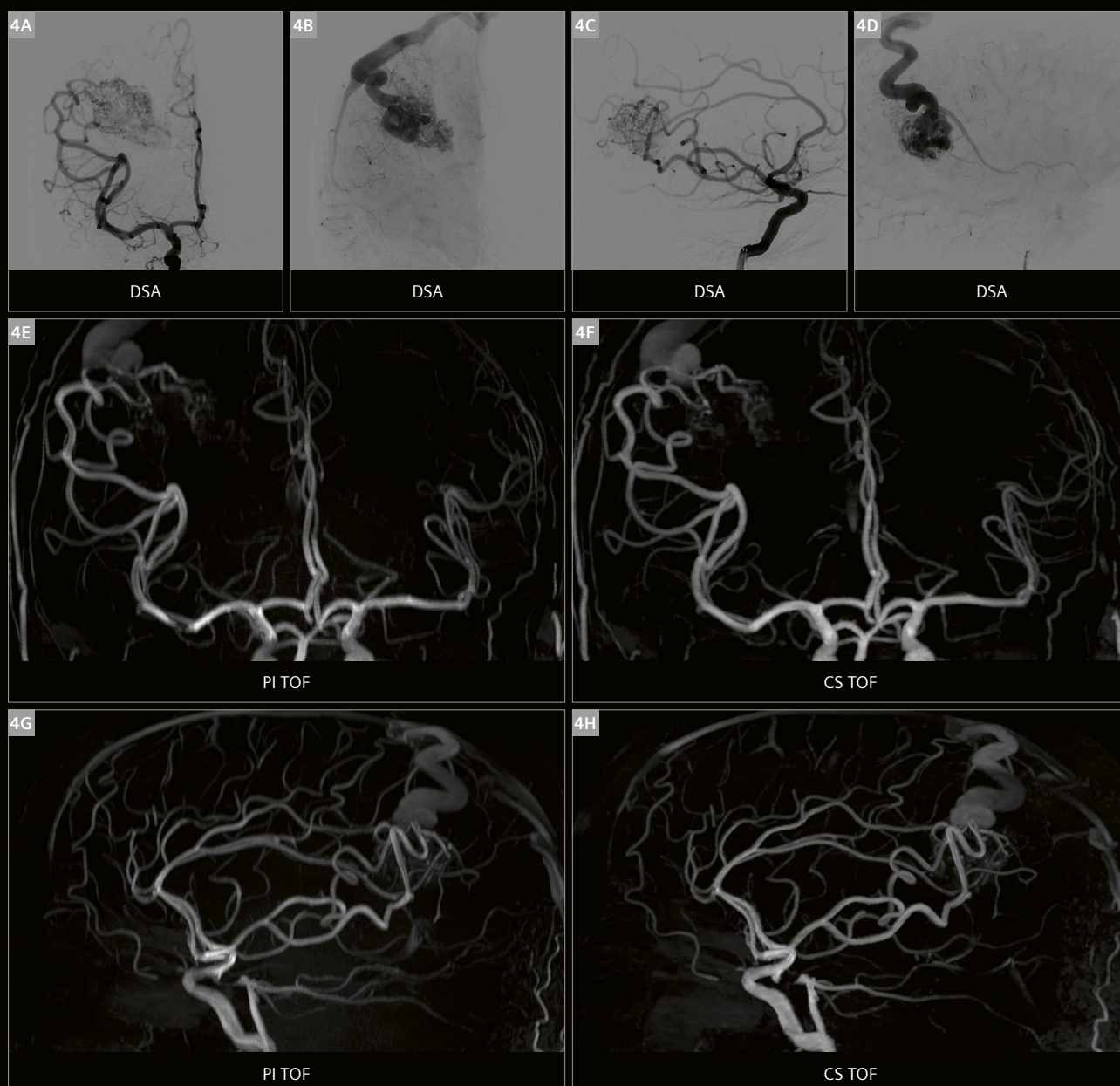


3 DSA with anterior-posterior (3A) and lateral (3B) views of the left internal carotid artery showing stenosis of the proximal and distal portion of the cavernous segment. Coronal (3C, E) and sagittal (3D, F) MIP images from PI TOF MRA (3C, D) and CS TOF MRA (3E, F) showing comparable characterization of the stenosis, although CS TOF MRA depicted higher signal homogeneity.

Case 4

A 38-year-old male presenting with simple partial seizure: Neuroimaging revealed a right parietal arteriovenous malformation with feeding pedicles originating from the right middle cerebral artery. The patient underwent partial embolization prior to radiosurgery. Post-embolization CS TOF MRA exhibited more homogeneous signal of afferent

vessels as well as higher signal at the level of the residual nidus compared to PI TOF MRA. The time advantage of CS acceleration was particularly relevant in this case, given the need to image a larger volume that would include the entire intracranial vasculature; scan time was reduced from 9.5 to 4 minutes.

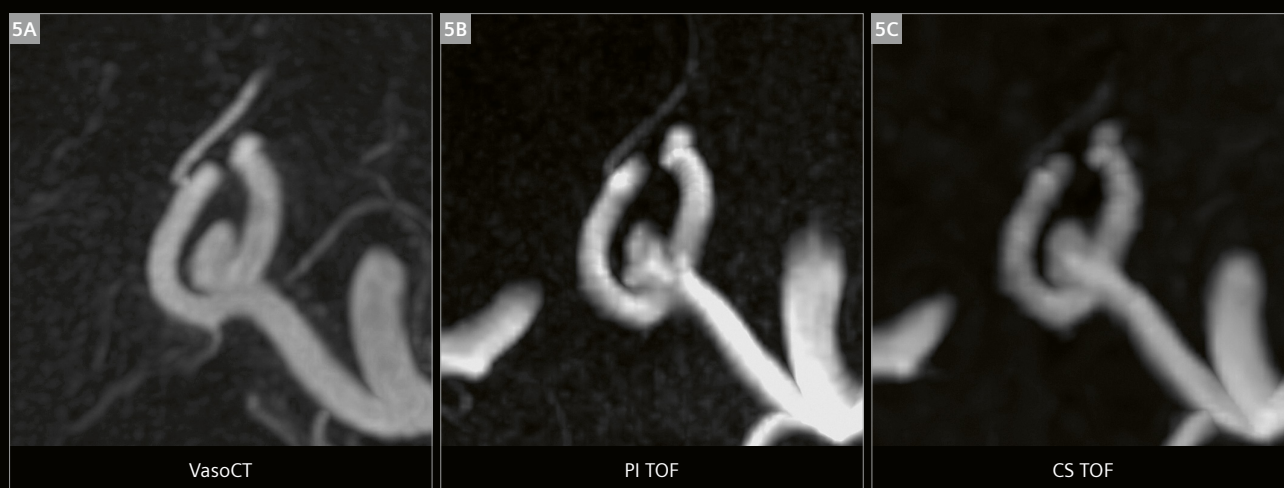


4 DSA with anterior-posterior (4A, B) and lateral (4C, D) views of the right internal carotid artery in arterial (4A, C) and capillary (4B, D) phases after partial embolization of the arterio-venous malformation. Coronal (4E, F) and sagittal (4G, H) MIP images from PI TOF MRA (4E, G) and CS TOF MRA (4F, H).

Case 5

A 65-year-old male with incidental finding of a small anterior communicating artery aneurysm, which was not treated due to the low risk of rupture: At follow-up imaging, PI TOF MRA (acquisition time: 7.5 minutes) showed an irregular morphology of the aneurysm, which

was not appreciated on CS TOF images (acquisition time: 2.5 minutes). The patient underwent further evaluation with VasoCT during DSA, which confirmed the regular shape of the aneurysm dome depicted by CS TOF MRA.



5 Axial oblique MIP images from VasoCT (**5A**), PI TOF MRA (**5B**), and CS TOF MRA (**5C**). CS TOF MRA shows a regular shape of the aneurysm dome, which is confirmed by VasoCT.

Technique

Imaging was performed on a 3T MR scanner (MAGNETOM Skyra, Siemens Healthcare, Erlangen, Germany) with a 64-channel head/neck coil. Parameters for the CS TOF MRA sequence were TR 21 ms, TE 3.49 ms, and a flip angle of 18°. In total, 4 slabs were acquired with 60 slices per slab and 20% slice oversampling, with a reconstructed voxel size of 0.4 x 0.4 x 0.4 mm³ and FOV of 22 cm. Parameters for the PI TOF MRA sequence were TR 23 ms, TE 3.98 ms and a flip angle of 18°. In total, 4 slabs were acquired with 36 slices per slab and 22% slice oversampling, with a reconstructed voxel size of 0.4 x 0.4 x 0.7 mm³.

Due to the computationally intensive nature of CS acceleration, we found it useful to acquire CS TOF MRA as one of the first sequences to allow reconstruction time before the end of the examination. It is still possible to continue to acquire other sequences during reconstruction.

Conclusions

CS TOF MRA scans with submillimeter resolution can be accelerated by a factor of ten, enabling scan times of only two minutes while maintaining diagnostic image quality. Short scan times reduce the risk of motion artifacts, allowing examination of uncooperative patients, and increase patient comfort, which is particularly relevant for those needing frequent follow-up scans.

After an initial stage when both PI and CS TOF MRA sequences were acquired to assess diagnostic accuracy and gain confidence with this new technique, we began routinely using CS TOF MRA to evaluate different cerebrovascular pathologies. As well as the advantage of short acquisition times, we also observed an increase in signal homogeneity in intracranial vessels with turbulent flow, and a reduction in device-related artifacts.

References

- 1 Mozaffarian D, Benjamin EJ, Go AS, Arnett DK, Blaha MJ, Cushman M, et al. Heart Disease and Stroke Statistics – 2016 Update. *Circulation*. 2016;133(4):e38–360. Available at: <https://www.ahajournals.org/doi/10.1161/CIR.0000000000000350>.
- 2 Carr JC, Carroll TJ (eds). *Magnetic Resonance Angiography* [book on the Internet]. New York, NY: Springer New York; 2012. Available from: <http://link.springer.com/10.1007/978-1-4419-1686-0>.
- 3 Sailer AM, Wagemans BA, Nelemans PJ, de Graaf R, van Zwam WH. Diagnosing intracranial aneurysms with MR angiography: systematic review and meta-analysis. *Stroke*. 2014;45:119–126.
- 4 Li MH, Li YD, Tan HQ, Gu BX, Chen YC, Wang W, et al. Contrast-free MRA at 3.0 T for the detection of intracranial aneurysms. *Neurology*. 2011;77(7):667–676.
- 5 van Amerongen MJ, Boogaarts HD, de Vries J, Verbeek AL, Meijer FJ, Prokop M, et al. MRA versus DSA for follow-up of coiled intracranial aneurysms: A meta-analysis. *AJNR Am J Neuroradiol*. 2014;35(9):1655–1661.
- 6 Ahmed SU, Mocco J, Zhang X, Kelly M, Doshi A, Nael K, et al. MRA versus DSA for the follow-up imaging of intracranial aneurysms treated using endovascular techniques: A meta-analysis. *J Neurointerv Surg*. 2019;11(10):1009–1014.
- 7 Leclerc X, Guillaud O, Reyns N, Hodel J, Outteryck O, Bala F, et al. Follow-Up MRI for Small Brain AVMs Treated by Radiosurgery: Is Gadolinium Really Necessary? *AJNR Am J Neuroradiol*. 2020;41(3):437–445.
- 8 Hu YS, Guo WY, Lin CJ, Wu HM, Luo CB, Wu CA, et al. Magnetic resonance imaging as a single diagnostic tool for verifying radiosurgery outcomes of cavernous sinus dural arteriovenous fistula. *Eur J Radiol*. 2020;125:108866. Available at: <https://doi.org/10.1016/j.ejrad.2020.108866>.
- 9 Griswold MA, Jakob PM, Heidemann RM, Nittka M, Jellus V, Wang J, et al. Generalized autocalibrating partially parallel acquisitions (GRAPPA). *Magn Reson Med*. 2002;47(6):1202–1210.
- 10 Forman C, Wetzl J, Hayes C, Schmidt M. Compressed Sensing: a Paradigm Shift in MRI. *MAGNETOM Flash*. 2016;66(3):8–13. Available at: <https://www.magnetomworld.siemens-healthineers.com/hot-topics/compressed-sensing?stc=wwhim800017>
- 11 Ye JC. Compressed sensing MRI: a review from signal processing perspective. *BMC Biomed Eng*. 2019;1:1–17.
- 12 Geethanath S, Reddy R, Konar AS, Imam S, Sundaresan R, Ramesh Babu DR, et al. Compressed sensing MRI: a review. *Crit Rev Biomed Eng*. 2013;41(3):183–204.
- 13 Yamamoto T, Okada T, Fujimoto K, Fushimi Y, Yamamoto A, Togashi K. Compressed Sensing: Application to Time-of-Flight MR Angiography. *MAGNETOM Flash* 2016;66(3):36–39. Available at: [http://file://localhost\(null\)%0Apapers3://publication/uuid/CCEA2692-EA37-4073-AC67-D10ACDB5D765](http://file://localhost(null)%0Apapers3://publication/uuid/CCEA2692-EA37-4073-AC67-D10ACDB5D765).
- 14 Fushimi Y, Okada T, Kikuchi T, Yamamoto A, Okada T, Yamamoto T, et al. Clinical evaluation of time-of-flight MR angiography with sparse undersampling and iterative reconstruction for cerebral aneurysms. *NMR Biomed*. 2017;30(11):1–9.
- 15 Sakata A, Fushimi Y, Okada T, Nakajima S, Hinoda T, Speier P, et al. Evaluation of cerebral arteriovenous shunts: a comparison of parallel imaging time-of-flight magnetic resonance angiography (TOF-MRA) and compressed sensing TOF-MRA to digital subtraction angiography. *Neuroradiology*. 2020. doi: 10.1007/s00234-020-02581-y. Epub ahead of print.
- 16 Demerath T, Bonati L, Mekabaty A El, Schubert T. High-resolution compressed-sensing time-of-flight MRA in a case of acute ICA/MCA dissection. *Neuroradiology*. 2020;62(6):753–756.
- 17 Yamamoto T, Okada T, Fushimi Y, Yamamoto A, Fujimoto K, Okuchi S, et al. Magnetic resonance angiography with compressed sensing: An evaluation of moyamoya disease. *PLoS One*. 2018;13(1):e0189493.
- 18 Zhang X, Cao YZ, Mu XH, Sun Y, Schmidt M, Forman C, et al. Highly accelerated compressed sensing time-of-flight magnetic resonance angiography may be reliable for diagnosing head and neck arterial steno-occlusive disease: a comparative study with digital subtraction angiography. *Eur Radiol*. 2020;30(6):3059–3065.

Contact

Luigi Cirillo
Associate Professor of Neuroradiology
Alma Mater Studiorum – University of Bologna
IRCCS Istituto delle Scienze Neurologiche
di Bologna
Via Altura 3
40133 Bologna
Italy
luigi.cirillo2@unibo.it



Iterative Denoising Applied to 3D SPACE CAIPIRINHA: An Application to Musculoskeletal Imaging

Sana Rebbah, Ph.D.¹; Chadi Hlailhel, M.D.²; Yves Le Rumeur, M.D.²; Stephan Kannengiesser, Ph.D.³; Alto Stemmer³; Thomas Troalen, Ph.D.¹

¹Siemens Healthcare SAS, Saint-Denis, France

²Groupe du Mail, Grenoble, France

³Siemens Healthineers, Erlangen, Germany

Abstract

The purpose of this study was to evaluate the performance of 3D SPACE with CAIPIRINHA acceleration combined with a prototype iterative denoising (ID) algorithm¹ in musculoskeletal imaging at 1.5T, and to qualitatively compare image quality between the conventional sequence and the iteratively denoised sequence.

This prospective study involved a total of 23 patients who underwent a 1.5T knee or ankle MRI. Standard SPACE and SPACE with ID reconstruction were acquired. Two reviewers assessed sequence performance (resolution, signal/noise, contrast, edge sharpness) and clinical criteria (cartilage defect, meniscus, bone marrow edema, ligament) based on a 5-point scale. Qualitative scores were statistically analyzed using Wilcoxon rank tests, and the interobserver reliability was evaluated using Cohen's kappa coefficient.

SPACE with ID demonstrated better image quality than the standard SPACE sequence for all evaluated items (median = 4; $p < 0.05$) apart from signal/noise (median = 3; $p > 0.05$). Once the utilization of ID in MSK was validated in a patient cohort, a second evaluation step focused on contrast-optimized sequences with ID reconstruction in patients. We show that signal and contrast could both be improved in comparison to the standard SPACE sequence and reconstruction.

Introduction

Magnetic resonance imaging (MRI) has been established as a very reliable modality for the evaluation of the musculoskeletal (MSK) system, including the knee and the ankle joints. The standard protocol for MSK MRI usually comprises fat-saturated proton density (PD) or T2-weighted 2D turbo-spin-echo (2D TSE) sequences in three planes and one sagittal T1-weighted TSE sequence. Indeed, an accurate visualization of the cartilage, bone damage, and joint effusion is usually obtained using this contrast combination. The main indications are diverse and depend on the studied joints. These sequences offer excellent image quality and are routinely used. However, due to partial volume effects occurring in the usual slice thickness of ≥ 3 mm at 1.5T and the limited possibilities of postprocessing with 2D sequences, the detection of small lesions and small structures remains difficult with 2D sequences [1].

3D TSE sequences allow covering a whole volume of interest with an isotropic resolution and reduced partial volume effects [2]. 3D TSE sequences have been used in MSK imaging, particularly of the spine, knee, and ankle [3, 4]. The commercially available SPACE sequence, a 3D TSE sequence, uses extended echo trains with flip-angle modulation allowing very high turbo factors and a scan time that is compatible with clinical routine. The SPACE sequence with CAIPIRINHA (controlled aliasing in parallel imaging results in higher acceleration), a parallel imaging technique [5, 6], has been proven to be an advantageous combination in MSK and brain imaging, as an improvement in spatial resolution and a reduction of the acquisi-

¹Work in progress: the application is currently under development and is not for sale in the U.S. and in other countries. Its future availability cannot be ensured.

tion time were observed [7]. More recently, the combination of SPACE readout with a prototype iterative denoising (ID) algorithm [8] has been highly encouraging for neurological disease exploration, as shown in previous work by Vaussy et al. [9].

To our knowledge, the ID algorithm has not yet been evaluated in combination with SPACE readout in MSK imaging. In this work, we first seek to provide clinical cases and evidence of the added value of ID in MSK imaging. We then present some contrast-optimized SPACE protocols that are enabled by the time saved using an improved image reconstruction algorithm compared to standard parallel imaging.

Validation of iterative denoising applied to the SPACE CAIPIRINHA sequence in MSK imaging

Materials and methods

Study information

This prospective study was carried out from October 2020 to December 2020 at Groupe du Mail, Grenoble, France. A total of 23 patients (13 female and 10 male) aged 40 ± 14 [15–63] years (mean \pm SD [range]) were enrolled for this first study. Knee MR examinations were conducted on 15 patients (laterality: 9 left and 6 right), and ankle MR examinations were performed on 8 patients (laterality: 2 left and 6 right). The main reason for the MR exams was pain in the knee or in the ankle area. Severe motion artifacts in 3D sequences were the exclusion criteria for this population. The images were independently reviewed and evaluated by two musculoskeletal radiologists with over 10 years of experience.

MRI technique

All MR examinations were acquired on a 1.5T MRI system (MAGNETOM Aera, Siemens Healthcare, Erlangen, Germany) using a Tx/Rx 15-channel coil for knee examinations and a 16-channel receive-only coil for ankle examinations.

The patients underwent both the conventional SPACE sequence with CAIPIRINHA acceleration (a commercially available sequence), and a SPACE CAIPIRINHA with prototype¹ iterative denoising [8]. The image contrast studied was proton density with SPAIR fat saturation (PD FS).

Different sequence optimization strategies were implemented depending on the anatomical region:

For knee examinations, the aim was to improve spatial resolution while keeping scan time constant at 4 minutes. Therefore, a 3D sagittal SPACE sequence with an interpolated $(0.36 \text{ mm})^3$ isotropic resolution was acquired with a field of view of $187 \times 165 \text{ mm}^2$, a parallel imaging accel-

eration factor of 2×2 (3D CAIPIRINHA), weak SPAIR mode, a turbo factor of 35, and TE/TR of 75 ms/1000 ms, combined with ID reconstruction and 85% denoising strength.

For ankle examinations, the aim was to adapt the original 0.7 mm^3 protocol to reduce scan time. Therefore, a 3D sagittal SPACE sequence with a $(0.7 \text{ mm})^3$ isotropic resolution (interpolated to $0.37 \times 0.37 \times 0.7 \text{ mm}^3$) was acquired with a field of view of $190 \times 190 \text{ mm}^2$, a parallel imaging acceleration factor of 3×2 (3D CAIPIRINHA), and TE/TR of 77 ms/800 ms, combined with ID reconstruction and 85% denoising strength.

Spatial resolution and scan time of the standard and ID sequences are reported in Table 1 for the different applications. For more information about the sequence parameters, please contact the corresponding authors.

		Spatial resolution (mm ³)	CAIPIRINHA acceleration factor	Scan time
Knee	Reference 3D SPACE PD FS	$0.8 \times 0.8 \times 0.8$	2×2	4:00
	High-resolution 3D SPACE PD FS + ID	$0.36 \times 0.36 \times 0.36i$	2×2	4:10
Ankle	Reference 3D SPACE PD FS	$0.7 \times 0.7 \times 0.7$	2×2	4:50
	Accelerated 3D SPACE PD FS + ID	$0.37 \times 0.37 \times 0.7i$	3×2	3:25

Table 1: Principal sequence parameters of the 3D SPACE CAIP sequences (with and without iterative denoising, ID).

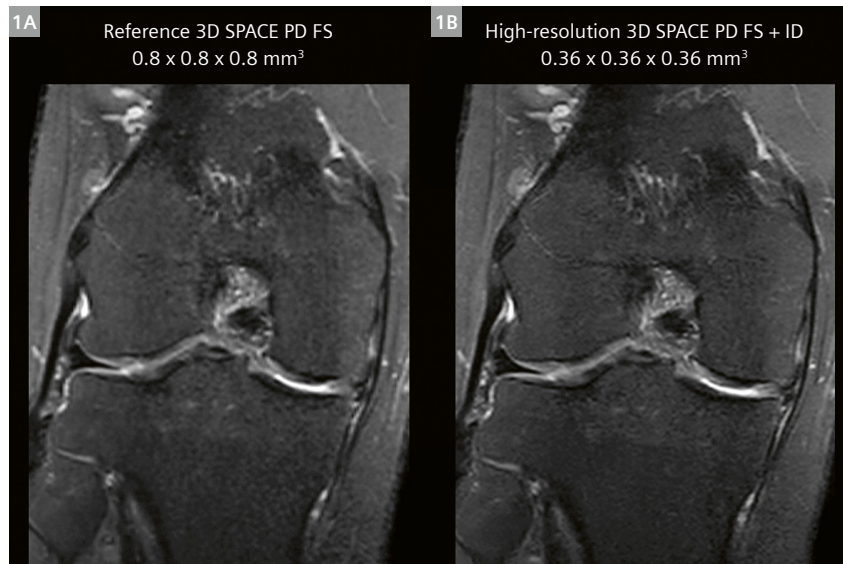
Qualitative assessment

The standard images and the optimized SPACE CAIPIRINHA with ID reconstruction were compared side-by-side for each patient by two reviewers.

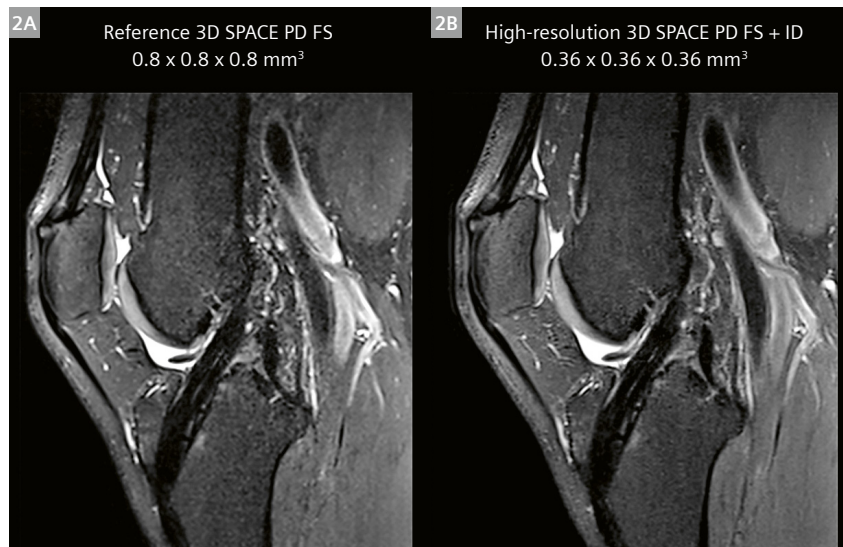
Images were rated by evaluating eight qualitative criteria: four imaging scores (resolution, signal/noise, contrast, and edge sharpness) and four clinical scores (chondropathy, meniscus, bone marrow edema, ligament) that evaluate the capacity of the new sequence to visualize the latter aspects. Scores were based on a scale of 1 to 5 (1 = markedly worse; 2 = worse; 3 = equivalent; 4 = better; 5 = markedly better).

Statistical analysis

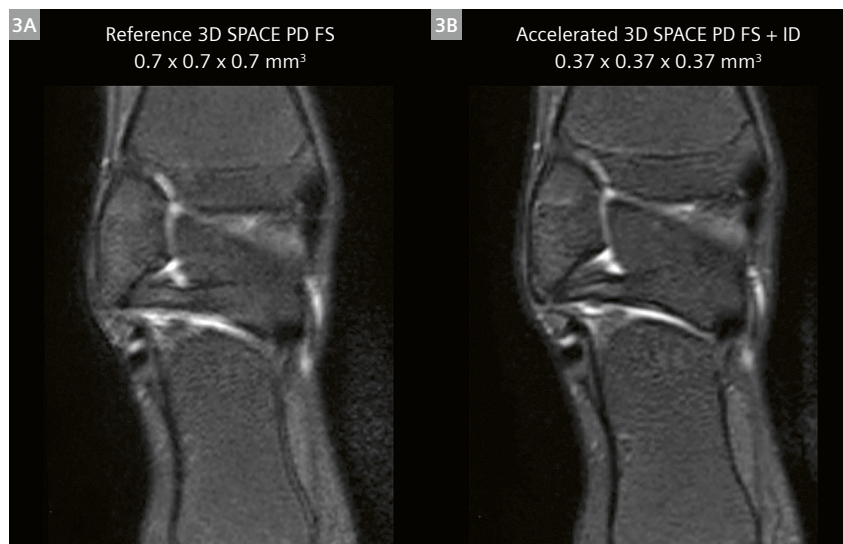
Statistical analyses were performed using the commercially available software R, version 3.6.2 (The R Foundation, Vienna, Austria) [10]. The statistical analyses for the quality scores were performed using Wilcoxon rank tests



- 1** 59-year-old male with a medial meniscal tear, coronal reformat of 3D SPACE PD FS image with ID (**1B**) shows a better outline of the meniscus and the medial femoral condyle abnormalities than the reference 3D SPACE (**1A**).



- 2** 40-year-old male with a history of anterior cruciate ligament reconstruction, native sagittal 3D SPACE PD FS image with ID (**2B**) shows a significantly better signal-to-noise ratio in the intercondylar notch and the distal femur compared to the standard 3D SPACE (**2A**).



- 3** 15-year-old female with ankle pain, coronal reconstruction of 3D SPACE PD FS image with ID (**3B**) shows a significantly better signal-to-noise ratio and improved visualization of the calcaneo-fibular and posterior talo-fibular ligaments compared to the standard 3D SPACE (**3A**), with a scan time reduction of almost 30%.

(one-sided, null hypothesis $H_0: m \leq m_0$ with $m_0 = 3$, which represents the “equivalent” quality score). P-values < 0.05 ($\alpha = 5\%$) were considered as statistically significant and were Bonferroni-corrected for multiple comparisons. The inter-rater agreement for the qualitative scores was assessed using the weighted Cohen’s kappa coefficient with 0–0.20 = slight agreement; 0.21–0.40 = fair agreement; 0.41–0.60 = moderate agreement; 0.61–0.80 = substantial agreement; 0.81–1.0 = almost perfect agreement [11].

Results

Image-quality assessment

Our results demonstrate that it was possible to achieve high-quality (0.36 mm)³ isotropic 3D SPACE PD FS images in a clinically acceptable imaging time of 4 minutes for knee imaging at 1.5T. Figures 1 and 2 present two clinical cases.

While we aimed to improve spatial resolution for knee imaging, our focus for ankle imaging was on optimizing the acquisition time. A 30% reduction in scan time was feasible while maintaining high image quality and radiological confidence, as depicted in the clinical example in Figure 3.

Quality scores and statistical analysis

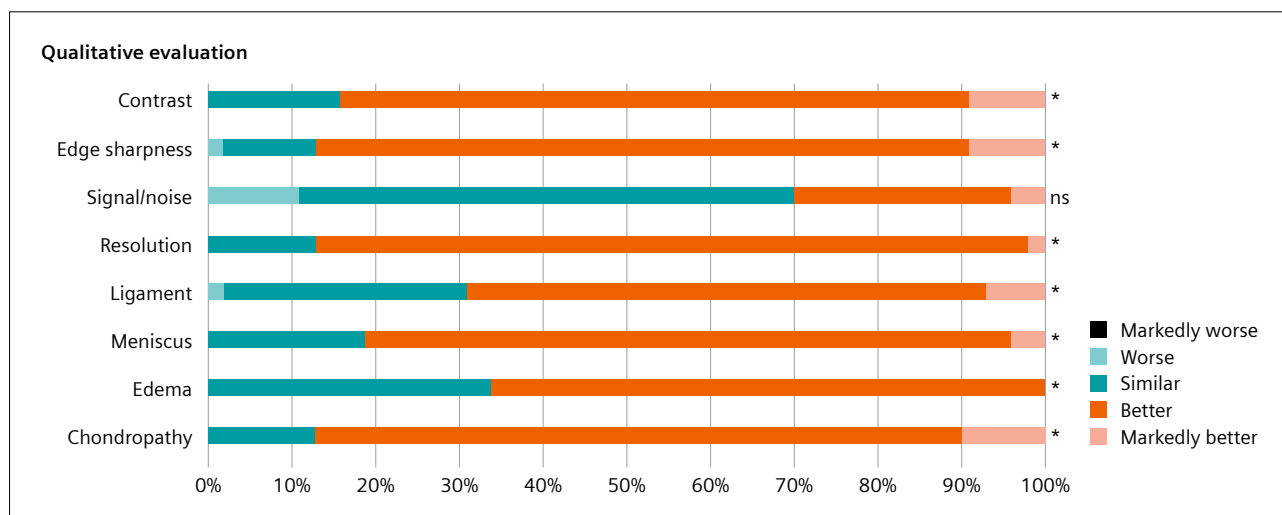
The quality scores for the high-resolution or accelerated SPACE CAIPIRINHA combined with ID reconstruction were significantly higher than those for the standard SPACE CAIPIRINHA reconstructions without ID. This was true for almost all the quality scores: resolution (median = 4; range = 3 to 5; p-value < 0.001), contrast (median = 4; range = 3 to 5; p-value < 0.001), edge sharpness (median = 4; range = 3 to 5; p-value < 0.001), edge sharpness (median = 4; range = 2 to 5; p-value < 0.001), chondropathy

(median = 4; range = 3 to 5; p-value < 0.01), bone marrow edema (median = 4; range = 3 to 4; p-value < 0.05), meniscus (median = 4; range = 3 to 5; p-value < 0.05), ligament (median = 4; range = 2 to 5; p-value < 0.01). Only the signal/noise score was not significantly improved (median = 3; range = 2 to 5; p-value > 0.05). We also noted that neither of the two radiologists ever rated the ID images as being “markedly worse” (score of 1) than the original images. Relative score distributions are displayed in Figure 4.

The average kappa coefficient is 0.55 ($p < 0.05$) between the two reviewers for all evaluated items, which indicates moderate agreement between the two radiologists. Substantial agreement was observed for the bone marrow edema, ligament, and chondropathy quality scores ($\kappa = 0.75, 0.8$, and 0.6 respectively; p-value < 0.05) and fair agreement was seen for the meniscus and edge sharpness scores ($\kappa = 0.35$ and 0.3 respectively).

Discussion

This study shows that ID reconstruction, when compared to conventional parallel imaging reconstruction and applied to the 3D SPACE sequence in MSK, achieves an overall improvement in image quality. The sole exception is the signal/noise criterion, which seems to be equivalent for the new and the standard reconstructions, although the spatial resolution or the acquisition time were improved. This can be explained by the fact that the denoising strength was deliberately set at 85% to avoid a synthetic or blurred appearance in the final reconstructed images. Furthermore, in MSK imaging the endpoints of MR examinations are the visualization and radiological confidence of the clinical findings (chondropathy, meniscus, ligament,



4 Results of the two radiologists’ ratings based on the comparison of images from the standard and the new sequences (the scores were combined into relative distributions, as a percentage of the total number of cases). Quality scores for the new images with iterative denoising were significantly higher than the original images without ID (* $p < 0.05$, Wilcoxon rank tests) for all the qualitative criteria except signal/noise (ns = non-significant, $p > 0.05$).

or edema). The SPACE sequence with ID reconstruction was shown to be superior in all of these clinical aspects, with an improved visualization of the clinical criteria. However, one bias of the present study is that the prototype sequence was always acquired at the end of the exam in order to ensure reliable clinical findings. This might have introduced more variations into the measured metrics, especially signal stability over the successive long SPACE readouts with respect to motion. Figure 5 shows an example in which the ID reconstruction was rated worse than the standard one.

We have demonstrated that improvement of the spatial resolution or reduction of the acquisition time, which undeniably reduces the inherent signal-to-noise ratio, were feasible without visual signal loss using this denoising approach. Therefore, this version of SPACE ID with higher spatial resolution or reduced acquisition time allowed us to address the most important clinical evaluation criteria in MSK imaging while keeping the high signal-to-noise ratio needed for clinical decision-making.

This first cohort study was necessary to validate the ID reconstruction while maintaining clinical confidence. The following part now focuses on improving contrast and signal quality while maintaining the clinical benefits obtained in the first study.

Using iterative denoising to improve image contrast: An MSK imaging case report

Population and MRI technique

A total of 6 patients (4 female and 2 male) aged 43 ± 17 [24–71] years (mean \pm SD [range]) were enrolled for this second study. Half of the patients underwent knee MR examinations (laterality: 2 left and 1 right) and half underwent ankle MR examinations (laterality: 2 left and

1 right). The same two radiologists reviewed and evaluated the images.

All MR examinations were acquired on the same scanner and using the same coils as the first study. The patients underwent both the conventional sequence and a contrast-

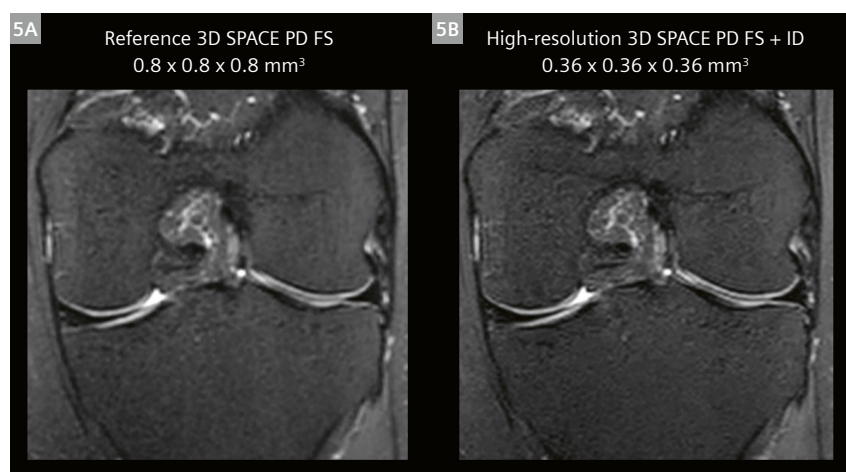
		Spatial resolution (mm ³)	CAIPIRINHA acceleration factor	Scan time
Knee	Optimized 3D SPACE PD FS + ID	0.36 x 0.36 x 0.36i	2 x 2	3:58
Ankle	Optimized 3D SPACE PD FS + ID	0.37 x 0.37 x 0.37i	3 x 2	3:53

Table 2: Principal sequence parameters of the contrast-optimized 3D SPACE CAIPIRINHA ID sequences.

optimized SPACE CAIPIRINHA with ID reconstruction. Again, the contrast was proton density with SPAIR fat saturation (PD FS). For this second study, some parameters were finely tuned to improve image contrast and signal-to-noise ratio:

For knee imaging the SPACE variable flip angle mode was set to Constant (FA 120°) instead of PDVar, a strong SPAIR FS mode was selected, and a denoising strength of 95% was carefully chosen to accommodate signal loss using strong SPAIR fat saturation.

For ankle imaging the acceleration factor and spatial resolution were kept constant with a final reconstructed isotropic voxel size of (0.37 mm)³. TE/TR was increased from 77 ms/800 ms to 100 ms/1000 ms, TF was increased from 33 to 44 using T2Var instead of PDVar, and a partial signal average of 1.4 instead of 1 was used. SPAIR mode was also set to Strong, and the denoising strength was slightly increased from 85% to 90% to improve the final image appearance and the signal-to-noise ratio.

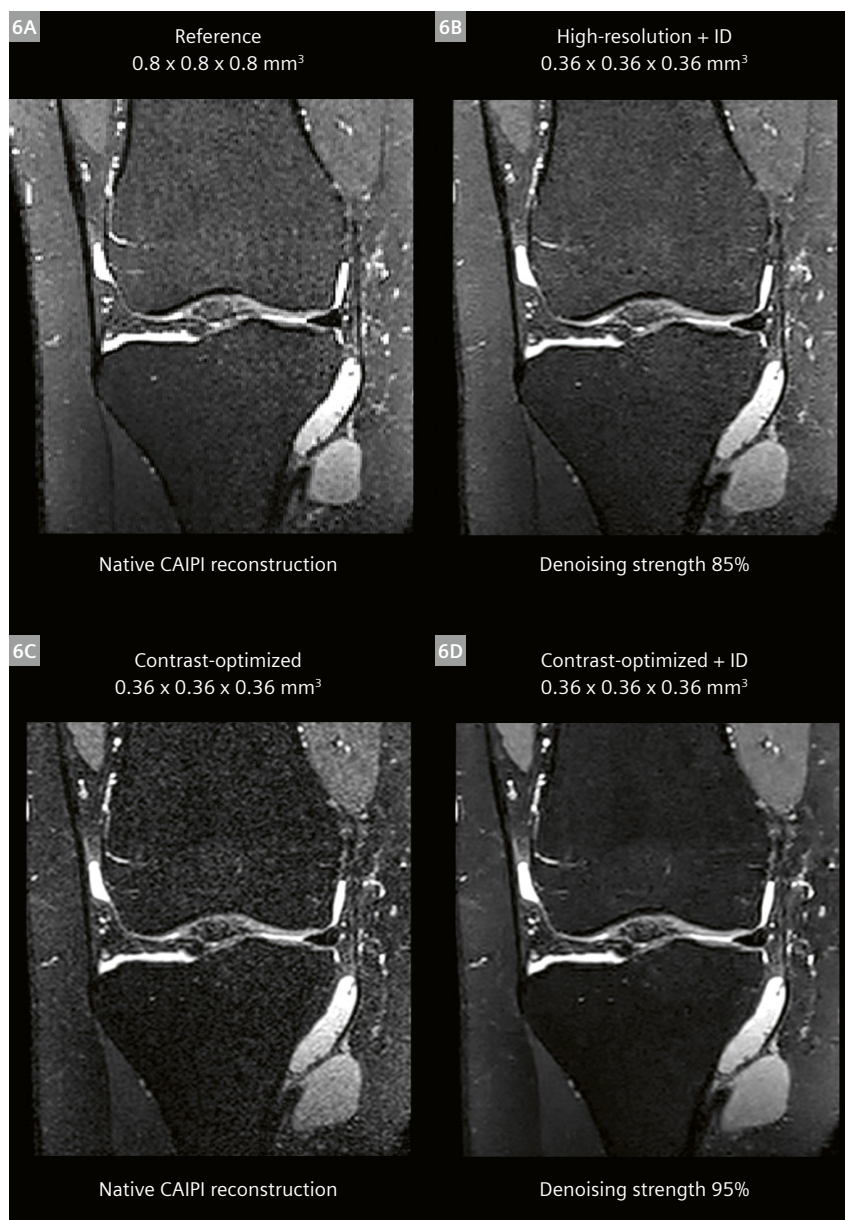


5 26-year-old male referred for a lateral knee pain. Coronal 3D SPACE PD FS image with ID (**5B**) shows a reduced signal-to-noise ratio and signal ripples at the interfaces within the medial femoral cartilage in comparison to the product SPACE reference (**5A**); this could be attributed to excessive motion during the scan.

Results and discussion

The contrast-optimized SPACE ID sequence allowed us to obtain higher image quality than the standard SPACE sequence without ID for all the quality scores: resolution (median = 4; range = 3 to 5), contrast (median = 4; range = 3 to 5), edge sharpness (median = 4; range = 3 to 5), chondropathy (median = 4; range = 4 to 5), bone marrow edema (median = 4; range = 3 to 5), meniscus (median = 4; range = 4 to 4), ligament (median = 4; range = 3 to 5), and signal/noise (median = 4; range = 3 to 5). We also noticed that none of the quality scores were lower than 3, meaning that all of the new images acquired with the contrast-optimized SPACE ID sequence were at least equivalent to the images from the standard SPACE sequence.

A comparison of the three knee protocols proposed in this article is presented in Figure 6. While the parameter changes for the first study (6A and B) could accommodate a denoising strength of only 85%, by using strong SPAIR fat sat and a constant flip angle readout to improve the contrast, one can easily see that the resulting image using default reconstruction was too noisy for proper interpretation. With stronger denoising of 95%, the final image is drastically improved in terms of contrast, SNR, and radiological confidence. This result demonstrates that iterative denoising is an interesting method for improving signal-to-noise ratio and for gaining more freedom in MR sequence parameter settings to improve



6 Contrast-optimized 3D PD FS SPACE of a 54-year-old female patient referred for a symptomatic medial cyst. The window levels (contrast and width) have been set equally for all sequences to highlight both signal and contrast changes. The contrast-optimized ID image allowed a better homogeneity and contrast within the cyst as well as the bone marrow and subcutaneous fat. Note the higher contrast in **6C** and **6D** between the quadriceps muscle and the adjacent subcutaneous fat compared to **6A** and **6B**.

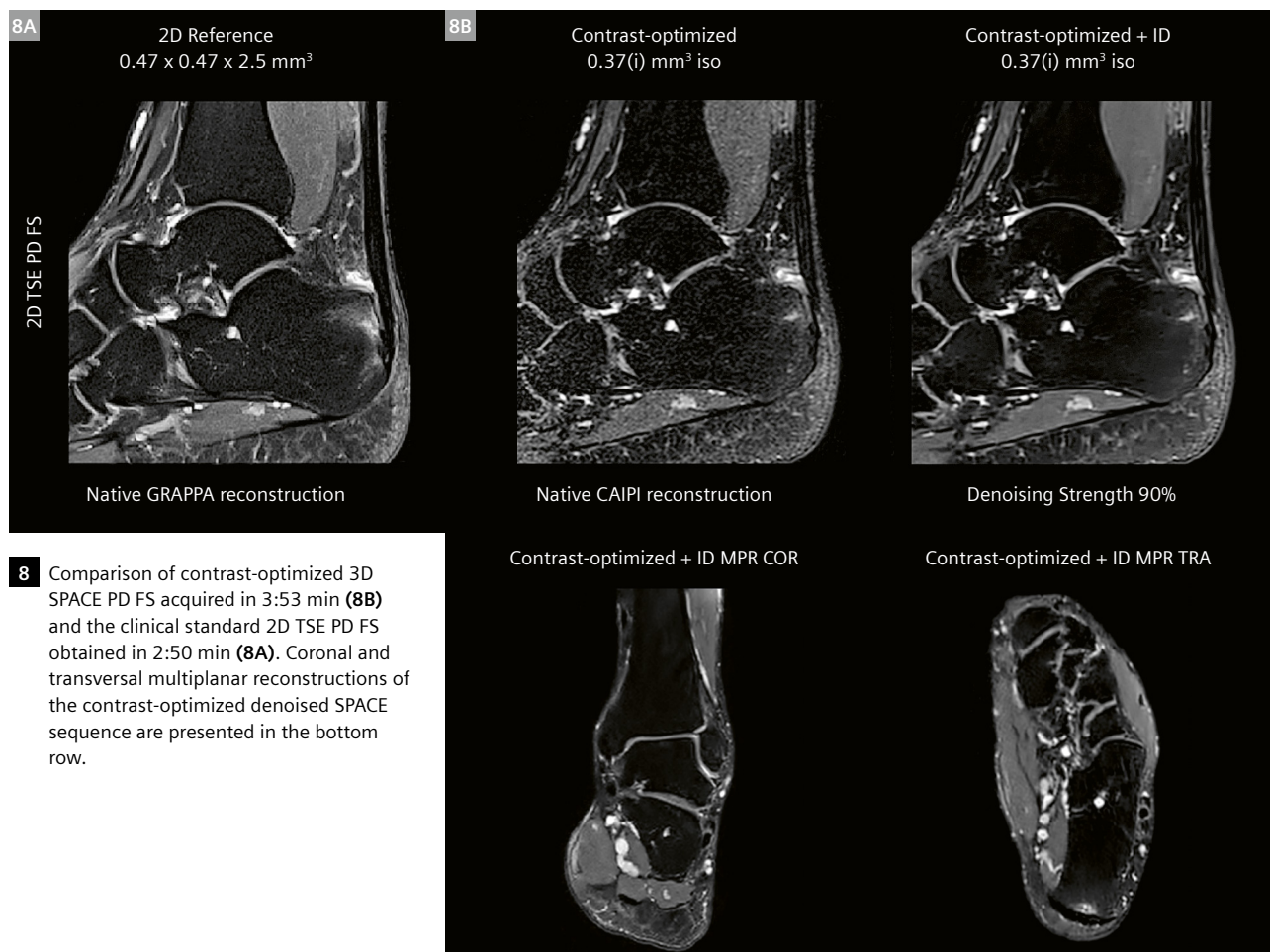
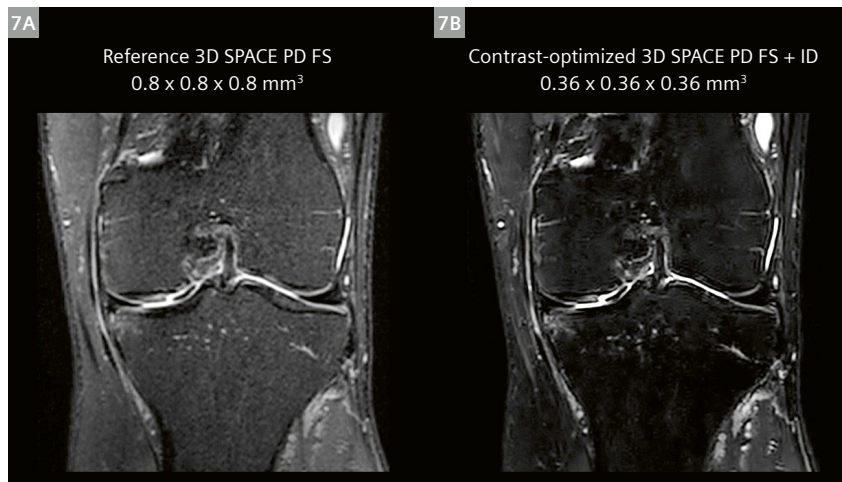
the image contrast and quality, even with the lower SNR produced by a 1.5T magnet.

Contrast-optimized SPACE ID yielded high-quality images with an effective fat suppression (allowing more precise detection of the bone marrow edema), along with noise reduction in the final image (Fig. 7). The accuracy

of the meniscus and cartilage visualization remained unchanged.

Finally, Figure 8 compares a clinical case of contrast-optimized 3D SPACE ankle with the 2D TSE standard. Interestingly, we were able to reproduce the overall image appearance, which is known to be difficult in MSK imaging when moving from 2D to 3D.

- 7** 71-year-old male with a medial meniscal flap and grade 3 chondropathy. The contrast-enhanced ID image (**7B**) allows better visualization of bone marrow edema in the medial tibial plateau compared to the standard image (**7A**) while preserving high-quality exploration of the meniscus and the weight-bearing cartilage.



- 8** Comparison of contrast-optimized 3D SPACE PD FS acquired in 3:53 min (**8B**) and the clinical standard 2D TSE PD FS obtained in 2:50 min (**8A**). Coronal and transversal multiplanar reconstructions of the contrast-optimized denoised SPACE sequence are presented in the bottom row.

Conclusion

Three-dimensional PD FS is a well-established MSK technique mostly used in knee and ankle joints, allowing for isotropic resolution imaging of meniscus and cartilage abnormalities. However, 3D MSK does have some weaknesses, such as lower signal-to-noise ratio and contrast quality compared to conventional 2D PD FS imaging. In this study, we attempted to resolve the insufficiencies of 3D SPACE imaging without altering the time-effectiveness of the sequence. Iterative denoising allowed a significant improvement in the diagnostic confidence of knee and ankle abnormalities. Image quality was assessed in terms of contrast, edge sharpness, signal/noise, and resolution. All these criteria were significantly improved by the ID reconstruction, except for signal/noise, which was maintained at a stable level to emphasize other image parameters.

The clinical value of the ID reconstruction was determined using major criteria such as the evaluation of ligaments, meniscus, cartilage, and subchondral bone changes. Both readers considered the evaluated SPACE variants combined with ID reconstruction to be more accurate, while performing equally on time-effectiveness.

We believe this contrast-optimized SPACE ID to be a promising, time-effective, all-in-one sequence. However, further studies with larger cohorts are needed to objectively evaluate the diagnostic performance of this sequence. Furthermore, multicenter evaluations should be conducted to confirm our findings.

In conclusion, we demonstrated that the iterative denoising reconstruction is a reliable technique for imaging the knee and ankle for internal disruptions, resulting in a better evaluation of the anatomical components of these joints.

Acknowledgments

The authors would like to thank Boris Mailhe for the iterative denoising core and Alexis Vaussy for initial testing of the SPACE ID prototype and the protocol optimization recommendations for MSK imaging. The authors would like to also thank the MR technologists for having carefully added the prototype sequence to the clinical workflow.

References

- 1 Gold GE, Busse RF, Beehler C, Han E, Brau AC, Beatty PJ, et al. Isotropic MRI of the knee with 3D fast spin-echo extended echo-train acquisition (XETA): initial experience. *AJR Am J Roentgenol*. 2007;188(5):1287–93.
- 2 Mugler JP 3rd. Optimized three-dimensional fast-spin-echo MRI. *J Magn Reson Imaging*. 2014;39(4):745–67.
- 3 Kijowski R, Davis KW, Woods MA, Lindstrom MJ, De Smet AA, Gold GE, et al. Knee joint: comprehensive assessment with 3D isotropic resolution fast spin-echo MR imaging-diagnostic performance compared with that of conventional MR imaging at 3.0 T. *Radiology*. 2009;252(2):486–95.
- 4 Kijowski R, Gold GE. Routine 3D magnetic resonance imaging of joints. *J Magn Reson Imaging*. 2011;33(4):758–71.
- 5 Breuer FA, Blaimer M, Mueller MF, Seiberlich N, Heidemann RM, Griswold MA, et al. Controlled aliasing in volumetric parallel imaging (2D CAIPIRINHA). *Magn Reson Med*. 2006;55(3):549–56.
- 6 Breuer F, Blaimer M, Griswold M, Jakob P. Controlled Aliasing in Parallel Imaging Results in Higher Acceleration (CAIPIRINHA). *MAGNETOM Flash*. 2012(1):135–142.
- 7 Paret M, Barral FG, Barles C, Doussin S. CAIPIRINHA and SPACE – a Winning Combination. *MAGNETOM Flash*. 2018(2):45–51.
- 8 Kannengiesser S, Mailhe B, Nadar M, Huber S, Kiefer B. Universal iterative denoising of complex-valued volumetric MR image data using supplementary information. In: *ISMRM Annual Meeting Proceedings [conference proceedings on the Internet]*; 2016 May; Singapore. Available from: <https://archive.ismr.org/2016/1779.html>
- 9 Vaussy A, Eliezer M, Menjot de Champfleury N, Le Bars E, Nguyen TH, Habas C, et al. Iterative Denoising Applied to 3D SPACE CAIPIRINHA: A New Approach to Accelerate 3D Brain Examination in Clinical Routine. *MAGNETOM Free.Max special issue*. 2020;26–34.
- 10 R Core Team. R: A Language and Environment for Statistical Computing. R Foundation for Statistical Computing. Vienna, Austria. 2020.
- 11 Landis JR, Koch GG. The measurement of observer agreement for categorical data. *Biometrics*. 1977;33(1):159–74.

Contact

Chadi Hlailhel, M.D.
Groupe Du Mail
19 Avenue Marie Reynoard
38100 Grenoble
France
chadi.hlailhel@groupe-du-mail.com



Thomas Troalen
Siemens Healthcare SAS
40 Avenue des Fruitières
93210, Saint-Denis
France
thomas.troalen@siemens-healthineers.com

Breast Biopsy Workflow with *syngo* MR XA20 – How I Do It

Sarah-Jane Lewis

Siemens Healthineers UK and Ireland

Background

During the investigation of a breast lump or suspicious lesion, the patient may undergo several modality examinations. The dynamic contrast-enhanced MRI scan is highly sensitive [1] at demonstrating lesions and may lead to the discovery of a lesion only visible on the MRI scan, a so-called MRI-only lesion. If the lesion is only visible with MR imaging, the biopsy must be performed under MRI guidance. Clinical sites that perform breast MRI in the UK are expected to either perform or have access to a referral site that performs MRI-guided biopsy.

This article provides an overview of MR-guided breast biopsy performed using the Breast Biopsy software, *syngo* MR XA20 version (Siemens Healthcare, Erlangen, Germany).

Introduction

A breast biopsy itself may involve several stages: A standard procedure involves a vacuum-assisted biopsy (VAB) using an MRI-compatible biopsy system. The biopsy console unit is not MRI-compatible and must remain outside the scan room. There are several manufacturers of such devices and the biopsy arm should be checked for MRI compatibility along with the foot pedal used to control the tissue removal. Targeting is performed using an MR Safe introducer kit that includes a needle guide for accurate positioning and an obturator that helps both to stem the flow of blood and to confirm the location. Once the main biopsy has been performed, the radiologist may leave a hookwire or marker *in situ* for further surgery or biopsy site evaluation. Sterile disposable grids are also required. Consequently, good preparation is essential before each examination due to the large amount of specialist consumable items needed. It is recommended that procedures are reviewed and workflows are practiced regularly at the clinical site to maintain the competency to perform breast biopsy. Clinical sites are expected to perform at least 10 biopsies a year to maintain their competency [1].

Dot

Patient View

+

Basic Patient View

✓

Routine

localizer

00:11

Breast Biopsy workflow

Advanced Application

Right or Left

Right

▼

+

Basic Decision

Right or Left

Right		Left	
t1_fl3d_nonfs_sag_1+2_right	07:41	t1_fl3d_nonfs_sag_1+2_left	07:41
<div> <div></div> <div>▶</div> <div>1</div> </div>		<div> <div></div> <div>▶</div> <div>2</div> </div>	
t1_tse_tra_right	02:04	t1_tse_tra_left	02:04
<div> <div></div> </div>		<div> <div></div> </div>	
t1_fl3d_sag_cavity_right	02:08	t1_fl3d_sag_cavity_left	02:08
<div> <div>▶</div> <div>1</div> </div>		<div> <div>▶</div> <div>2</div> </div>	

1 Right and left breast may be separated to activate specific coil elements

Equipment

The procedure was performed on a 1.5T MAGNETOM Sola system with *syngo* MR XA20 software and the Breast Biopsy software license. A grid system was used, which is available for the 2-/10-/16-channel and 2-/4-/8-channel Sentinelle Breast Coils, and the Breast BI 7 coil. The grid is the biopsy system used most in Great Britain and Ireland (GB&I) and is the method described in this article. The Breast Biopsy software, however, also supports the post and pillar approach in combination with the Breast BI7 coil.

Preparation

The patient is required to lie prone, and the procedure may take as long as 45 minutes. It would be advisable to encourage the patient to empty their bladder and to avoid heavy meals for a couple of hours prior to the procedure. A cannula is required for IV contrast. The patient may need to place their hands above their head in a "Superman-style" position, so it may be advisable to place the cannula in the wrist if the elbows are to be bent for the procedure. A useful procedure seen at several sites within GB&I is to have a meeting prior to the procedure and delegate the tasks required. For example, a metallic scalpel may be used, and a designated person will be responsible for making sure it is safely brought into, and removed from, the scanning room. Additionally, the radiologist performing the procedure should confirm the anatomical site or sites to be biopsied. This can be performed at a PACS workstation or the MR system itself. The location of the potential biopsy site is important as this can influence how the breast is positioned within the grid. With a biopsy site toward the axilla, the patient may need to lie slightly obliquely on the table to ensure the axillary tissue is pulled into the grid area. Equally, if the biopsy site is toward the chest wall, the breast tissue needs to be pulled quite firmly away from the chest into the grid. If a medial approach is considered, then the contra-lateral breast will need to be lifted out of the way using the breast plate and the grid and fiducial placed on the medial side. If the exact approach is not known beforehand, the breast will need to be compressed medially using a second grid with a second fiducial. Most radiologists will generally attempt a lateral approach if possible as the access is more open, therefore making the procedure easier. Once the patient is lying on the patient table with the cannula attached to the contrast pump, the breast should be immobilized within the biopsy grid device by providing moderate compression. The positioning of the grids should be supervised by the radiologist to ensure optimum compression. Compression is needed to immobilize the breast but also to prevent stretching or tenting of the subcutaneous tissue when the introducer needle is pushed in and out of the breast. Compressing the breasts also has the advantage of

creating a smaller volume of tissue to scan, which is useful in volume scanning to reduce the number of slices required. The level of compression also needs to be balanced against the risk of reducing visibility of the lesion by applying too firm a compression [2].

The fiducial should be placed in a grid opening. With the Sentinelle Breast Coil, the fiducial is placed at C4 as standard. The use of the same grid opening every time a biopsy is performed allows continuity and reduces any potential user error due to a wrong fiducial position. As the grid position is not fixed, a marker is crucial as it is used to establish a reference position for needle insertion.

Scanner protocols

The design of the biopsy scanning protocols varies slightly from that of the diagnostic protocol. The number of different sequences should be truncated to reduce the scanning time. The sequences will always start with a localizer. These should be looked at to assess the quality of the compression and to ensure that a good proportion of the breast tissue is included in the coil. If there is a roll of tissue above the grid, it may be possible to reposition the patient by releasing the grid and allowing more tissue to fall into the grid area. The localizer can also be used to assess the filling of the fiducial marker with diluted contrast medium when using the Siemens Healthineers Breast BI 7 coil and NORAS Breast Biopsy Set (NORAS MRI products, Höchberg, Germany). It may not be necessary to include any sequences prior to the dynamic run, the exception to this is if the suspected tumor area is shown particularly well on a non-enhanced sequence, such as T2 axial. Dynamic sequences will consist of a 3D gradient echo T1 in the sagittal plane without fat saturation. Sagittal acquisition is performed so that the slices are parallel to the grid plane. No angulation can be used. Inline subtraction is included for easier visualization of the tumor. The number of phases required should be discussed at the site level as there may be some delayed enhancement due to the compression of the breast and feeding blood vessels [2]. The initial phases are automatically loaded into the workflow as soon as they are reconstructed so these can be used to start the configuration whilst the later phases are obtained. Therefore, there is no time-saving advantage to keeping the number of dynamic phases too low. The automatic opening of the Breast Biopsy workflow is triggered by the **Advanced Application** add-in and, once completed, subsequent sequences will be loaded into the appropriate segments of the workflow. A decision within the strategy can be used to separate right and left breasts to have specific coil elements activated, as shown in Figure 1. Additionally, predetermined offsets in the sagittal dynamic blocks can be used to save a small amount of time when setting up the sequence.

Biopsy workflow

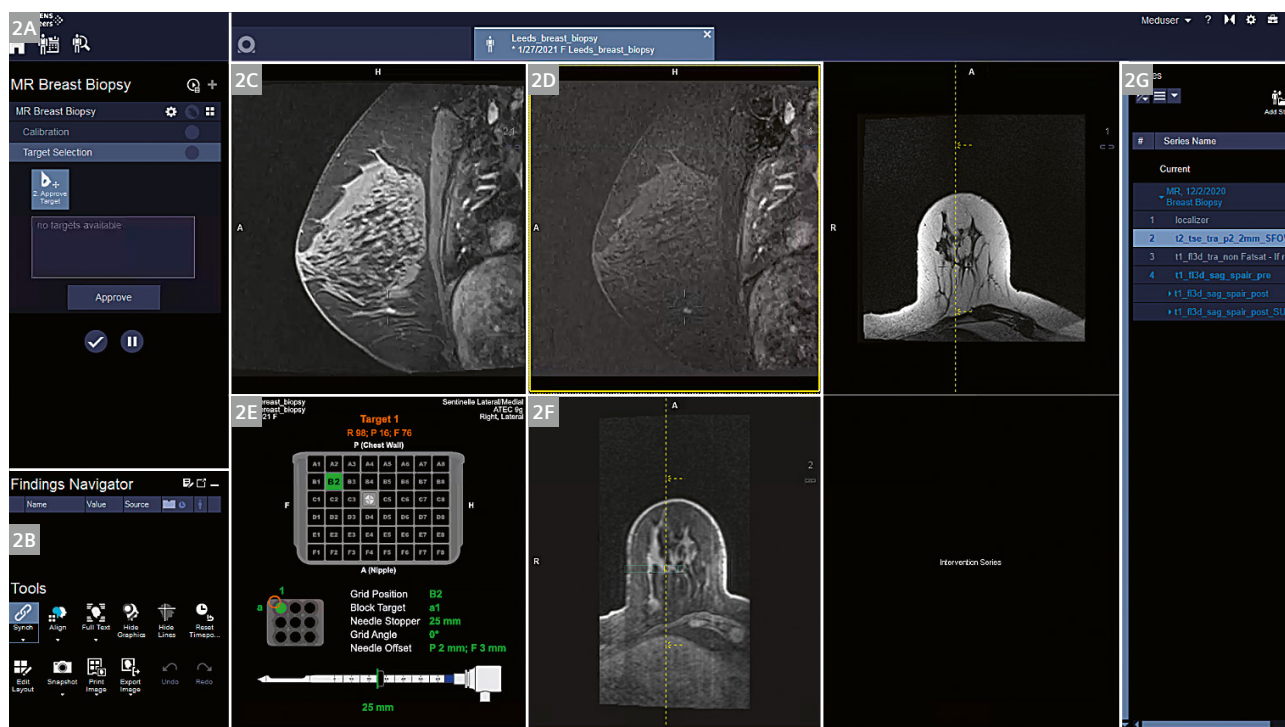
The patient is registered. During registration, the previous diagnostic images can be recalled from the PACS and will be available in the Breast Biopsy workflow. If this step is missed, then the images can be added to the Breast Biopsy workflow using the **Add Study** button in the Series Navigator. An overview of the whole layout is shown in Figure 2. Once the dynamic run is started, an IV injection is performed between the first and second phases, with the first phase acting as the subtraction mask or subtrahend. When the injection has been completed, your attention can turn to the Breast Biopsy workflow. The automated loading of sequences should have started, and the first dynamic phase can be used to begin the calibration step. The calibration workflow step contains all the information relating to the equipment used and the position of the fiducial. This step can be completed by the technologist in conjunction with the radiologist. The device menu enables the user to select from a list of pre-configured settings, depending on what equipment is in use.

In the normal scenario, only a small number of presets should be needed as similar methods will be used each time. Usually, a site only possesses one biopsy coil and the same type of needle device kit is normally used. If the fiducial is placed into the same grid square each time, this naturally limits the number of presets needed. When configuring presets for the Sentinelle Breast Coils, only

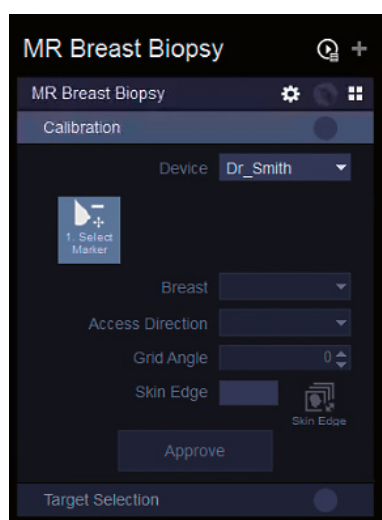
a C4 marker position is possible. These presets can be configured prior to scanning and quickly amended during the exam, if needed. Configuration of the device setting presets is accessed via the cogwheel icon as shown in Figure 3. The presets can be named as required after the radiologist using them or the individual needle types as shown in Figure 4.

Once the device preset has been selected, then the fiducial needs to be located. As soon as the images start arriving in the workflow, they will load with the native sagittal images in the top-left segment and the inline subtractions in the top middle segment. The middle mouse button or the keyboard arrows allow you to scroll through the images to locate the fiducial, which will be seen in cross-section on the sagittal as a dot. In the bottom middle segment, an MPR image allows you to see the length of the fiducial in the transverse plane. Click the **Marker Position** icon to activate the crosshairs. To mark the fiducial, place the crosshairs on the end of the fiducial closest to the breast as shown in Figure 5. Click the **Approve Marker** icon to confirm the marker position and set the **Access Direction**, which can be seen in the drop-down field. As the breast is compressed and the fiducial is pushed against it in the grid, the fiducial is marking the skin surface.

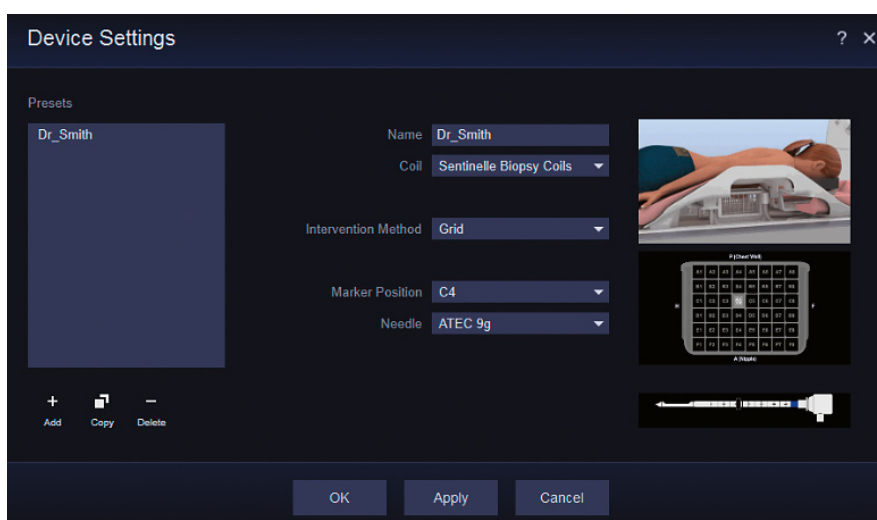
The slice position of the skin surface is visible in the **Skin Edge** field, which gives a slice position in the right or left direction. This skin surface location is needed for the depth measurement calculation. If the radiologist wants to



2 2A Workflow steps, 2B Tools and Findings Navigator, 2C targeting segment with native sagittal images, 2D subtracted sagittal images, 2E graphics for the targeting information, 2F MPR of native images, 2G Series Navigator



3 Calibration step



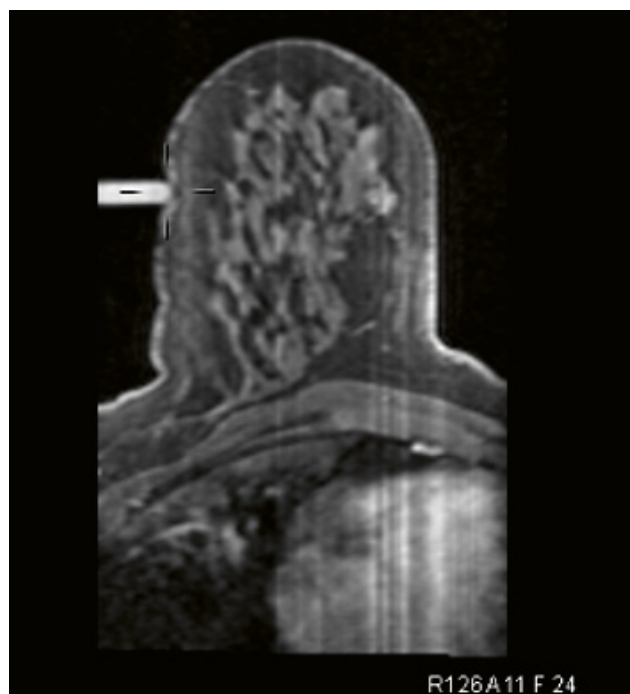
4 Device settings

change this skin surface, this can be done by clicking the **Skin Edge** button. By scrolling through the native sagittal images, you can visualize the grid and the skin protruding through the grid squares. By clicking **Approve** (skin edge), you reset the skin edge and a purple grid overlay allows you to visualize where the skin edge and grid are. Selecting the device preset and determining the marker position are necessary calibration steps that must be completed prior to locating the target lesion. Click **Approve** to complete

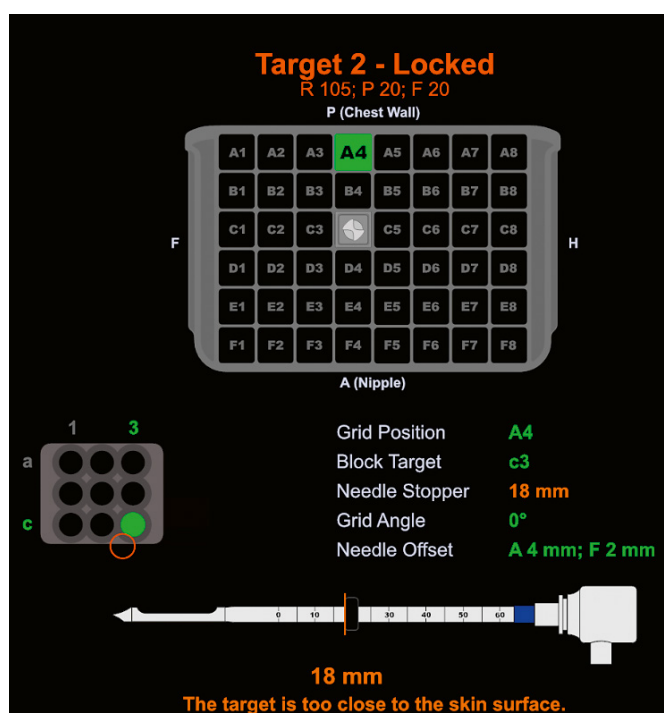
the **Calibration** workflow step and lock these values in.

If a double fiducial method has been used and then subsequently the alternate fiducial needs to be used, the preset can be changed mid-workflow. This might be needed if a lateral approach was planned but then the tumor position dictated that a medial approach was needed.

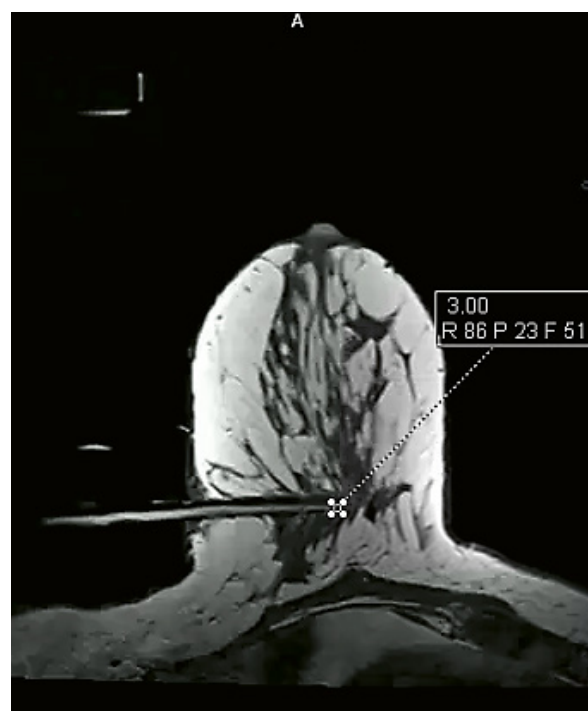
After approving the **Calibration** step, the **Target Selection** step is opened. The **Approve Target** tool is active, and the mouse pointer is displayed as crosshairs. If this is not required at this time, then the escape key can deactivate the tool. The radiologist can now view all images to see where the biopsy needs to be performed. Once a site has been chosen, the **Add Target** tool can be activated again and a mouse click on the lesion creates a target. At this point, the target has not yet been confirmed and pressing **Escape** removes the target. Alternatively, simply clicking in another place moves the target. Once the radiologist is satisfied with the target, the **Approve Target** button can be clicked. After this action, a finding will be created with images of the target, which can then be sent to the PACS. The target also appears in a list of targets that can be displayed on the Select&GO panels in the scan room. This is useful if multiple targets are obtained. The software has now calculated the depth and position of the target and this is displayed in the bottom-left segment. The graphic (Fig. 6) shows the exact position in the coordinate system, so this can be cross-referenced later with the pixel lens, if needed. Additionally, the needle system is displayed along with the depth measurement. If the target is within 20 mm of the skin surface on the fiducial side, then a warning will be displayed. The decision to proceed or not then lies with the radiologist. The side of the breast on the non-fiducial side has not been marked or delineated from the system, so the only limitation here is the depth of the lesion and the limitations of the needle system. On a small



5 Marking the fiducial



6 Graphic showing the exact target position in the coordinate system



7 Transversal scan at the level of the obturator

breast, the targeting can be quite close to the far edge of the breast and no warning is issued, so the staff must carefully check that they are not going to biopsy partially outside of the breast. The biopsy needle samples from a trough or notch along the length of the needle. The calculated depth positions the target in the middle of the notch, meaning that some of the needle and notch extends beyond the target point. The target coordinate display also gives information about the target selected by the radiologist and the nearest possible needle block position. The available target positions are limited by the grid walls themselves, and the needle block only has pre-determined positions. The red circle shows the target position marked and the green circle shows the nearest possible grid block opening. The **Needle Offset** shows the distance in mm that differs between these two positions. If the position is not precise due to the internal wall of the needle block, then the radiologist can make the decision to remove the needle block and perform the biopsy freehand. This requires experience and a steady hand as the needle block helps keep the biopsy arm perpendicular to the grid. If the position of the biopsy is not perfect due to the grid wall, not much can be done to move the needle itself to this position. However, when performing the vacuum biopsy, the radiologist can decide to concentrate the biopsy in this direction. So in Figure 6, the red circle/lesion is in a 7 o'clock position relative to the green circle/needle, so the radiologist could decide to perform more biopsy samples

here rather than more posteriorly toward the chest wall. Select the desired target and click **Send** to display the target coordinates on the Select&GO display in the scan room. In the example in Figure 6, the target is within 20 mm of the skin surface, so a warning is issued.

The first part of the intervention involves inserting the coaxial introducer sheath to create a pathway to the target. The patient table should be moved out of the scanner bore and the table lock applied from the Select&GO display. The radiologist will then inject some local anesthetic into the desired area through the biopsy grid. As soon as the area is numb, a small cut is made with a scalpel. Then the needle block can be inserted into the appropriate grid segment. If the required segment happens to be C4, where the fiducial is, then this will need to be carefully removed to make way for the needle block. Once the needle block is *in situ*, the radiologist can view the Select&GO display and select the depth measurement. Depth markers on the introducer sheath are used to insert the needle to the calculated depth, within the correct position in the needle block. Once the coaxial introducer has created the pathway, then the inner stylet can be withdrawn and replaced with the obturator. The table is unlocked, and the patient table is moved back into the scanner bore. A transverse scan is performed at the level of the obturator as shown in Figure 7. This scan can be performed at a slightly higher resolution than the dynamic run and is used to confirm the position of the obturator and can be positioned using the

known coordinates of the target as given in the target graphic. The transverse scan is looked at to confirm that the obturator is in a good position relative to the target. This workflow needs to be performed quickly as ideally the lesion would still retain some contrast on this scan, to be able to visualize it. If the obturator is not in the ideal position, the radiologist can either decide to reinsert the stylet and adjust the depth or can adjust on the fly. For example, frequently the intervention pushes the lesion slightly further away, toward the far side of the breast side. In this case, radiologists may make the adjustment to this as they go, simply by pushing the biopsy device further in.

Once the vacuum biopsy is completed, a post-biopsy image is acquired. A large void will be seen at the site of the biopsy and it can be confirmed that the lesion has been removed or sampled. It is likely that a post-biopsy clip will then be implanted to act as a marker for further imaging or interventions. Many sites do not perform imaging after the implantation, as it can be difficult to see a small clip in a large area of bleeding.

The findings created contain images that can be sent to the PACS using the **Save and Send** function when closing the MR Breast Biopsy workflow.

Troubleshooting tips

There may be occasions when the configuration needs to be changed during the exam. For example, the needle type may need to be changed if the biopsy is located quite close to the skin edge. This can be done by configuration of a device preset on the fly. This can be performed in the device

settings by copying the current preset and then changing the needle type. This will be loaded automatically without any changes to the original images, fiducial position and targeting. However, you can only access the **Device Settings** menu if you selected **Modify** in the **Calibration** step. Also, you may want to change the direction from lateral to medial approach. Again, this can be done by clicking the **Modify** button in the **Calibration** step and redefining the marker position on the medial side.

Sometimes you will need to view the sagittal images in an alternate orthogonal plane. This can be done by using the blue orientation cube on the right side of the display segments. By left mouse clicking on the cube you rotate through sagittal, transverse and coronal in turn. By right-clicking on the cube, you can select the orientation of choice. Additionally, you may want to view the subtraction images as a maximum intensity projection (MIP), which is done by selecting **MIP** in the bottom-left corner menu.

With **MIP** selected, you can scroll through the phases using the movie tool, which you can start by pressing the space-bar or by opening the top-left corner menu. If you have left the orientation of the images in a slightly odd position and wish to reset them, double-clicking the blue orientation cube will reset the orientation back to sagittal.

Acknowledgment

Thank you to the Radiology Department at St. James Hospital, Leeds, England for the kind use of their images.

References

- 1 Sardanelli et al., Magnetic resonance imaging of the breast: Recommendations from the EUSOMA working group. *Eur J Cancer*. 2010 May;46(8):1296-316. doi: 10.1016/j.ejca.2010.02.015. Epub 2010 Mar 19.
- 2 El Khouli et al., The effects of applying breast compression in dynamic contrast-material enhanced MRI Imaging. *Radiology*. 2014 Jul;272(1):79-90. doi: 10.1148/radiol.14131384. Epub 2014 Mar 12.

Contact

Sarah-Jane Lewis
MRI Applications Specialist
Siemens Healthcare Limited
United Kingdom
Phone: +44 7808 822444
sarah-jane.lewis@siemens-healthineers.com



Pushing the Limits of Accuracy in MRI – A Perspective

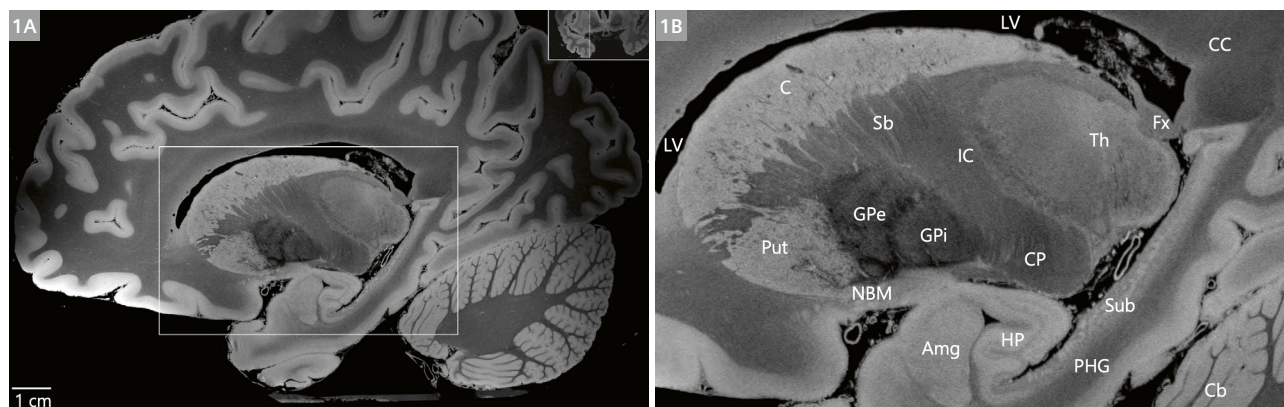
John E Kirsch, Ph.D.

Athinoula A Martinos Center for Biomedical Imaging, Massachusetts General Hospital,
Department of Radiology, Charlestown, MA, USA

Introduction

I am pretty sure that magnetic fields were never intended to be perfectly homogeneous or to vary precisely linearly in space at exactly a certain moment in time. At the very least, it is probably plausible to say that it was not what James Clerk Maxwell was thinking when he formulated his famous equations. Yet in 2021, magnetic resonance imaging (MRI) is used to do just about everything in healthcare, including guiding the placement of an electrode deep into the interior of the human brain at better than 1 mm accuracy to help patients with epilepsy, or producing exquisite anatomical information at 100 micron isotropic resolution (Fig 1).

MRI is based on magnetic fields throughout the entire measurement and imaging process, starting with a static external magnetic field that magnetizes the hydrogen nuclei in the body and ending with producing an image from that magnetization. The accuracy of those fields therefore ultimately determines the precision of the image outcome. The position of a voxel in a digital image representation of the anatomy is based on the singular assumption that the magnetic fields are precisely known everywhere in space and time. Deviation from this and there will be a proportional inaccuracy associated with the position of that voxel.



1 100 micron thick sagittal slice through an ex-vivo human brain acquired with the MAGNETOM 7T Classic showing delineation of basal ganglia, diencephalon, and medial temporal neuroanatomy at 100 micron resolution (1A). A zoomed view of the striatum, amygdala (Amg), and hippocampus (HP) (within the white rectangle in 1A) is shown in (1B).

Neuroanatomic abbreviations: C = caudate; Cb = cerebellum; CC = corpus callosum; CP = cerebral peduncle; Fx = fornix; GPe = globus pallidus externa; GPi = globus pallidus interna; IC = internal capsule; LV = lateral ventricle; NBM = nucleus basalis of Meynert; PHG = parahippocampal gyrus; Put = putamen; Sb = striatal bridges; Sub = subicular cortices; Th = thalamus.

With permission: Brian L Edlow, MD, Massachusetts General Hospital. BL Edlow, A Mareyam, A Horn, et al., 7 Tesla MRI of the ex vivo human brain at 100 micron resolution. *Sci Data* 6, 244 (2019). <https://doi.org/10.1038/s41597-019-0254-8>.

There are many applications now that rely on the informational accuracy of MRI, whether it be with its signal amplitude, phase, or position in space. Nowhere is this more evident than when using MRI for stereotactic planning, where spatial accuracy is paramount. High resolution isotropic 3D MR imaging has become the modality of choice for radiation treatment planning or surgical implantation procedures. Inaccuracies in the spatial position of the anatomy with respect to external fiducial markers can lead to potentially catastrophic outcomes. Spatial precision is also a requirement for personalized prosthetic modeling, where localized errors in position can cause painful misalignment for the recipient. Tissue morphometry and segmentation are being used more and more for medical and therapeutic evaluation that relies heavily on the volumetric precision not only in a given dataset but also longitudinally over time.

But spatial accuracy is not the only thing that relies on magnetic fields. In recent years, MRI is becoming more quantitative where accuracy in its signal amplitude and phase are necessary as well. Flow quantification in vascular and cardiac applications relies heavily on the precision of the signal phase, as does high-intensity focused ultrasound (HIFU) and other therapeutic procedures that use the phase information for MR thermometry to monitor tissue response. MR elastography requires the phase information to measure tissue stiffness in liver disease. Applications that demand accuracy and reproducibility in the signal amplitude also exist. Quantitative biomarkers such as the Apparent Diffusion Coefficient (ADC) in diffusion-weighted MRI rely on the signal amplitude decay associated with diffusion sensitization of water motion to probe tissues on a microscopic scale. And, fMRI requires extreme temporal stability of the signal magnitude to detect the statistical significance of the blood oxygen level dependence (BOLD) response in brain activity.

In the early days of MRI, we pretty much focused on just trying to maximize the signal-to-noise ratio (SNR) and simply hoped that after a 15-minute acquisition the scan would yield a reasonable facsimile of the human anatomy, whether it be of the brain, a knee, or the liver. But in this age of precision medicine, MRI is becoming much more quantitative, requiring equally greater accuracy. Just getting an image is no longer a reasonable expectation. MRI is now expected to be perfect in every way. Let us take a brief look into just how perfect, or not-so-perfect, it is.

Signal encoding

MRI of course begins with an external static B_0 magnetic field to create the initial magnetization. The MR signal that eventually is generated will possess characteristics of amplitude, phase, and frequency. Essentially, all three of

these features are based on magnetic fields as described by the Larmor equation. For them to be accurate, this means that the magnetic fields that they are based on must also be accurate. Note that there are three magnetic fields that we deal with in MRI: B_0 , B_1^+ , and B_1^- . B_1^+ and B_1^- are the transmission and reception fields, respectively, and are perpendicular to the B_0 field in order to rotate the magnetization and detect it. Although the B_1 fields are clearly important and deserving of discussions about their accuracy, it is the B_0 field that is the focus here since it is ultimately what encodes the MR signal that gets detected and generates the image. Therefore, for the remainder of this paper only the B_0 magnetic fields will be discussed.

The MR experiment can be viewed as having four basic time-sequential elements – preparation, excitation, encoding, and readout. During preparation, the initial state of the magnetization for the experiment becomes defined. This may be an inversion preparation that might be applied for a specific type of tissue contrast, or it might be a type of saturation to suppress the magnetization from a specific tissue such as fat. In this stage, the accuracy of the B_0 field could be argued as playing a lesser role, primarily associated with the spatial uniformity of the outcome.

After the initial preparation, excitation is then carried out to rotate the magnetization out of the B_0 direction to create a transverse component which eventually becomes detected. This process relies on the resonance condition between RF transmission and magnetization, whereby their frequencies must be matched to produce the action of excitation and the rotation of the magnetization. By applying a spatially varying gradient field (G) during excitation one can then selectively excite a specific region in space. Here, the total magnetic field, $B_{0,tot}$ (comprised of the summation of the main magnetic field, B_0 , and the gradient field, G) plays a significant role, since a one-to-one relationship will exist between the excitation of a physical location in space that matches the resonance condition according to the Larmor equation. Transmission at a specified frequency and bandwidth will produce excitation anywhere in physical space with a given slice thickness where it matches the Larmor frequency of the magnetization. For this to be accurate requires precision of $B_{0,tot}$ and therefore the main magnetic field, B_0 , and the gradient field, G .

The encoding process is facilitated by applying G magnetic fields that spatially vary the B_0 magnetic field in a well-behaving manner so that signal can be mapped uniquely to different points in physical space. Gradient pulses of a given direction, amplitude, and duration encode the signal in k -space, the Fourier counterpart of image space, with the coordinates of k_x , k_y , and k_z . The action of the encoding process is to define the starting point coordinates in k -space for the readout process to follow, and the value of k will be based on the time

integration of the gradient pulsing. That said, the accuracy of the k -space encoding will therefore be defined by the accuracy of the gradient pulsing. In addition, however, since the transverse magnetization experiences the *total* magnetic field $B_{0,tot}$, the uniformity of the main magnetic field B_0 also plays an important role in the accuracy.

The final step of the MR experiment is the signal readout when the magnetization is detected and digitally sampled. k -space gets sampled according to the gradient pulsing that is applied simultaneously during the detection process. The k -space trajectory in readout will be based on the direction, amplitude, and duration of the gradient pulsing. Therefore, the trajectory will be determined by the precision of the gradient pulsing. And, as with the encoding process, the transverse magnetization experiences $B_{0,tot}$, so the readout accuracy will also depend on the uniformity of B_0 as well.

Historical progression

The spatial accuracy and temporal stability of the main static B_0 magnetic field and the pulsed G gradient magnetic fields has gone through different progression through the years. Early magnets were very large and heavy, and their spatial uniformity, or homogeneity, was in general quite poor. As the engineering design and manufacturing improved, magnet homogeneity also improved. However, other factors did not necessarily always allow continual improvement in the homogeneity. For example, a demand existed for wider and shorter bore designs to increase patient comfort, and siting requirements became more challenging for installing magnets in much smaller footprints. As a result, even though magnets progressively have become higher in field strength and more reliable and efficient, attaining the greatest homogeneity across a large imaging volume is not the only factor that is considered in present magnet technology.

Some amount of compensation for this can come from the implementation of active shimming with coils that generate 2nd-order spatial – or more recently even 3rd-order – harmonic correction of the static B_0 field. But it takes space to accommodate these extra shim coils in the bore, and this may be counterproductive with the ever-increasing demand for wider bore systems. For accuracy and precision, magnet homogeneity is what matters. But the final design will ultimately consider these other factors as well.

Probably what has progressed the most in the past decades is the gradient performance (on this point, readers can refer to the recent comprehensive historical summary “An Attempt to Reconstruct the History of Gradient-System Technology at Siemens” by Franz Schmitt et al. in the 2020 ISMRM issue of MAGNETOM Flash (77) 2/2020). In the early- to mid-1980s, gradient coils were unshielded, which

meant that without compensation the field errors were on the order of 20% of the nominal amplitude of the gradient pulsing. Performance-wise, pulse rise times were typically 1500 μ secs or even longer in duration, and the maximum gradient amplitudes were no greater than about 3 mT/m. Since that time, continual improvements in power amplifiers, gradient coil design, and manufacturing have led to actively shielded configurations that have force compensation to minimize mechanical torque and vibrations, as well as counter windings to minimize higher-spatial-order eddy currents. Errors are reduced by several orders of magnitude or more, and gradient performance on contemporary whole-body clinical systems now have 200 T/m/s slew rates that allow pulse rise times of less than 100 μ secs and amplitudes up to 80 mT/m amplitudes. Digital precision to control arbitrary and complex gradient waveforms and their pre-emphasis to minimize eddy currents has steadily improved over the years, from 12 bits, to 16 bits, and up to 20 bits or higher.

Specialized gradient coil designs have most recently dramatically increased performance to as high as an astonishing 600 T/m/s and 500 mT/m. However, such fantastic improvements have not come without some compromises as well. In order to achieve these levels and stay within safe limits of peripheral nerve stimulation in the human body, the accuracy and extent of the spatial linearity of such gradient fields can be constrained.

The steady improvements in magnet, shim, and gradient coil design over the decades have allowed for rapid expansion of the types of acquisitions and applications that are now achievable with MRI. However, spatial and quantitative accuracy has not necessarily been the only metric by which contemporary systems are judged. Yet it can be considered just as critical and just as important.

Confounding factors (and where things can go wrong)

To have an appreciation for what it actually means to achieve better than 1 mm spatial accuracy or to produce an image with 100 micron resolution is to also have a realistic appreciation for what can go wrong. This became readily apparent to me very early in my career as an MRI scientist. My first role was to develop new applications, and what I found more times than not was that theory rarely behaved the same way in actual practice. And when it comes to the magnetic fields there are many things that can occur to cause these fields to distort in the real world, as shown in Table 1.

The primary objective of the magnet static B_0 magnetic field is to possess perfect uniformity everywhere in space. Since the B_0 field defines the initial state of the magnetization and its encoding, spatial non-uniformities and imperfections are a fundamental source of error. The

magnet itself is of course finite in size. As such, it will possess a nominal field strength in the middle of the bore and zero field strength at some distance far away. Therefore, at some point as you move away from the isocenter yet still are within the imaging field of view of spatial encoding, the B_0 field will taper off and the required homogeneity is lost. There exists a so-called “sweet spot” where the uniformity of the field is the highest.

One of the most common things that can lead to errors in the static magnetic field are the spatial distributions of the different magnetic susceptibility (χ) that exist in tissues and objects (Fig. 2). This physical property determines the B_0 magnetic field that that medium experiences. Most soft tissues are quite similar, so the distortions of the field are negligible. However, the χ of bone and air are quite different from soft tissue and their presence can cause significant local distortions in B_0 . And of course, foreign objects such as surgical or therapeutic implants that might be made of a type of metal possessing very

different properties of χ can produce very large spatial distortions of B_0 near the object.

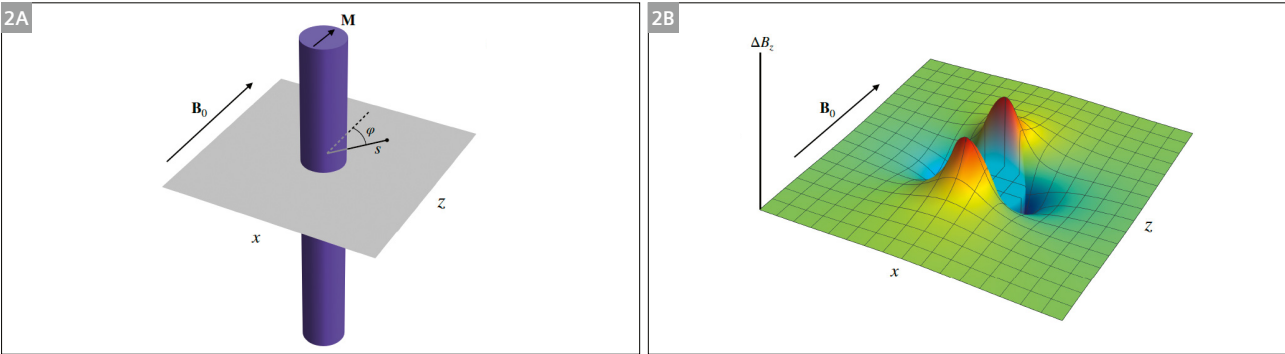
The molecular environment that surrounds hydrogen nuclei causes small but observable changes in the microscopic magnetic field environment known as chemical shift. Because fat and water in tissues have a frequency shift that equates to roughly 3.5 ppm of magnetic field difference, this means that the signal from each will originate from different locations in space. The most common example of this is pixel misregistration where fat will be located at slightly different positions in the field-of-view from water. Excitation of fat will also occur at different positions from water.

These are static B_0 factors. But what about dynamic errors that are caused by external influences or the pulsing of the gradient G fields necessary to encode the MR signal? In urban areas like New York City, the environment can be a “firestorm” of magnetic fields that are constantly fluctuating all around you. A common source are subways, not so much because of the moving metallic trains but because of power lines that can produce strong magnetic fields from surges needed to move the trains. Although Siemens Healthineers has a unique solution for protecting the magnet from such external B_0 perturbations, if an MRI scanner is simply too close it can lead to measurable errors if it occurs when a scan is being done at that time.

Faraday’s law tells us that a magnetic field that changes in time will generate an electric field. When a gradient is pulsed, it changes the total magnetic field $B_{0,tot}$ dynamically over time at a given point in space. This will therefore produce a countering eddy-current induced magnetic field on conductive surfaces that can then distort G and in turn $B_{0,tot}$ dynamically. Such eddy-current fields can come from implants or objects that have conductive components

Static and dynamic B_0 magnetic field	Dynamic G magnetic field
Finite shim volume	Eddy currents
Magnetic susceptibility	Concomitant fields
Chemical shift	Finite spatial linearity
External influences	Calibration and regulation
	Mechanical vibration
	Heating and drift

Table 1: Some of the sources of static B_0 and dynamic G errors.



2 Localized magnetic susceptibility induced B_0 distortion in the presence of a cylinder containing uniform susceptibility that is greater than the surrounding external environment. (2A): mathematical model showing the orientation of the cylinder relative to the main static B_0 magnetic field. (2B): theoretical simulation of the distortion of the B_0 field. This model demonstrates the origins of the Blood Oxygen Level Dependent (BOLD) effect in the microvasculature in regions of brain activation.
With permission: Bradley R Buchbinder, MD, Massachusetts General Hospital. BR Buchbinder. Chapter 4: Functional magnetic resonance imaging. Handbook of Clinical Neurology. Vol 135. Neuroimaging, Part I. pp 61-92, JC Masdeu and RG Gonzalez, Editors, Elsevier BV (2016). <https://doi.org/10.1016/B978-0-444-53485-9.00004-0>

and surfaces, but the dominant source is from the conductive cryoshields within the magnet itself. As previously mentioned, actively shielded gradient coils are designed to minimize this, but the high performance of modern systems will still generate measurable errors within the imaging volume caused by these eddy currents.

Another source of error caused by pulsing the gradients is the additional terms commonly referred to as Maxwell concomitant gradients. According to Maxwell's equations, it can be shown that when producing a spatially varying gradient field, the actual total effect contains higher-spatial-order mathematical terms that are secondary or "concomitant" fields over and above the spatial linear term we wish to produce for encoding purposes. The extent of their contribution to errors are primarily proportional to the square of the magnitude of the gradient strength, the square of the position away from isocenter, and are inversely proportional to the main magnetic field strength. Therefore, large-gradient amplitudes of pulsing such as what are used in diffusion applications can produce appreciable errors from this source.

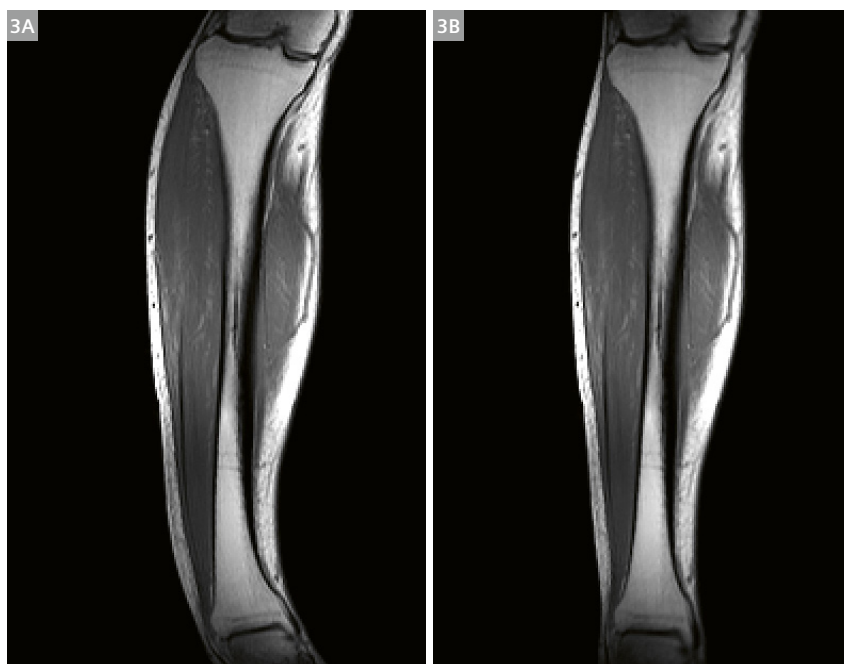
Aside from these physics-based phenomena, there are also several engineering factors that also can contribute to the overall errors associated with the gradient fields. First, like the magnet, the gradient coil is finite. As such, this will mean that the fields that it generates will eventually fall off away from the isocenter. Additionally, with the increased performance of modern gradients it is necessary to consider peripheral nerve stimulation and other safety constraints that will limit the extent of spatial linearity of

the gradient fields. Figure 3 demonstrates how significant the spatial distortion can be if corrections of these errors are not applied.

Calibration and regulation of the amplifier output that drives the production of the gradient field are important aspects of accurate field generation. When a pulse sequence instruction specifies the amplitude and duration of a gradient pulse, this information is sent to the amplifier to convert the digital instruction to an analog electrical current which then drives the gradient coil generating the requested G field. Too much current will produce a G that is higher than what the instruction calls for. Calibrating this is therefore necessary to ensure accurate field generation (Fig. 4). And proper regulation is required to make sure that the baseline current always remains zero when no gradient field is being pulsed.

Rapidly changing magnetic fields associated with gradient pulsing also induce Lorentz forces that in turn produce mechanical vibrations. This of course also leads to the quite familiar knocking sounds associated with all MRI scanners. But it also can produce physical displacement. Although minor in most cases now that modern gradient coils are designed with force compensation to mitigate these vibrations, it cannot be completely ruled out as a potential factor.

The amount of current required to generate the gradient fields can be quite large, which over time produces a lot of heat that must be mitigated with cooling. However, state-of-the-art applications that exploit the maximum gradient performance over longer periods of time can lead



3 Large FOV coronal T1-weighted spin echo slice through the lower leg and calf muscle. Without correcting for the spatial nonlinearity of the gradient field, the image is geometrically distorted (**3A**). Gradient related nonlinearity distortion is completely predictable if the gradient field is known and can therefore be corrected by pixel reformatting/remapping (**3B**).

to gradual drifting of the total B_0 field over the duration of the MR experiment.

And finally, with all these things that can go awry, when it is all said and done, Siemens Healthineers continues to strive to improve and perfect things, and we are therefore able to achieve some of the most astounding diagnostic images and remarkable outcomes with MRI, that continues to significantly make a positive impact on healthcare.

MRI applications

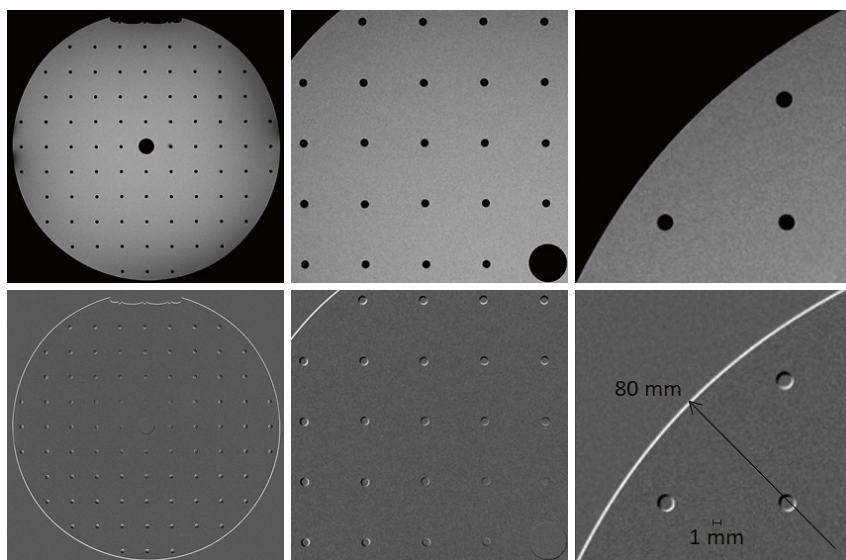
Once magnetization is transverse after the excitation process, it becomes vulnerable to all the inaccuracies of the B_0 -related magnetic fields, whether from the main static magnetic field or from the pulsing of the gradients. This will be true regardless of the application. However, it is the application and what information it is trying to extract from the human body that ultimately determines whether the errors in $B_{0,tot}$ make a difference or not. For a given B_0 error somewhere in space, the spatial distortion or signal phase deviation may be large or small at that location based on the technique of measurement and its application.

Specific details of the myriad of MRI applications that now exist on modern scanners are beyond the scope of this paper. But there are several basic aspects that can make an application more or less sensitive to the $B_{0,tot}$ field and its errors. One of these is the MR signal readout. How fast one samples the signal and encodes it in k -space

defines the field sensitivity of the MR experiment. The longer this duration, the more time passes for the transverse magnetization to evolve in the $B_{0,tot}$ field that it experiences. Errors in the field increase the magnitude of the error in the signal, as the magnetization continues to evolve during the sampling process.

Single-shot echo-planar-imaging (EPI) applications such as functional MRI (fMRI), diffusion tensor imaging (DTI), and dynamic susceptibility contrast (DSC) are at one extreme of the sensitivity spectrum where the entire readout of the MRI signal and complete sampling of k -space is done with a single magnetization preparation. Ironically, although this provides the ability to produce rapid “freeze-frame” results in a matter of 20 or 40 ms per image, on the scale of evolution of the transverse magnetization this is quite slow. These techniques are therefore extremely sensitive to B_0 errors leading to substantial spatial distortions, and signal magnitude and phase deviations.

In the more traditional steady-state Cartesian sampling used in gradient echo (GRE), spin echo (SE) or turbo spin echo (TSE) techniques, the duration of the readout of a line in k -space, and thus the sensitivity of the scan, is determined by different factors. On the one hand, high-bandwidth sampling associated with short readout durations offers the ability to shorten timing such as echo time (TE) or echo spacing with less sensitivity to B_0 errors, but is accomplished at the expense of increased noise and thus lower SNR. On the other hand, longer durations of lower bandwidth sampling improve the SNR but at the



4 Effect of gradient calibration. A high resolution image of a phantom specially designed to assess spatial accuracy is shown in the upper row at various magnifications. The bottom row is a difference map between two slightly different calibrations. Note that since calibration is relative, the absolute spatial error will depend on the distance away from isocenter.

expense of increased sensitivity to B_0 errors. And, what fights against this is that higher spatial resolution necessitates higher k -space sampling of the information requiring larger gradient pulsing which can introduce greater error. So, although one may spatially encode an image with high resolution, the inaccuracy in the spatial position may also be higher.

Cartesian sampling is not the only method used to sample and fill k -space. Depending on the application, spiral or radial sampling trajectories can be of benefit. For example, ultrashort echo times are necessary to catch the MR signal before it rapidly decays away in solids such as cortical bone, or regions of interest that contain large localized susceptibility-based B_0 inhomogeneities, such as lung parenchyma. Each sampled data point in k -space will only be as accurate as the gradient pulsing that is required to encode that sample with the correct k -space coordinates. The more complex the k -space trajectory and the longer the readout of the sampling, the greater the potential for error in the mapping.

And finally, as perfect as we might strive to make the magnetic fields and signal encoding, the cooperation of the subject may end up being the single most important confounding factor. The longer the scan is, the greater the probability that the patient will move during the scan which can compromise the accuracy of the outcome. Navigator signals and tracking devices are prospective strategies used to attempt to mitigate some of these inevitable errors due to motion, but these as well ultimately rely on the accuracy of the B_0 fields to correct things.

On the not-so-distant horizon

As the MRI applications become more sophisticated, so do the ways to produce more accurate and reliable results. Clearly, engineering and manufacturing continues to

improve the performance of MRI scanners, and Siemens Healthineers leads the way on this front. The scanner is no longer just a diagnostic device that produces images, but is a quantitative measurement system of biomarkers in the age of precision medicine.

In a different approach that accepts the premise that complicated four-dimensional B_0 errors will always exist, dynamic field cameras are devices that measure these complicated fields and either retrospectively or prospectively correct for such errors so that the result is completely corrected of the deviations that occur during the measurement process.

And of course, artificial intelligence (AI) has made great strides in recent years to become integrated in healthcare, radiology applications, and workflow. MRI is not excluded from this. AI is being assessed across a broad range of applications from improving lesion conspicuity, to increasing SNR without the typical compromise in spatial resolution, and using deep-learning algorithms to correct for B_0 -related errors and producing super-resolution results.

Concluding remarks

At the beginning of my career, it was extremely important to me that I never stop learning in whatever field I chose. If I stopped learning, I vowed that I would change my direction. I never anticipated that when I chose to be a scientist in the field of magnetic resonance imaging that I would still be here today 35 years later where never a day passes that I am still fascinated by what can be accomplished with this incredible technology.

James Clerk Maxwell may not have ever expected that magnetic fields would be exploited in this way, but I am pretty sure he would be quite pleased to see what we have done with them.



Contact

John E Kirsch, Ph.D.
 Director, Human Imaging Core
 Athinoula A Martinos Center for Biomedical Imaging
 Massachusetts General Hospital
 Department of Radiology
 149 Thirteenth Street, Room 2301
 Charlestown, MA 02129
 USA
jkirsch@mgh.harvard.edu

Extending the Reach of MRI with Remote Operations

Bac Nguyen¹; Lukas Sevcik²

¹ARISTRA, Rasta, Norway

²ARISTRA, Dübendorf, Switzerland

Introduction

In times of unexpected circumstances, one needs dedicated approaches and strategies to be able to perform as usual. Due to COVID-19, a lot of private institutes and hospitals are having to change their ways of thinking. One of the most important messages that we'd like to highlight and discuss in this article is that it is possible to provide high-quality examinations without local support.

The key to doing so is a well-connected digital network of specialists. At ARISTRA, our entire infrastructure is based on doctors and technicians in different locations. We have been operating in this way for almost two years now, and we have never had the feeling that we are missing something.

The MRI institutes, where we operate, are widely spread out. This means that, even before the coronavirus restrictions, we sometimes could not set our protocols onsite. We want to highlight some pitfalls and issues that users might run into, and show the solutions we find useful for our work processes.

Scanners at different sites may differ in many ways, even if they look alike.

Examples include:

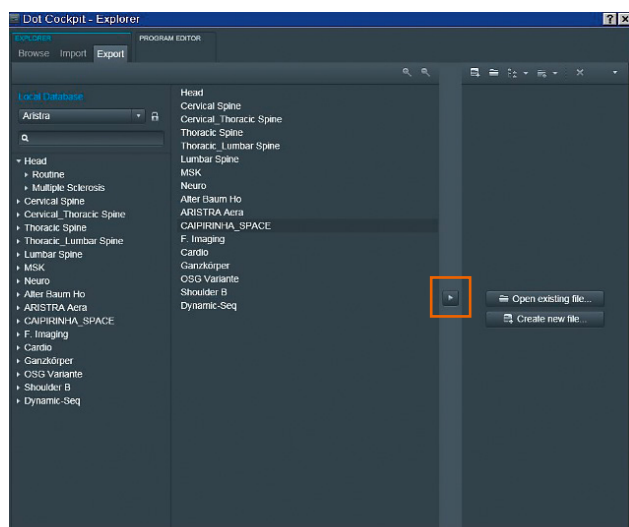
- gradient strengths
- coils
- versions/releases
- magnetic field strength
- environmental circumstances
- licenses or software packages
- vendors and their specific sequences
- patients/study participants

As you can see, there are many aspects that can bring up plenty of challenges. To make sure our protocols provide the same quality on different scanners, we must keep all of them in mind.

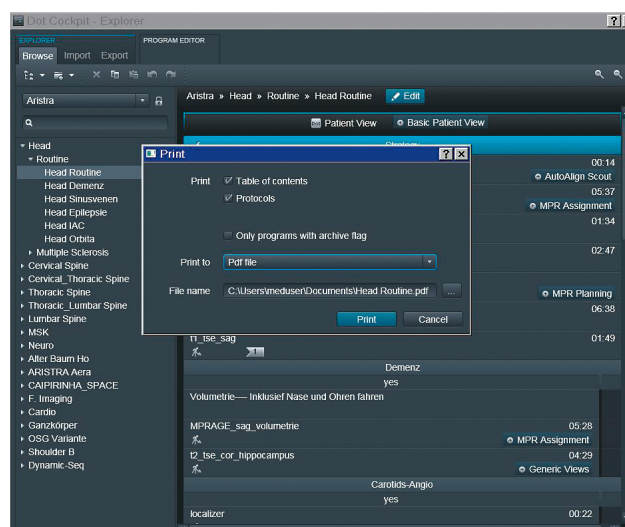
Our approaches

Exporting protocols

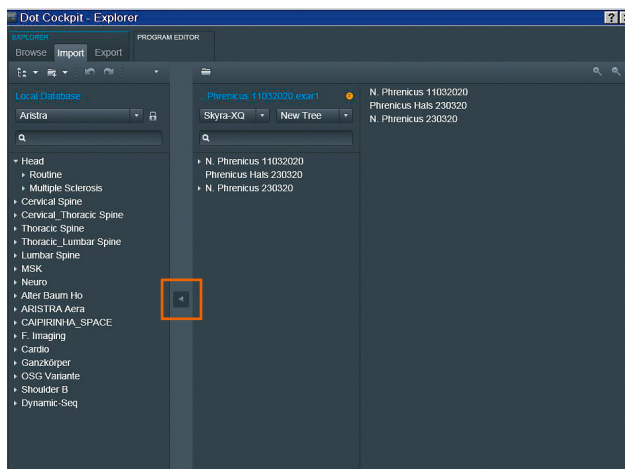
When we finish our protocols, we have to export them from the scanner unit. The Dot Cockpit provides a simple solution: just click on the arrow in the 'Export' menu (Fig. 1).



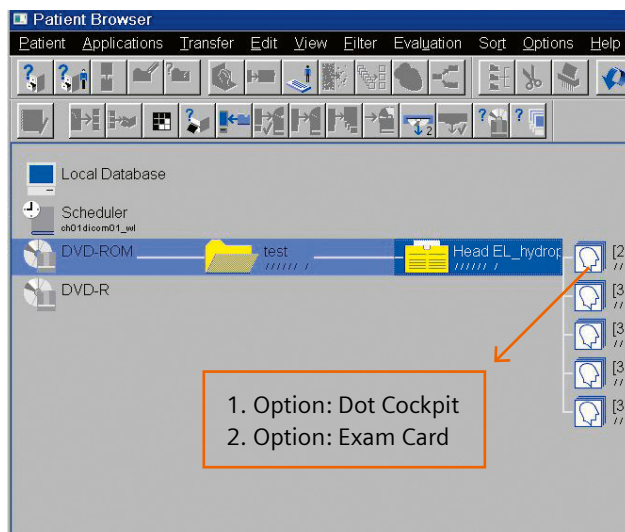
1 Prepare your protocol and use the arrow to export it to your favorite destination.



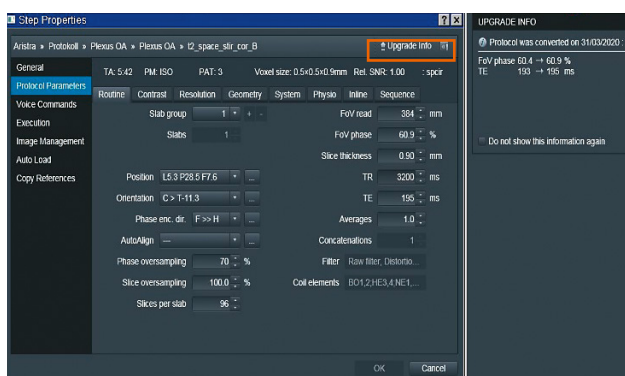
2 Choose your protocol and use the 'Print' option to export your data as a PDF or XML file.



- 3** Choose your protocol from your source and click on the arrow to tell the Dot Cockpit to import it to your workstation.



- 4** Choose your sequence and drag and drop it either to the Dot Cockpit or your exam card to scan immediately.



- 5** Choose 'Upgrade Info' to see the adaptation of relevant parameters.

It also gives you the opportunity to export the finished data as a PDF or XML file (Fig. 2). Our recommendation is to export it as all different file types to make sure that one of them will be suitable for the scanner on which you are about to implement the protocol.

Also, if you have images with your preferred protocol, syngo.via gives you the opportunity to export them to a CD or into your PACS. You'll see in the next step why this can be useful.

Importing protocols

Implementing protocols on a workstation can also be done in the Dot Cockpit. You'll find another arrow in the 'Import' menu (Fig. 3).

This can be done easily, but there can also be some difficulties with the scanner/release version. While trying to implement the .edx or .exar file, the Dot Cockpit will show you what the issue is caused by:

- Version/release incompatibility → take the information from the Dot Cockpit and set up the protocols on your scanner manually.
- Hardware incompatibility (e.g., differences in gradient system or local coils) → the system will show a popup window telling you that it is about to transform the sequences in your current system. After this process, you'll be able to see in the Dot Cockpit what parameters have changed (Fig. 5). We strongly recommend checking these parameter changes and adapting as necessary, probably with a sample patient.

If you only have images that you want to implement on your scanner, you can just drag and drop them into your Dot Cockpit or into the queue in the exam card.

Adapting protocols

Parameters can convert due to hardware differences, and these have to be adapted by technicians onsite. Check the mentioned list with changes before you start adapting. Protocols with parameter changes due to conversion are underlined, and can therefore be identified easily. Perform a sample examination to make sure the image quality is the same as before.

Remote approach

In certain situations it can be difficult to achieve the same quality as on the reference scanner. If no application specialist is available, we recommend using Expert-i. This software from Siemens Healthineers provides you with a fully remote workstation.

Another option from Siemens Healthineers is syngo Virtual Cockpit. This option allows technologists or radiologists to access the current examination from anywhere in the world. This can be very useful if the technologist needs assistance with difficult cases.

syngo Virtual Cockpit can also be a cost-effective way of teaching technologists remotely, or troubleshooting with application specialists. As Siemens Healthineers says, *syngo* Virtual Cockpit helps you move knowledge, not staff.

At ARISTRA, we do not currently have the *syngo* Virtual Cockpit available on any of our scanners, but this is something we looked into long before the pandemic hit. We hope the *syngo* Virtual Cockpit will be available on our scanners in the near future. This will enable us to maintain our protocols well, teach newer technologists, optimize processes together, and even manage difficult cases without being physically present.

Conclusion

Protocol maintenance can be a complicated process that has to be performed by highly skilled technicians. This is especially true when the hospital has different scanner types and different sites. However, there are ways to make it easier by using remote operating systems and staff. Our solutions show some of the basic approaches.

As institutes and hospitals spread their MRI scanners, there should be improvements in the entire infrastructure. We recommend considering and taking a look at the *syngo* Virtual Cockpit, which in our opinion is a holistic solution for remote maintenance and high-quality examinations.

Contact

Bac Nguyen, BSc, RT (R) (MR), App.Sc (MR)
Senior MR Radiographer
ARISTRA
MRI application Specialist
Rasta, Norway
Phone: +47 97702111
bac.nguyen@aristra.com



Lukas Sevcik
Senior MR Radiographer
ARISTRA – radiology network service
Applications Operations Manager
Dübendorf, Switzerland
Phone: +41764746332
lukas.sevcik@aristra.com

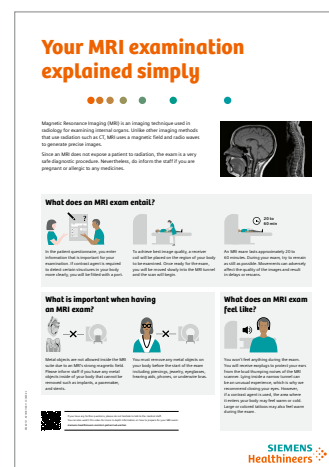
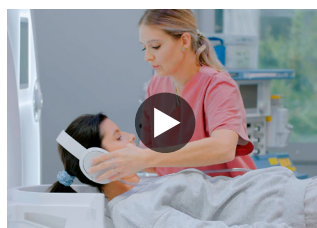
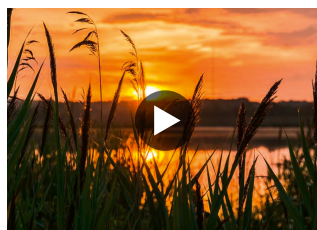
Advertisement

Prepare your patients mentally for their MRI exam

Most patients who undergo an MRI exam, experience some level of anxiety. As a result, some move so much that they cause motion artifacts, cannot complete the scan, or do not even show up for the exam. Up to 75%¹ of all unsatisfactory scan outcomes can be eliminated by educating patients on the MRI exam.

Tap the full potential of your facility by preparing your patients for the scan with our Patient Education Toolkit. A **video**, **poster**, **meditation**, and a **book for children** explain the process of an MRI exam in simple words and answer common questions:

- What does an MRI exam entail?
- What is important when having an MRI exam?
- What does an MRI exam feel like?



Download the Patient Education Toolkit in your preferred language here:
siemens-healthineers.com/mri-patient-education

¹ Törnqvist, E., Månsson, A., Larsson, E.-M., & Hallström, I. (2006). Impact of extended written information on patient anxiety and image motion artifacts during magnetic resonance imaging. *Acta Radiologica*, 47(5), 474–480. <https://doi.org/10.1080/02841850600690355>.

How Blended Learning Can Provide Answers for Training in the COVID-19 Pandemic: Experience from France

Magali Lopes¹; Maxime Roger²

¹Siemens Healthineers, Saint-Denis, France

²Siemens Healthineers, Ronchin, France

Sincere thanks to the radiologists Professor Verclytte and Professor Budzik, and to the entire team at Hôpital Saint Philibert!

Introduction

The current pandemic is creating complications for day-to-day exams, work, and organizational tasks. Healthcare providers have to respond agilely to new events every day, and they must always put safety first. As of February 2021, more than three million people in France had contracted COVID-19. (<https://www.gouvernement.fr/info-coronavirus/carte-et-donnees>)

Isolation makes it possible to contain infections and reduce the pressure on the health service. When a person tests positive for COVID-19 in France, they must give their

health insurance provider a list of everyone they met over the past few days. The insurance provider will then instruct the contacts to self-isolate for several days and take a test.

Many hospitals have had to adapt their processes because of the pandemic. Since the beginning of the pandemic, Siemens Healthineers has been working hard to find the best ways of responding to the situation. Its digital services have allowed the company to continue delivering all the support its customers need during this challenging period.



1 The team at Hôpital Saint Philibert, Lille, France

Blended learning

Mixing different training formats (blended learning) is a key feature of learning today, and it has become even more important since the COVID-19 pandemic began. Blended learning provides flexibility and allows direct customer contact without the need for physical presence and travel. It enables people to learn without the pressure of exams and patient handling – and it is a good way of adapting the learning path and format to the individual user's needs.

The customer

Hôpital Saint Philibert is a private university hospital that is part of the GHICL group in northern France. It focuses heavily on neurology, musculoskeletal (MSK), and liver examinations.

Professor Verclytte (neuro, brain perfusion) and Professor Budzik (MSK, diffusion tensor imaging) are well-known within the scientific community and have published numerous papers. The hospital's MRI system is shared with two other private institutions (HPVA, IRIS).

The site, which performs around 6,000 MRI scans per year, has various devices from Siemens Healthineers: 3 remote-controlled fluoroscopy systems, 4 mobile C-arms, 1 interventional angiography system, 1 MRI system, 2 CT scanners, and 2 picture archiving and communication systems (PACS).

The hospital has a large stroke care unit, which treats between 10 and 15 strokes per week.

The challenge

A two-week handover onsite training for a 3T MAGNETOM Vida scanner was scheduled to take place at the hospital. However, an unexpected event led to a change of plans.

The first week of onsite training went well, but at the end of the week one of the technologists tested positive for coronavirus. In line with French regulations and the

policy in place at Siemens Healthineers, the onsite training had to be stopped.

The application specialist therefore had to quickly adapt the second week of training, moving it from onsite to online. This was possible thanks to the customer agreement, good reactivity, and the necessary IT infrastructure.

Moving the program online allowed the second week of training to go ahead as scheduled. Without this solution, the technologists and radiologists would have had to postpone their training. This would have potentially impacted exam quality due to the lack of ability to optimize sequences, and would have caused problems in patient scheduling. Without full training, the team might have been unable to perform some exams, particularly since they used to work with a different vendor's system.

We were able to respond quickly to the situation and provided transparency from both a customer and patient perspective.

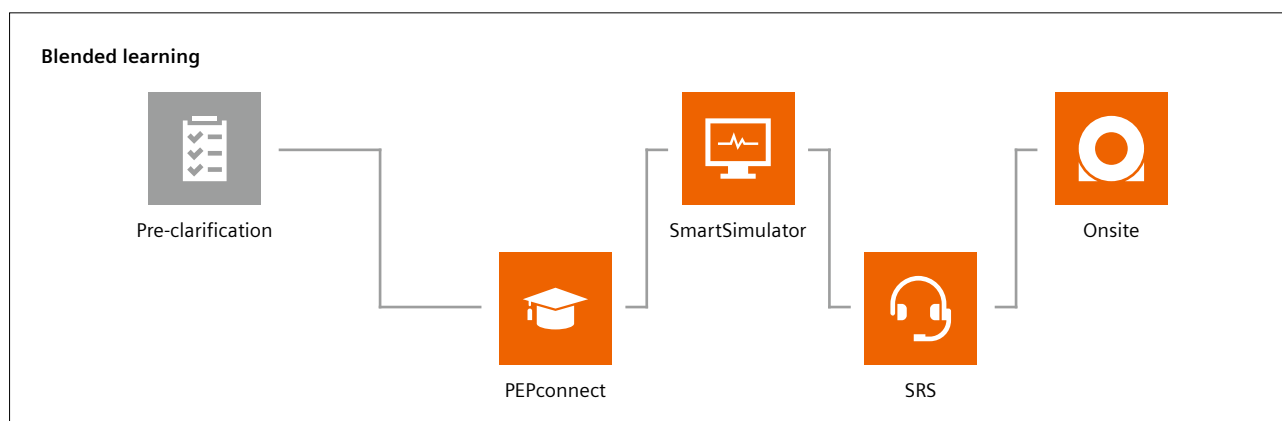
Online pre-clarification

To create the best conditions for learning and to optimize the training for the customer, the application specialist discusses the program with the customer by phone and email one to two months before the training is scheduled to take place. The conversation allows the application specialist to be sure that the training will fit the users' needs.

It is important to have information about patient throughput and exam duration at the customer site, as this will help with exam scheduling for patients and planning holiday times for clinical staff.

PEPconnect

PEPconnect is one of the training pillars. This online platform provides customers with free access to more than 8,000 learning activities, 600 of which are available in French. As a pre-training tool, PEPconnect improves



2 The four pillars of blended learning: PEPconnect, SmartSimulator, Siemens Remote Service (SRS), and Onsite support.

efficiency during the handover, allowing a strong focus on image quality and smooth exam workflows. It also enables learners to complete their training activities from anywhere, and at any time.

Through PEPconnect, Siemens Healthineers can provide a fully personalized training path for users. For Hôpital Saint Philibert, more than 20 different learning activities were provided. The content covered MRI safety, the use of different software features, memory aids, and shortcuts in a highly interactive way, including videos. Figure 3 shows the hospital's training path and the training progress of the site staff.

SmartSimulator provides a virtual classroom

SmartSimulator online sessions last for two hours and involve the application expert sharing their screen with participants to present and explain how to use the new system interface. Eleven technologists from the Saint Philibert team participated. The aim of the sessions was to allow the technologists to familiarize themselves with using the software and to answer their questions about the PEPconnect content and software features.

Once participants have subscribed to PEPconnect, participating in a virtual classroom is as simple as following an e-learning session.

Image demonstration

Image-quality requirements were defined via demonstration. During a Microsoft Teams meeting, a *syngo.via* clinical demonstration expert showed different images from cardiology, neurology, MSK, and whole-body exams on a *syngo.via* server.

The customer could choose the images they wanted to work with before the onsite training began. The application specialist then adapted the protocols in advance to meet the customer's expectations.

Onsite training

During the first week of customer training, an application specialist was onsite to deliver the agreed training. As various e-learning activities had already been provided to the technologists and radiologists, they were well prepared for using their new equipment. The work done before the installation (importing protocols for the customer) enabled easier and quicker system handling and allowed the team to concentrate on learning.

Smart Remote Services: Remote Trainer

The second week of training was scheduled to be onsite. However, due to the COVID-19 case in the team, it was decided to move the training online.

Smart Remote Services (SRS) is the infrastructure that enables Siemens Healthineers to provide customers with technical and application support for all equipment connected to the service.

This solution provides quick and secure access to an application hotline for answers to any questions (as part of the French Service contracts). It also offers access to Remote Trainers who can respond to ad hoc training needs. This is the tool that allowed the second week of training to take place online.

Participants shared the acquisition screen with the application specialist via the secure SRS link, and a Microsoft Teams meeting enabled direct contact and live communication throughout the remote training.

After the MAGNETOM Vida handover, additional training is also provided during the warranty period. This began two weeks after installation and continues for one or two years. The sessions are used to optimize the scanner and its protocols, to review cases that were not covered by all the technologists, to evaluate complicated exam cases, and to ensure that everyone assimilated the relevant knowledge.

Potential challenges for virtual remote training

The right IT infrastructure is key to the success of virtual remote training: a computer, a wireless connection, Microsoft Teams, and a good microphone and camera are all important! Although everyone is socially distanced, Siemens Healthineers works hard to make the training as personal as it would be if it were delivered onsite.

The IT department at Hôpital Saint Philibert provided the team with everything they needed. One element not to be underestimated is the importance of testing that everything is working properly before the training starts. This will help to avoid any breakdowns in communication caused by faulty microphones or cameras. The MR system was monitored using TeamViewer.

Feedback

Professor Sébastien Verclytte, a neuroradiologist and head of the radiology department, said: "The face-to-face and distance learning has been very effective. The technologists are more involved in the acquisition during the remote training, and they have more control and can work on the system while being supervised by the application specialist. There are less errors in the acquisition of sequences because the technical parameters are verified in real time by the application specialist."

3A **GHICL-St Philibert (Responsable)**

Instructions

La frise représente vos tâches pour chaque événement. Le vert indique que la tâche est terminée et l'orange qu'elle est en cours. Vous pouvez accéder à et modifier n'importe quelle tâche terminée ou en cours. Envoyer des certificats n'est possible que le jour de début de l'événement.
Pour ajouter un événement, cliquez sur «Nouveau groupe d'événement de formation».

+ Nouveau groupe d'événement de formation

Formations initiales pour la VIDA

Date d'échéance: 09/02/2020
Plan Pas commencé: 7 En cours: 7 Terminé: 4

Détails événement Définir assignation Inviter membres Consulter les assignations

Progression de l'export des assignations Exporter les participants

Membres (20)

Nom	Rôle	Statut
...	responsable	Actif
...	Invitation en attente	Formations initiales pour la VIDA
...	Actif	Formations initiales pour la VIDA
...	Invitation en attente	Formations initiales pour la VIDA
...	Actif	Formations initiales pour la VIDA
...	Actif	Formations initiales pour la VIDA
...	Invitation en attente	Formations initiales pour la VIDA
...	Actif	Formations initiales pour la VIDA
...	Invitation en attente	Formations initiales pour la VIDA
...	Actif	Formations initiales pour la VIDA
...	Invitation en attente	Formations initiales pour la VIDA
...	Actif	Formations initiales pour la VIDA
...	Invitation en attente	Formations initiales pour la VIDA
...	Actif	Formations initiales pour la VIDA
...	Invitation en attente	Formations initiales pour la VIDA
...	Actif	Formations initiales pour la VIDA
...	Invitation en attente	Formations initiales pour la VIDA
...	Actif	Formations initiales pour la VIDA

The remote link to the application specialist also avoids too many people being in the same room at the same time. The technologists had access to the screen simultaneously with the application specialist, which was very convenient for them.”

Conclusion

Within the current pandemic, blended learning can reduce risk, enable social distancing, and make it easier to respond to customers' needs. These were exactly the benefits of blended learning at Hôpital Saint Philibert. Siemens Healthineers has many solutions that can make organizing and running the training completely transparent and smooth for the customer – even when COVID-19 forced us to change the planned training method from one day to the next.

Contact

Magali Lopes
Siemens Healthcare SAS
SHS EMEA FBA FRA CS BS
40 avenue des Fruitiers
93527 Saint-Denis Cedex
France
Phone: +33 617109514
magali.lopes@siemens-healthineers.com



Maxime Roger
Siemens Healthcare SAS
SHS EMEA FBA FRA CS APP DI&AT1
Postbox 3
59790 Ronchin Cedex
France
Phone: +33 625362257
maxime.roger@siemens-healthineers.com



3B

Aide-mémoire PEConnect · Trouver la formation adaptée à la version de mon logiciel

- Sécurité IRM - Introduction
- Sécurité IRM - Chapitre 1 Préface sur la sécurité IRM
- Sécurité IRM - Chapitre 2 Examen préalable du personnel IRM et des patients
- Sécurité IRM - Chapitre 3 Examen du patient
- Sécurité IRM - Chapitre 4 En cas d'urgence
- Configuration à un moniteur (XA20)
- Messages système et historique des messages (XA20)
- Écran d'accueil et écran de démarrage (XA20)
- Configuration à deux moniteurs (XA20)
- Enregistrement du patient (XA20)
- syngo MR XA11 - Raccourcis MR View&GO Aide-mémoire
- BioMatrix Spine 32
- BioMatrix Body 12
- BioMatrix Head/Neck 20

3 Training path and the training progress.

Meet Siemens Healthineers

Siemens Healthineers: Our brand name embodies the pioneering spirit and engineering expertise that is unique in the healthcare industry. The people working for Siemens Healthineers are totally committed to the company they work for, and are passionate about their technology. In this section we introduce you to colleagues from all over the world – people who put their hearts into what they do.

Haitham Mohamed, Ph.D.

I'm Haitham Mohamed and I work as a business development manager in the MR strategy department in Erlangen, Germany. After joining Siemens Healthineers in 2007, I worked in various roles as a CT and MR product specialist, and later as a product manager. In 2014, I became the MR Business Line manager in Egypt. While continuing in this role, I also became an MR collaboration manager in 2015, and then scientific partnership head for the Middle East and South East Africa. While working at Siemens Healthineers, I also earned my Master's (2004) and Ph.D. (2010) in magnetic resonance imaging from the Faculty of Engineering at Cairo University in Egypt.



Erlangen, Germany



How did you first come into contact with MRI?

It was almost 20 years ago, during my bachelor studies in Cairo. My supervisor gave us an interesting lecture about MR physics and the potential benefits over other imaging modalities. The fascinating mixture of physics and mathematics sparked my interest the field, and just three days later we were working out how to simulate and reconstruct our first experimental MR images. That was awesome.

What are the greatest challenges in your job?

The pace of development in healthcare is so fast right now. You have to lift your head above your day-to-day work and consider the larger environment in which you're operating. It's about asking questions and challenging assumptions about the way things work in your environment and in the industry as a whole. One major challenge is how to leverage the current developments in technology to increase accessibility, improve care delivery, and achieve better outcomes for patients. It is important that we find ways to overcome the lack of trained staff and offer routes to training and development for healthcare workers in general and for radiologists, technologists, and biomedical engineers in particular. The patient experience should also be a key consideration when envisaging future developments.

The Aswan Heart Centre in Egypt is a specialist institution that treats children from all over Africa. We collaborate with AHC on heart diseases. Integrating and incorporating research work into daily routine is a key success factor for the center. Research is not a luxury part of the job, but

rather a necessity to accomplish the center's mission. Providing the required applications was therefore just one pillar for us. The other was about transferring our expertise to AHC, and vice versa so that we have a thorough understanding of the local clinical challenges. This continuous feedback loop is the cornerstone of our successful collaboration.

In a nutshell, the biggest challenge of my job is about finding ways to enable access to innovations that can meet basic needs in a highly efficient and affordable way.

What about MRI fascinates you and keeps you moving?

I would say the main motivation is a commitment to supporting and helping people and communities, improving their quality of life, and giving them hope for a better future. One of the greatest examples of this is our collaboration on heart diseases with Aswan Heart Centre. Its vision for providing neglected communities with the highest level of care is the same as any other center of excellence anywhere in the world: It works with commitment and dedication, serving patients free of charge regardless of who they are and where they come from. I'm proud that, as a leading healthcare company, we are involved with this kind of institute and its communities – that we are an integral part and enabler of its mission. I'm not on the front line with patients, but I still feel happy about every patient's smile on their journey to recovery. Ultimately, I'm driven by the impact that MRI has on people's lives.

What do you think are the most important developments in healthcare?

Increased accessibility to medical imaging such as MRI is an important factor for bringing the benefits to a wider population. Diagnostic information gained by MRI will definitely improve a patient's treatment journey, especially if it is deployed at an early stage. But MRI is still a highly specialized and expensive modality that is not widely used. Developments in the affordability of MR itself, shorter scan times, and automated patient-specific technologies powered by AI and machine learning will all help to make MRI available to more patients. In addition, there is growing interest in having a second opinion immediately before and during the scan either from the technologist or the

radiologist. So facilitating this kind of communication in a way that preserves patient privacy and assures confidence in the outcome will be a game-changer, especially in rural areas.

What would you do if you could spend a month doing whatever you wanted?

Outside of work, I enjoy spending time with my family, reading, walking, telling my children stories, and playing chess. I love to travel and discover new places, meet new people, and learn about new cultures. Getting away from my normal day-to-day routine gives me the opportunity for personal reflection and allows me to refresh my mind and to practice meditation.

Get to know us

Find more portraits of Siemens Healthineers around the world

www.magnetomworld.siemens-healthineers.com/meet-siemens-healthineers



The entire editorial staff at All India Institute of Medical Sciences, New Delhi, India and at Siemens Healthineers extends their appreciation to all the radiologists, technologists, physicists, experts, and scholars who donate their time and energy – without payment – in order to share their expertise with the readers of MAGNETOM Flash

MAGNETOM Flash – Imprint

© 2021 by Siemens Healthcare GmbH,
All Rights Reserved

Publisher:

Siemens Healthcare GmbH
Magnetic Resonance,
Karl-Schall-Str. 6, D-91052 Erlangen, Germany

Editor-in-chief:

Antje Hellwich
(antje.hellwich@siemens-healthineers.com)

Guest Editors:

Professor Dr. Raju Sharma, M.D., MAMS, FICR ;
Dr. Devasenathipathy Kandasamy, M.D.;
Dr. Ankur Goyal, M.D.
Department of Radiology
All India Institute of Medical Sciences, New Delhi, India

Editorial Board:

Rebecca Ramb, Ph.D.; Sunil Kumar S. L., M.D.;
Wellesley Were; Jane Kilkenny; Nadine Leclair, M.D.

Review Board:

André Fischer, Ph.D.; Daniel Fischer;
Christian Geppert, Ph.D.; Heiko Meyer, Ph.D.;
Gregor Thörmer, Ph.D.

Copy Editing:

Sheila Regan, Jen Metcalf, UNIWORKS,
www.uni-works.org
(with special thanks to Kylie Martin)

Layout:

Agentur Baumgärtner,
Friedrichstr. 4, D-90762 Fürth, Germany

Production:

Norbert Moser,
Siemens Healthcare GmbH

Printer:

G. Peschke Druckerei GmbH,
Taxenstr. 4, D-85599 Parsdorf b. Munich, Germany

Note in accordance with § 33 Para.1 of the German Federal Data Protection Law: Despatch is made using an address file which is maintained with the aid of an automated data processing system.

MAGNETOM Flash is sent free of charge to Siemens Healthineers MR customers, qualified physicians, technologists, physicists and radiology departments throughout the world. It includes reports in the English language on magnetic resonance: diagnostic and therapeutic methods and their application as well as results and experience gained with corresponding systems and solutions. It introduces from case to case new principles and procedures and discusses their clinical potential. The statements and views of the authors in the individual contributions do not necessarily reflect the opinion of the publisher.

The information presented in these articles and case reports is for illustration only and is not intended to be relied upon by the reader for instruction as to the practice of medicine. Any health care practitioner reading this information is reminded that they must use their own learning, training and expertise in dealing with their individual patients. This material does not substitute for that duty and is not intended by Siemens Healthcare to be used for any purpose in that regard. The drugs and doses mentioned herein are consistent with the approval labeling for uses and/or indications of the drug. The treating physician bears the sole responsibility for the diagnosis and treatment of patients, including drugs and doses prescribed in connection with such use. The Operating Instructions must always be strictly followed when operating the MR system. The sources for the technical data are the corresponding data sheets. Results may vary.

Partial reproduction in printed form of individual contributions is permitted, provided the customary bibliographical data such as author's name and title of the contribution as well as year, issue number and pages of MAGNETOM Flash are named, but the editors request that two copies be sent to them. The written consent of the authors and publisher is required for the complete reprinting of an article.

We welcome your questions and comments about the editorial content of MAGNETOM Flash. Please contact us at
magnetomworld.team@siemens-healthineers.com

Manuscripts as well as suggestions, proposals and information are always welcome; they are carefully examined and submitted to the editorial board for attention. MAGNETOM Flash is not responsible for loss, damage, or any other injury to unsolicited manuscripts or other materials. We reserve the right to edit for clarity, accuracy, and space. Include your name, address, and phone number and send to the editors, address above.

MAGNETOM Flash is also available online:

www.siemens-healthineers.com/magnetom-world

Not for distribution in the US

On account of certain regional limitations of sales rights and service availability, we cannot guarantee that all products included in this brochure are available through the Siemens sales organization worldwide. Availability and packaging may vary by country and is subject to change without prior notice. Some/All of the features and products described herein may not be available in the United States.

The information in this document contains general technical descriptions of specifications and options as well as standard and optional features which do not always have to be present in individual cases, and which may not be commercially available in all countries.

Due to regulatory reasons their future availability cannot be guaranteed. Please contact your local Siemens organization for further details.

Siemens reserves the right to modify the design, packaging, specifications, and options described herein without prior notice. Please contact your local Siemens sales representative for the most current information.

Note: Any technical data contained in this document may vary within defined tolerances. Original images always lose a certain amount of detail when reproduced.

Siemens Healthineers Headquarters

Siemens Healthcare GmbH
Henkestr. 127
91052 Erlangen, Germany
Phone: +49 9131 84-0
siemens-healthineers.com